UC Berkeley
UC Berkeley Electronic Theses and Dissertations

Title

Interactions of Point Defects and Other Localized States with Charge and Structural Disorder in Complex Materials

Permalink

https://escholarship.org/uc/item/3qs1q5qw

Author

Srivastava, Shivani

Publication Date

2024

Peer reviewed|Thesis/dissertation

eScholarship.org Powered by the California Digital Library
University of California

Interactions of Point Defects and Other Localized States with Charge and Structural Disorder in Complex Materials

By

Shivani Srivastava

A dissertation submitted in partial satisfaction of the

requirements for the degree of

Doctor of Philosophy

in

Engineering - Materials Science and Engineering

in the

Graduate Division

of the

University of California, Berkeley

Committee in charge:

Professor Mark Asta, Chair
Professor Darryl Chrzan
Professor Jeffrey Neaton

Spring 2024

Interactions of Point Defects and Other Localized States with Charge and Structural Disorder in Complex Materials

Copyright 2024
by
Shivani Srivastava

Abstract

Interactions of Point Defects and Other Localized States with Charge and Structural Disorder in Complex Materials

by

Shivani Srivastava

Doctor of Philosophy in Engineering- Materials Science and Engineering

University of California, Berkeley

Professor Mark Asta, Chair

Materials with strong coupling between structural and electronic degrees of freedom (charge, orbital and spin) are of interest for a wide array of functional applications. Localized electronic states resulting from point defects and bound-excitons in ionic materials influence functional behavior of these materials. We explore the consequences of such couplings on defect properties and excited states, for cases where intrinsic charge and structural disorder give rise to a variety of local environments. Using Density Functional Theory (DFT) with Hubbard U correction and hybrid density functional theory levels of theory, we study how local distortions and chemical disorder influence the localized electronic states determining bulk properties such as defect thermodynamics and scintillation. The work presented in this thesis focuses on two illustrative cases.

We investigate the energetics underlying charge ordering, defect formation and clustering in iron oxides. For magnetite (Fe_3O_4), we study the energetics underlying the ordering of Fe^{2+} and Fe^{3+} cations, and the effect of this ordering on point defect energetics and electronic structure. The calculations reveal strong variations in anion and cation vacancy formation energetics and stable charge states with changes in local environment. We also extend this study to oxygen-iron vacancy complexes in magnetite (Fe_3O_4) and hematite (Fe_2O_3) and find a significant thermodynamic driving force for oxygen and iron vacancies to bind. The results have potentially important implications for ionic transport, as the low energy defect configurations in certain local chemical environments can lead to percolating networks of low-energy migration pathways. In the second topic, we consider the nature of localized exciton states in Tl_2LiYCl_6, a promising candidate for commercial scintillator applications such as γ-ray detection. The driving forces for structural distortions away from the idealized cubic elpasolite crystal structure are discussed as originating from maximizing the energy lowering interactions of Tl and Cl orbitals. These distortions influence the bulk electronic

structure and lead to different stable and metastable exciton configurations. Comparison of electron-hole binding energies of exciton configurations show that the Tl^+ centered exciton exhibits the best agreement with the broad peak, as observed in the measured emission spectra.

Collectively, this work explores complexities of simulating localized defect and exciton electronic states in materials with variations in the coupled local structural and chemical environments. This research motivates further studies into developing approaches for sampling defect and exciton configurations generated by coupling of localized electronic states with structural and chemical order in the bulk.

To my mother *Sarika*

Contents

Contents **ii**

List of Figures **iv**

List of Tables **ix**

1 Overview **1**

2 Background **3**
2.1 Fe_3O_4 (Magnetite): Charge ordering in bulk and point defects 4
2.2 Tl_2LiYCl_6: A Tl based elpasolite scintillator 9

3 Computational Methods **15**
3.1 Electronic Structure Methods 15
3.2 Computational Methods for magnetite (Fe_3O_4) 18
3.3 Computational Methods for hematite 22
3.4 Computational Methods for Tl_2LiYCl_6 22

4 Modelling Magnetite using DFT: Role of charge ordering **26**
4.1 Results on Charge Ordering in Bulk Magnetite 26

5 DFT Study of Local Environment Effects on Oxygen Vacancy Properties in Magnetite **29**
5.1 Oxygen Vacancy Charge and Spin Environments 29
5.2 Neutral Oxygen Vacancies 31
5.3 Positively Charged Oxygen Vacancies 34
5.4 Discussion 37
5.5 Conclusions 40

6 Defect Complexes in Iron Oxides **41**
6.1 Iron vacancies for octahedral sites in magnetite 41
6.2 Brief Discussion on iron vacancies in magnetite 46
6.3 Iron-Oxygen di-vacancy in magnetite 47

6.4 Iron Oxygen di-vacancy in Fe_2O_3 (Hematite) 56

7 Density Functional Theory study of structure and optical properties of the elpasolite scintillator Tl_2LiYCl_6 60

7.1 Structural Analysis of bulk Tl_2LiYCl_6 61

7.2 Electronic and Optical properties of cubic and other low energy phases of Tl_2LiYCl_6 71

8 Conclusions and Future Work 78

8.1 Extension of the iron oxide work 79

8.2 Extension of the Tl_2LiYCl_6 work 82

Bibliography 84

List of Figures

2.1 Schematic illustration of the cubic inverse spinel structure for magnetite, showing the calculated relaxed positions and coordination of representative ions. Panel (a) shows only oxygen anions (red circles), which form a face-centered cubic sublattice. The iron cations are distributed on two different sublattices, each consisting of (b) tetrahedrally coordinated sites occupied by Fe^{3+} (as indicated by the dark green shading of the tetrahedra) and (c) octahedrally coordinated sites occupied by both Fe^{3+} and Fe^{2+} cations (as indicated by the lighter green shading of the octahedra). The edges of the cubes correspond to the lattice vector directions for the conventional unit cell for the cubic inverse spinel structure. . . 5

2.2 Schematic illustration of the low-temperature monoclinic phase of magnetite with its 224 atom conventional unit cell. Panel (a) illustrates the ordering of Fe^{2+} (yellow octahedra) and Fe^{3+} (green octahedra) cations on the octahedral sublattice, while (b) shows the tetrahedral sublattice occupied exclusively by Fe^{3+} cations (green tetrahedra). Oxygen positions are indicated by red circles. 6

2.3 Schematic of a Tl^{+} ion acting as an activator ion. When present as a dopant substituting a group 1 monoatomic ion such as Na^{+}, the occupied $6s^2$ orbitals and unoccupied 6p orbitals exist as localized states within the bulk band-gap. The Tl^{+} ion can act as a site for exciton capture by trapping a hole in the $6s^2$ orbitals and subsequent capture of an electron in the 6p states. (a) and (b) describe the state of the system before and after the capture of electron and holes, leading to a bound exciton state. 10

2.4 The 40 atom conventional unit cell for the cubic $Fm\overline{3}m$ phase of the elpasolite phase of Tl_2LiYCl_6. The gold and silver spheres represent Cl^{-} anions. The silver spheres represent Tl^{+} ion in the A sites of the structure. The Li and Y ions are located in the B-site centered octahedra, indicated respectively with dark and light green shading. 13

3.1 Dependence of total energy on number of electrons(N, defined relative to the neutral value) for the 224 atom monoclinic magnetite cell. The x-axis denotes the fractional number of electrons in the supercell, and the y-axis is the total energy from DFT+U calculation for $U_{eff} = 4.1$ eV 16

3.2 448 atom supercells for cubic magnetite, representing different models for charge ordering on the octahedral sublattice. These models are created as a 2 × 2 × 2 supercell of the conventional inverse spinel cubic unit cell, which consists of 56 atoms, making the total number of atoms equal to 448. This is in contrast to the monoclinic structure, which, in the conventional unit cell, contains 224 atoms. In each panel, only the oxygen positions (red circles) and octahedra (dark green, yellow and light green) are highlighted. All tetrahedral sublattice sites are occupied by Fe^{3+} (not shown). In panel (a) Fe^{3+} (dark green) and Fe^{2+} octahedral sites are ordered according to the configuration found in the low-temperature monoclinic structure (note that the cubic unit cells here are rotated relative to that for the monoclinic structure illustrated in Fig. 2.2). In panel (b) the Fe^{3+} and Fe^{2+} sites are arranged according to a special-quasirandom structure model for random configurational disorder on the octahedral sublattice. In panel (c) the light green octahedra denote an averaged Fe octahedral site with effective charge of 2.5 19

4.1 Electronic density of states for the three different charge ordering models on the octahedral sublattice for 448 atom supercells of cubic magnetite. The labels (a), (b) and (c) correspond to charge-ordering models described in 3.2. In this plot, the value of the Fermi energy (E_{Fermi}) corresponds to the highest occupied state. DOS for spin-up (spin-down) electrons are plotted as positive (negative) values. 28

5.1 Fe coordination around O vacancy in bulk monoclinic. The red circles denote the oxygen site, the green and yellow circles denote Fe^{3+} and Fe^{2+} respectively. All the schematics (a)-(d) have the same arrangement for octahedral and tetrahedral sites as shown in (a) but differ in number of Fe^{3+}/Fe^{2+} ions occupying the octahedral sites. 30

5.2 Charge redistribution around a neutral oxygen vacancy for different spin states of the excess electrons for 333 (first row), 332 (second row), 322 (third row) and 222 (fourth row) charge environments. Images in the left, middle and right column correspond to Up-Down, Down-Down and Up-Up spin configurations, respectively. In each figure, the location of the extra electrons is shown schematically as an orange circle or an ellipse connected by dashed lines to the position of the removed oxygen ion (red circle). For cases where the electron is localized on an Fe^{3+} ion (green spheres) the orange electron cloud is centered on that ion. For the case where the electron is distributed between sites, the orange ellipse is centered off an ion site. Fe^{2+} ions are shown as yellow spheres. The arrows indicate the spin state (up or down) of the electrons. The small red spheres indicate oxygen sites outside the vacancy core centered on the central, larger red sphere. 32

5.3 Total and partial electron density of states (DOS) for (a) bulk monoclinic Fe_3O_4, and neutral oxygen-vacancy supercells with (b) 222:UD:V_O and (c) 222:UU:$V_O^{\bullet}$-Fe'_{Fe} defect configurations. The mid-gap electronic state in the 222:UD:V_O oxygen vacancy is absent for the 222:UU:$V_O^{\bullet}$-Fe'_{Fe} configuration. In this plot, the value of the Fermi energy (E_{Fermi}) corresponds to the highest occupied state. DOS for spin-up (spin-down) electrons are plotted as positive (negative) values. 34
5.4 Charge redistribution around a +1 charged oxygen vacancy for (a) the 322 environment containing more than one Fe^{3+} in the vacancy core, and (b) the 222 environment containing one Fe^{3+} in the vacancy core. For both cases, the configuration of the corresponding neutral vacancy is shown on the left and that of the positively charged vacancy on the right. As in Fig. 5.2, the location of the extra electron is shown schematically as an orange circle or ellipse. The green circle on the top right figure is the localized hole on the octahedral Fe^{2+} site outside the vacancy core. 36
5.5 Formation energies for oxygen vacancies in the low-T monoclinic phase of magnetite. Results are presented for three charge states, across all the distinct local environments. The legend gives the charge and spin configurations, following the notation described in the text. Results are plotted for the range of Fermi energy spanning the band gap calculated for the bulk monoclinic structure of magnetite. 38
5.6 Formation energies for oxygen vacancies in the four different local environments, as labeled in the legends. 39

6.1 Local environments around Fe^{2+} sites on the octahedral sublattice of the monoclinic phase of magnetite. The red, blue and yellow circles denote Fe^{2+}, Fe^{3+} and the octahedrally-coordinated Fe^{2+} vacancy sites, respectively. 43
6.2 Local environments around Fe^{3+} sites on the octahedral sublattice of the monoclinic phase of magnetite. The red, blue and yellow circles denote Fe^{2+}, Fe^{3+} and the octahedrally-coordinated Fe^{3+} vacancy sites, respectively. 43
6.3 Formation energy of iron vacancies in magnetite for sixteen different Wyckoff sites and three charge states: 0, -1, -2 and -3. The red lines depict the vacancies at Fe^{2+} sites and the blue lines represent the vacancies at the Fe^{3+} sites. The -3 charge state is only depicted for 3_52_1 environment, as for the rest is is not stable with respect to decomposition to -2 charged vacancies and an unbound electron polaron. 45
6.4 Different configurations for iron oxygen di-vacancies in magnetite. The top row shows the four environments of an oxygen site, following the representation introduced in Figure 5.1. For the 332 environment, four distinct Fe-O di-vacancy configurations are illustrated by the black spheres, along with numbers (1-4) corresponding to each. 49

6.5 Formation energies for different charge states of iron-oxygen di-vacancies formed at the four different oxygen sites in magnetite. The legends in each plot denote the index of iron vacancies around the oxygen vacancy in the 448 atom monoclinic supercell. The indices between 0-63 denote tetrahedral Fe^{3+} sites. The indices 64-127 and 128-192 denote octahedral iron sites occupied with Fe^{2+} and Fe^{3+} ions, respectively. 50
6.6 Formation energies of iron-oxygen di-vacancies formed at the four different oxygen sites in magnetite for charge states +1, 0, -1 and -2. The colors for the lines correspond to different environments for the oxygen and iron vacancies as described in the text and legend. The -3 charged di-vacancies are not stable except for a single configuration as described in the text. 52
6.7 Core charges and Formation Energy for different defect charge states for each of the di-vacancy local environments, classified based on the oxygen site involved in the di-vacancy. The points denoted by "o" and "*" denote the divacancies with iron vacancy on octahedral and tetrahedral sublattices, respectively. The formation energy for charged defects is calculated for the Fermi energy at the valence band maximum (VBM). The colors of the symbols correspond to the defect charge stage, as given in the legend. 53
6.8 The formation energies of iron-oxygen divacancies, iron vacancies and oxygen vacancies in Fe_2O_3(hematite). The solid lines, dashed lines and the dotted lines denote the formation energies of the di-vacancy, iron vacancy and the oxygen vacancy, respectively. 57

7.1 Different structures of Tl_2LiYCl_6 used in this paper to analyze the role of distortions on total energy and bulk electronic structure. The dark green and light green octahedra in these figures correspond to Y-Cl and Li-Cl respectively. The grey spheres correspond to Tl ions. For all the figures, the directions of the lattice vectors are along [100], [010] and [001] directions with these axes aligned with the reference cubic elpasolite phase shown in panel (a). 62
7.2 Comparison of calculated phonon dispersion curves for cubic elpasolite structures of Cs_2LiYCl_6, Rb_2LiYCl_6 and Tl_2LiYCl_6. The number of unstable modes increase progressively from Cs_2LiYCl_6, to Rb_2LiYCl_6 to Tl_2LiYCl_6 owing to different interaction of Cs^+, Rb^+ and Tl^+ with Cl^- ions 64
7.3 Cubic Tl_2LiYCl_6 phonon density of states. Colors are element-wise projections illustrating the contribution from Tl, Cl, Li and Y, and the vertical black line denotes zero frequency. The negative frequencies values correspond to the unstable modes in phonon dispersion curve for cubic Tl_2LiYCl_6. 65
7.4 Calculated phonon dispersion curves of (a)$P4_2/n$ and (b)$P4_2$ spacegroups of Tl_2LiYCl_6. The $P4_2$ space group was reported based on refinements in neutron diffraction experiments on room-temperature Tl_2LiYCl_6. The $P4_2/n$ structure is derived from the octahedral rotations as described in the text. Both structures exhibit unstable phonon modes, originating from displacement of both Tl and Cl 67

7.5 Comparison of Tl-Cl bond distances for different structures of Tl_2LiYCl_6: $Fm\bar{3}m$ cubic elpasolite phase, the $P4_2/n$ and $P4_2$ tetragonal phases, $P\bar{1}$ and P1 triclinic phases and the polymorphous models of cubic structure. For each structure, the bond length to each of the 12 Cl neighbors of the distinct Tl atoms are plotted and values are connected by lines. The bond lengths are ordered by increasing value, such that the Cl neighbor index 1 (12) corresponds to the shortest (largest) bond length. 69
7.6 Many-body tensor representation of different structures for Tl_2LiYCl_6. The different colors correspond to the different structures of Tl_2LiYCl_6: $Fm\bar{3}m$ cubic elpasolite phase, the $P4_2/n$ and $P4_2$ tetragonal phases, $P\bar{1}$ and P1 triclinic phases and the polymorphous models of cubic structure. The x-axis and y-axis denote the Tl-Cl distances and the MBTR vector calculated using equation 7.2 as described in the text to describe each of the structure in terms of Tl-Cl bond distances. 70
7.7 A heatmap describing similarity between different phases and polymorphous representation of Tl_2LiYCl_6. From left to right and top to bottom, the phases are $Fm\bar{3}m$, $P4_2/n$, $P4_2$, $P\bar{1}$, P1 and two different polymorphic representations of cubic cell. 71
7.8 Crystal Orbital Hamiltonian Population plots for Tl_2LiYCl_6 73
7.9 Density of states with Tl contribution for different structures of Tl_2LiYCl_6 . . . 74
7.10 Different exciton configurations found in triclinic P1 Tl_2LiYCl_6 structure. Subfigure (a) shows the Tl-centered electron and hole wavefunctions for most stable exciton configuration. (b) and (c) correspond to bound exciton with a V_k like hole state and electron localized on Y^{3+} and Li^+ respectively. All the Tl sites in the triclinic structure have identical nearest neighbor local environment. 75

List of Tables

4.1 DFT-calculated energies for the three supercell models of the cubic phase of magnetite. The first column lists the supercell model as illustrated in Fig. 3.2, the second describes the configuration of the Fe^{2+} and Fe^{3+} cations over the octahedral sublattice, and the third lists the calculated energy difference, per formula-unit (fu), relative to the ground state low-temperature monoclinic phase. 27

5.1 Formation energies of neutral oxygen vacancies. The first three columns specify the environment, spin and charge configurations, and the fourth lists the corresponding calculated defect formation energy. 31

5.2 Formation energies of positively-charged oxygen vacancies. The first column specifies the environment, the second the defect charge, and the third and fourth the spin and charge configurations, respectively. The fourth column lists the calculated binding energy of the localized holes to the vacancy core (with "N/A" implying the defect configuration does not involve a localized hole). The corresponding calculated defect formation energy is given in the final column. 35

6.1 Formation energies of iron vacancies with neutral, -1,-2 and -3 charge states calculated for Fermi level at the valence band maxima. The first three columns specify the environment, spin and charge configurations, and the fourth lists the corresponding calculated defect formation energy. The first three rows are the environments around octahedral Fe^{2+} sites, whereas the last three rows denote the local environments around Fe^{3+} sites on octahedral sublattice. 44

6.2 Charge redistribution around Fe^{2+} vacancy sites. The first column lists the environment by denoting the number of 3+ and 2+ Fe neighbors (see main text). The second column gives the charge state of the defect, and the third the charge within the core after relaxing the defect configuration. For cases where the core charge differs from the overall defect charge, the binding energy of the excess electron or hole localized outside the core is given in the fourth column. In only one such case (the neutral vacancy for the $3_5 2_1$ configuration) is the excess localized charge outside the core bound. 47

6.3 Charge redistribution around Fe^{3+} vacancy sites. The first column lists the environment by denoting the number of 3+ and 2+ Fe neighbors (see main text). The second column gives the charge state of the defect, and the third the charge within the core after relaxing the defect configuration. For cases where the core charge differs from the overall defect charge, the binding energy of the excess electron or hole localized outside the core is given in the fourth column. Note that the excess electrons outside the core for the -3 charge states of the vacancy are not bound to the core. 48
6.4 Formation energies of neutral and +1 charged iron-oxygen divacancies. The first two columns specify the oxygen environment and charge configurations of the Fe cation site, respectively. The third and fourth columns lists the corresponding calculated defect formation energy for the neutral and +1 charged di-vacancy configurations, with the value of the Fermi energy corresponding to the valence band edge. 51
6.5 Binding energies of +1 charged iron-oxygen divacancies for the Fermi level at the valence band maxima. The first two columns specify the oxygen environment and charge state of the Fe site before the vacancy is introduced. The third column lists the corresponding calculated di-vacancy binding energy as described in the text. 55
6.6 Binding energies of iron-oxygen divacancies for Fermi levels above the mid-gap. The first two columns specify the di-vacancy charge state and the respective defect reaction, where $V_{Fe}^{'''}$ and V_O^X are the most stable configurations for the iron and oxygen vacancies used to calculate the binding energy. The third column shows the binding energy for the reaction in column two. 58

7.1 Energy per formula unit relative to cubic elpasolite phase for different phases of Tl_2LiYCl_6. The first column gives the structure symmetry, the second the energy relative to the reference cubic phase, and the third and fourth provide the lattice parameters and cell angles for the primitive unit cells. 68
7.2 Formation energies and emission energies of different configurations of excitons in triclinic P1 Tl_2LiYCl_6. All the formation energies are relative to the lowest energy exciton configurations found. 73
7.3 Formation energies and emission energies of different configurations of excitons localized on three distinct Tl sites in tetragonal Tl_2LiYCl_6 with $P4_2/n$ symmetry. All the formation energies are relative to the lowest energy exciton configurations found. 77

Acknowledgments

First and foremost, I would like to thank my advisor Prof. Mark Asta for his support and guidance all through my PhD. I have been fortunate to experience your uncommon blend of intellect and kindness, as you helped me navigate the ups and downs of the past few years. It would not have been possible for me to chase after the complexities of my research problems without your continuous encouragement during my moments of doubt. In addition to learning how to do scientific research, I have benefitted tremendously from observing your excellent work ethic, humbleness and genuine commitment to your students, and will hopefully be able to emulate and carry it forward in my life.

I would also like to thank my collaborators Blas Uberuaga, Andrew Canning and Mauro Del Ben for thoughtful discussions and providing me opportunities to work on interesting problems. Throughout past years, I have also learned a lot from members of Asta Research group: Danny, Anas, Shahriar, Nick, Enze, Flynn, Nathan, Andrea, Pedro, Kuner, Yuan and many others. It was always nice to catch a little break through office chit-chat, and our interactions have often lifted me out of low spirits during tedious work days. Special thanks to Guy Moore for being a great friend through the challenges of work and life, helping me keep things in perspective.

None of this would have been possible without the love and support of my family. To the memory of my grandparents Shrawan and Uma, who provided me with the confidence and motivation I needed. To my sister Amrita, who despite being younger has managed to become wiser. I am very thankful for you continuously encouraging and keeping me grounded at the same time. To my parents Sarika and Ashwani, you have always encouraged me to take my time to find my own way, and have selflessly put my interests in front of yours to enable that. Mom, you were my first teacher and I would not have been able to get this far without watching you set an example for persistence every day. This thesis is as much a product of your efforts as mine.

Funding Acknowledgements:

The research on iron oxides was supported as part of FUTURE (Fundamental Understanding of Transport Under Reactor Extremes), an Energy Frontier Research Center funded by the U.S. Department of Energy (DOE), Office of Science, Basic Energy Sciences (BES).

The research on Tl_2LiYCl_6 was supported by the U.S. Department of Energy, Office of Science, Office of Basic Energy Sciences, Materials Sciences and Engineering Division, under Contract No. DE-AC02-05-CH11231 (Materials Project program (KC23MP)).

This research used resources of the National Energy Research Scientific Computing Center, a DOE Office of Science User Facility supported by the Office of Science of the U.S. Department of Energy under Contract No. DE-AC02-05CH11231 and the Bridges-2 system, which is supported by NSF award number OAC-1928147 at the Pittsburgh Supercomputing Center (PSC).

Chapter 1

Overview

The research presented in this thesis focuses on understanding the localized electronic states created by point defects and bound excitons in complex systems through the lens of two very different applications. Studies of iron oxides is motivated by an overarching effort to develop an atomistic understanding of point defects influencing the tranport properties of irradiated oxide systems. The work on Tl_2LiYCl_6 focuses on the interplay between the local structural distortions and localized bound excitons states responsible for scintillation. The subsequent chapters in the thesis are arranged as follows:

Chapter 2 begins with an introduction to important concepts and previously performed research on structure and point defects in magnetite(Fe_3O_4) and defect complexes in related oxide systems. The ideas and papers cited motivate my research on sampling multiple local environments and their associated effects on the underlying defect properties in magnetite in chapters 4 and 5. Chapter 4 focuses on energetics associated with charge ordering in bulk magnetite and how the short-range ordering of Fe^{2+}/Fe^{3+} cations in the high temperature disordered cubic phase can be similar to the long-ranged order in the low temperature monoclinic phase. The results and discussion for oxygen vacancies presented in chapter 5, then focuses on understanding how this ordering impacts oxygen vacancy defect properties. Recognizing that compared to mono-vacancies, the iron-oxygen di-vacancy is less studied and could be important for understanding defect behavior under irradiation conditions, chapter 6 focuses on this defect in both magnetite and hematite. Specifically we calculate the driving force for these vacancies to bind, finding that both in magnetite (Fe_3O_4) and hematite (Fe_2O_3) the di-vacancy complex is stable with respect to decomposition into isolated iron and oxygen vacancies and localized hole (in case of Fe_3O_4) and electron (in case of Fe_2O_3) polarons. Similar to mono-vacancies in magnetite (Fe_3O_4), the formation energies of di-vacancies also depend on charge ordering around the defect site.

The later part of chapter 2, focuses on an ordered double halide perovskite system (elpasolite), Tl_2LiYCl_6, studied as an intrinsically activated scintillator material. Owing to the importance of structural distortions in determining the bulk electronic structure, chapter 2

provides a brief overview of previous work done on different structural phases for these systems. Then a brief discussion on the role of Tl^+ cation in determining the local structure and as an activator ion is provided. These concepts aid the analysis of bulk Tl_2LiYCl_6 phonons, distortion modes and resulting Tl*s*-Cl*p* hybridization in chapter 7, which ends with description of different configurations of bound excitons in the lowest energy structure of Tl_2LiYCl_6. Throughout chapter 7, comparisons are made with non-Tl containing elpasolite systems to highlight the role of Tl^+ ions in developing intrinsically activated halide scintillators.

For both of the oxide systems and Tl_2LiYCl_6, the details of the computational methods employed in the work are provided in chapter 3. The final chapter of the thesis provides conclusions and suggestions for future work related to the topics presented in the thesis.

Some sections of chapters 2, 3, 4 and 5 are adapted from my previously published work *Density Functional Theory Study of Local Environment Effects on Oxygen Vacancy Properties in Magnetite. J. Phys. Chem. C 2023, 127 (35), 17460–17472* and are reproduced in this dissertation with permission of the co-authors.

Chapter 2

Background

The work presented in this thesis aims to understand electronically localized point defects and self trapped excitons in materials which exhibit a tendency to form multiple local environments in room temperature phases. Unless explicitly included in the form of entropy contributions, dynamic structural vibrational modes, renormalization of band structure, etc. Density Functional Theory(DFT) does not explicitly account for the realistic finite temperature behavior of these materials and the localized electronic states formed as a result of formation of point defects, electron and hole polarons and self-trapped excitons. Including these effects requires significant computational power and methods which are usually expensive to implement on large system sizes. Keeping these limitations in mind, it makes practical sense to utilize the ground state DFT calculations as much as we can, before performing calculations with higher methods which usually involve including many body interactions, along with other computational approaches to include temperature effects in the form of vibrational and configurational entropy contribution to the defect energetics.

The two material systems involved in the ab-initio simulation results in this thesis are iron oxides (magnetite (Fe_3O_4) and hematite (Fe_2O_3)) and Tl based ordered halide double perovskites (Tl_2LiYCl_6). While these materials classes have widely different chemistry and applications, they both provide interesting albeit challenging opportunities to study how point defects (in case of Fe_3O_4) and self trapped excitons (in case of TLYC), both with their own localized electronic structure, interact with the different local environments formed in these materials. In the remaining part of this chapter, I aim to provide a brief overview of our understanding of the bulk structure and previous experimental and computational studies of defects in these materials (Fe_3O_4, Fe_2O_3 and Tl_2LiYCl_6), which will explain my motivation and approach towards simulating point defects and self-trapped exciton properties. The review provided in this chapter is by no means comprehensive, but hopefully will provide the essential background for the results and discussion presented in subsequent chapters.

2.1 Fe_3O_4 (Magnetite): Charge ordering in bulk and point defects

Magnetite (Fe_3O_4) is a technologically important transition-metal oxide that continues to be actively investigated for a range of properties and processes. It is one of the constituent phases in the mixed-oxide layers formed upon corrosion of iron through oxidation in air or in aqueous environments [1, 2, 3]. It also finds applications in catalysis, e.g., for water gas shift reactions, industrial wastewater decontamination and surface mediated reduction of uranyl. [4, 5, 6, 7]. Further, it has been studied extensively for applications in spintronic devices [8, 9]. For such applications, and also to understand the geochemistry associated with magnetite minerals, an important issue is the role of point defects, including the intrinsic oxygen and iron vacancies, interstitials, and associated clusters that have been reported to form at different temperatures and oxygen partial pressures [10, 11, 12, 13].

Bulk structure of magnetite

To highlight the structural complexity associated with magnetite at low and intermediate temperatures, we briefly review experimental findings related to charge and spin ordering in Fe_3O_4. Above the (monoclinic-cubic) Verwey transition temperature of ∼120 K, magnetite forms in a cubic inverse spinel structure with the oxygen anions forming a face-centered-cubic arrangement, and the iron cations occupying both tetrahedral and octahedral interstices of this oxygen sublattice, as illustrated in Fig. 2.1. In an ionic bonding picture, tetrahedral sites are occupied by Fe^{3+} cations, while the octahedral sublattice is occupied by a 1:1 mixture of Fe^{3+} and Fe^{2+}. At very high temperatures (above ∼ 500 K), the extra electron for the Fe^{2+} cations on the octahedral sublattice are understood to be delocalized [14].

By contrast, for intermediate temperatures between the Verwey transition and ∼370 K, experimental measurements [14, 15] are more consistent with a model in which these charges localize, such that the structure can be described as having a disordered mixture of Fe^{2+} and Fe^{3+} over the octahedral sublattice sites. While these cations are disordered, experimental evidence suggests that the distribution is not random, but rather characterized by local short-range order that increases as the temperature is lowered [14, 15, 16].

Below the Verwey temperature, the Fe^{2+} and Fe^{3+} cations undergo an ordering transition to form a long-range-ordered pattern over the octahedral sublattice [17, 18]. The nature of the charge order was experimentally determined by X-Ray diffraction measurements, which established the presence of electron localization over multiple octahedral Fe sites[17, 18], that are coupled with local lattice distortions. The structure is illustrated schematically in Fig. 2.2. The charge ordering leads to a breaking of the cubic symmetry, to form a long-range ordered structure with a monoclinic space group. Without structural distortions, the relationship between the lattice vectors in this monoclinic structure ($\mathbf{a}_i^{monoclinic}$) and

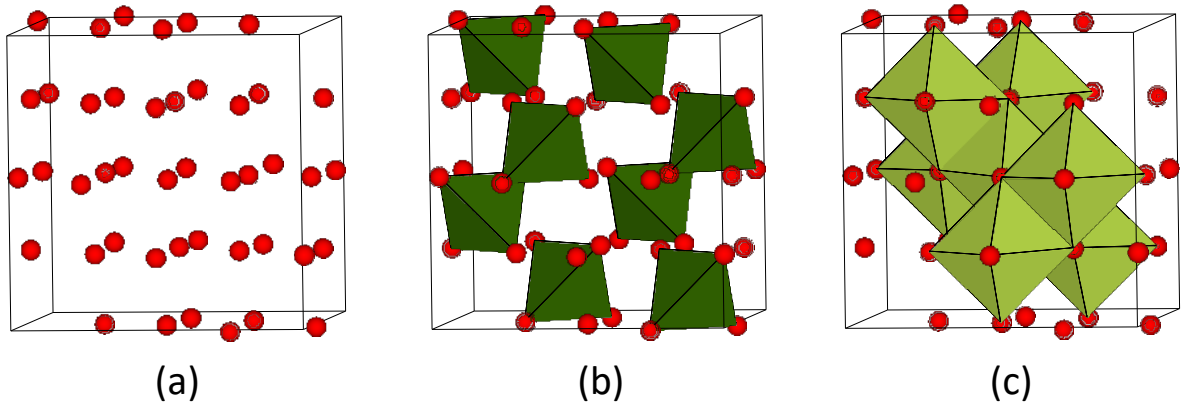


Figure 2.1: Schematic illustration of the cubic inverse spinel structure for magnetite, showing the calculated relaxed positions and coordination of representative ions. Panel (a) shows only oxygen anions (red circles), which form a face-centered cubic sublattice. The iron cations are distributed on two different sublattices, each consisting of (b) tetrahedrally coordinated sites occupied by Fe^{3+} (as indicated by the dark green shading of the tetrahedra) and (c) octahedrally coordinated sites occupied by both Fe^{3+} and Fe^{2+} cations (as indicated by the lighter green shading of the octahedra). The edges of the cubes correspond to the lattice vector directions for the conventional unit cell for the cubic inverse spinel structure.

the reference cubic structure (In the actual monoclinic structure the charge ordering is coupled with slight distortion of the unit cell, such that $a_2^{monoclinic}/a_1^{monoclinic} = 1.002$ and $a_3^{monoclinic}/a_1^{monoclinic} = 1.41$ (compared to the ideal values of 1 and $\sqrt{2}$, respectively) and the monoclinic angle takes a value of $\beta = 89.97°$ (compared with the reference value of 90°). In terms of the magnetic structure, magnetite is ferrimagnetic in the low-temperature monoclinic phase, and remains so above the Verwey transition temperature as the spins in tetrahedral and octahedral cation sublattice of the inverse spinel structure remain anti-aligned until about 850 K[19, 15].

Review of experimental observations on point defects in magnetite

Point defects generally play a central role in charge and ionic transport and are understood to have important effects on the electronic structure of magnetite[20]. Hence, their formation energetics, activation energies for diffusion, and electronic energy levels are of interest for developing theoretical understanding and predictive models of phase stability, kinetics and electronic properties[21]. However, despite extensive previous experimental and computational studies (as reviewed below), these point-defect properties remain incompletely understood, particularly for temperatures below roughly 370 K where the magnetite structure is known to be complicated by the presence of local or long-range charge, spin and

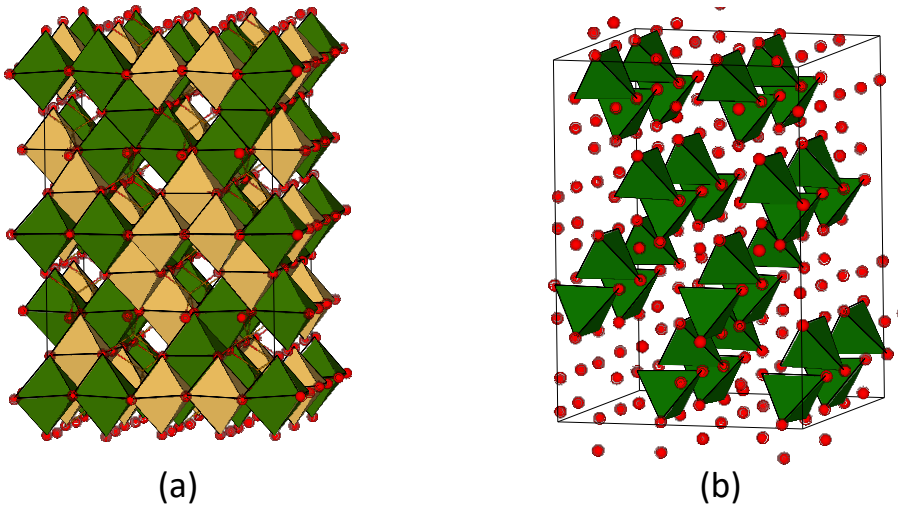


Figure 2.2: Schematic illustration of the low-temperature monoclinic phase of magnetite with its 224 atom conventional unit cell. Panel (a) illustrates the ordering of Fe^{2+} (yellow octahedra) and Fe^{3+} (green octahedra) cations on the octahedral sublattice, while (b) shows the tetrahedral sublattice occupied exclusively by Fe^{3+} cations (green tetrahedra). Oxygen positions are indicated by red circles.

orbital ordering [15, 16, 22].

Insights into the nature of the intrinsic point defects in magnetite have been derived from experimental measurements of cation and anion diffusion as functions of oxygen partial pressure and temperature [11, 12, 13, 10, 23]. These studies have yielded activation energies for ionic diffusion, and have been analyzed within the framework of ionic defect models to conclude that the dominant defects under reducing conditions are iron interstitials and oxygen vacancies, transitioning to iron vacancies and possibly iron-oxygen di-vacancies under oxidizing conditions [11]. To date, all such studies have been undertaken at high temperatures, where magnetite displays a cubic inverse spinel structure in which the electrons become delocalized over cation sites on the octahedral sublattice, and charge transport is rapid and characteristic of a metal [24]. By contrast, scattering[16], transport[24], and spectroscopic [14] studies at lower temperatures provide evidence of semiconductor behavior, and short and long-range ordering of the (localized) charges and spins. Additionally, magnetic aftereffects measurements at room temperature [25, 26] have provided insights into localized charge redistribution around cation vacancies in the form of Fe^{3+}/Fe^{2+} redox.

Review of computational studies on point defects in magnetite

Experimental studies of point defect properties have been complemented by first-principles calculations based on density functional theory (DFT). For example, such studies in models of magnetite with half-metallic electronic structures [27, 28, 29, 30, 31] have shown that this character of the electronic structure is maintained after the formation of neutral oxygen and cation vacancies and cation interstitials, with no defect states introduced in the band gaps for either spin channel. Additionally, an octahedral site preference was predicted for cation vacancies, and energy barriers on the order of 0.70 eV were computed for vacancy-mediated cation hopping [30]. Recent studies on cationic defects in magnetite emphasized the coupling of orbital ordering with lattice distortions in the cubic supercells[32, 33]. Another DFT study[31], compared the doping mechanism in magnetite with other spinels, finding that magnetite readily forms cation vacancies. The motivation for the aforementioned study is based on the role of point defects in determining free carrier concentrations, which allows for tuning the plasmonic resonance.

These computational studies have yielded important insights, but they have not explicitly considered the effect of different local environments created due to charge ordering found in the experimentally determined magnetite structure at low temperatures[17, 18]. As discussed in chapter 4, we expect the local charge ordering in the cubic phase at temperatures above 120K to be derived from low temperature phase, which motivates the current study of point defects in the low temperature phase of magnetite.

Review of experimental and computational studies on vacancies in oxides

My research focused on enhancing the current atomic scale understanding of defects behavior in irradiated iron oxides. Irradiating oxides can initially knock cations and anions from their lattice sites, creating vacancies and interstitials, which can then relax back to an equilibrium structure. Previous work [34, 35] has demonstrated that these defects can sometimes form metastable clusters which have reduced mobility and therefore can take a long time to anneal or diffuse towards sinks such as grain bounderies and surfaces. Compared to mono-vacancies, cation-anion di-vacancies in iron-oxides are comparatively less studied both computationally and experimentally. Hence, here we review previous findings from computational studies of cation-anion di-vacancies in oxide systems[36, 37, 38], particularly $MgAl_2O_4$, a normal cubic spinel[38, 37].

Owing to the requirement of large supercell sizes which can incorporate the resulting lattice distortions and changes in local electronic structure, di-vacancy defects in ionic materials are usually studied computationally using classical potentials, which do not allow the ionic charge to change. As shown in chapter 6, in magnetite, the resulting electron redistribution around even a simple complex like an iron-oxygen di-vacancy can extend to 6-8

Åand is accompanied by the redox of Fe^{3+} and Fe^{2+} ions, which motivates the development of charge-aware and reactive force-fields which can capture these atomistic effects. Nevertheless, the work performed on $MgAl_2O_4$ is instructive in understanding the interactions at play in stabilizing these defects. The study[38] also compares the formation energy of these point defects calculated using DFT and classical potentials with and without polarization of ions and find that including effects of polarization in empirical force fields is necessary to capture the correct energetics of intrinsic defects and associated clusters in oxide systems. From the above-mentioned studies, the key insights are relative stability of two types of cation-anion vacancies in $MgAl_2O_4$: V_{Mg}-V_O and V_{Al}-V_O and difference in their diffusion mechanism. Since $MgAl_2O_4$ is a normal spinel, all the Mg^{2+} are on tetrahedral sites and Al^{3+} occupy the octahedral sites. The V_{Mg}-V_O di-vacancies are less stable than the V_{Al}-V_O ones and also decay to V_{Al}-V_O during the course of diffusion through the lattice, as seen in the Speculatively Parallel Temperature Accelerated Dynamics (SpecTAD)[37] simulations. For both of these di-vacancies, clustering of cation and anion vacancies reduces the mobility of point defects. Further discussion on similarity and differences of $MgAl_2O_4$ and Fe_3O_4 is provided in chapter 6.

Bound cation-anion di-vacancies are also found to be stable in other oxide systems, such as Lead Titanate ($PbTiO_3$)[36]. Specifically for iron oxides: magnetite and hematite, experimental studies have speculated existence of iron-oxygen di-vacancies to explain some of the observations. In magnetite, for oxygen rich conditions, the minority defect responsible for oxygen transport is hypothesized to be iron-oxygen di-vacancy in the tracer diffusion studies[23]. In the case of hematite (Fe_2O_3), a recent study[39] performed on irradiated hematite films points to the possibly strong interactions between defects on cation and anion sub-lattices which could lead to clustering and link the self-diffusion behavior of cation and anion defects. In our work, owing to computational limitations, we do not calculate any migration barriers or diffusion pathways for point defects. However, future work in this area will be extremely significant for developing models for oxide formation and are discussed in chapter 8.

In summary, in the work presented here, we extend previous computational studies by employing DFT to calculate properties of point defects for low-temperature structures where charge and spin ordering give rise to a variety of local atomic environments. In chapter 5, we focus on oxygen vacancies, and explore local-environment dependencies of point-defect properties in the low-temperature monoclinic magnetite phase, where Fe^{2+} and Fe^{3+} ions display long-range ordering over the octahedral sites of the inverse-spinel structure. Calculated results are presented that demonstrate a significant effect of changes in the local charge and spin environments on oxygen vacancy formation energies and charge-transition levels. The results thus suggest a complex coupling of defect properties with local charge and spin order around the defect, which is likely to have important consequences for ionic transport at temperatures where such order is pronounced. Prior to presenting the results for oxygen-vacancy defects, in chapter 4 we also consider calculated energies for different

configurational models of the cubic phase, which suggest that the calculated results for these defects in the monoclinic phase should be relevant also to the cubic phase for temperatures above the monoclinic-cubic transition where local charge ordering is anticipated. In chapter 6 on defect complexes in iron oxides, we describe the properties of iron-oxygen di-vacancies in magnetite and hematite. We begin by a brief discussion of iron vacancies in magnetite, focusing on the low temperature monoclinic phase to explore the effect of local environment on charge redistribution and formation energies. Then we present the results on formation energy, binding energy and charge redistribution around iron-oxygen di-vacancies for different configurations involving the oxygen vacancy environments described in chapter 5. We end the chapter by providing results and a brief discussion of iron-oxygen di-vacancies in hematite. The emphasis on di-vacancies is motivated by the possibility of formation of defect complexes under irradiation, as well as some previous experimental observations which allude to the presence of di-vacancies in iron oxides[23].

The point defect thermodynamics and transport properties in Fe_3O_4 (Magnetite) and Fe_2O_3 (Hematite) have been extensively studied experimentally, especially at higher temperatures. I have made an attempt to make connections to this body of research when possible. From the perspective of creating computational models which can capture essential and complex behavior of these systems, there is still significant room for progress and I present my suggestions on improving the results in this thesis in chapter 8 on Future Work.

2.2 Tl_2LiYCl_6: A Tl based elpasolite scintillator

Scintillators are an important class of materials with optical and electronic properties leading to emission of light upon excitation by incident high-energy electromagnetic radiation such as x-rays and gamma rays[40, 41]. These materials are used for many different applications including medical imaging, nuclear nonproliferation, cosmology and high energy physics[40]. The underlying sequence of processes behind the finally observed emission of light involves the transfer of energy from the incident radiation to ions called activator centers. This leads to the capture or formation of excitons at the activator sites, which upon recombination emit electromagnetic radiation, typically in the visible spectrum[42, 40]. The activator centers can be either dopant ions in the host materials, in the form of substitutional defects, or intrinsic in the bulk material. An important class of scintillators, which have been used for decades, consists of binary halides employed as the bulk host doped with various optically active ions such as Tl^+, Ce^{3+} and $Eu^{2+/3+}$[43, 44, 45, 40, 46], with thallium being one of the most commonly used dopants in scintillators. For example, Tl doped binary halides, such as NaI:Tl and CsI:Tl, are among the most heavily used scintillating materials for gamma ray detection [44, 47, 48]. In scintillators of this class, Tl^+ can be present as an intrinsic or extrinsic luminescent center. Similarly to Tl^+, Pb^{2+} and Sn^{2+} also have an ns^2 configuration, stabilized by relativistic effects, and have been used as activator centers in alkali halides for a long time[49, 50]. These ions act as efficient exciton trapping centers.

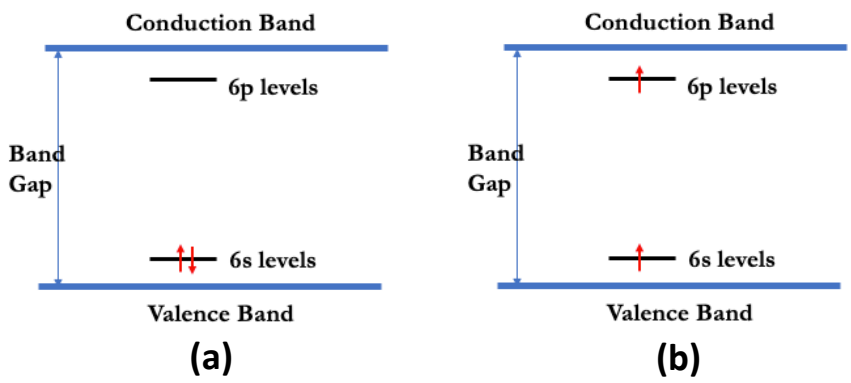


Figure 2.3: Schematic of a Tl^+ ion acting as an activator ion. When present as a dopant substituting a group 1 monoatomic ion such as Na^+, the occupied $6s^2$ orbitals and unoccupied 6p orbitals exist as localized states within the bulk band-gap. The Tl^+ ion can act as a site for exciton capture by trapping a hole in the $6s^2$ orbitals and subsequent capture of an electron in the 6p states. (a) and (b) describe the state of the system before and after the capture of electron and holes, leading to a bound exciton state.

Tl as an activator ion

For a dopant to act as an activator ion in a scintillator, it must be able to exhibit a radiative transition between a high energy and low energy state. Additionally, the radiation emitted from this transition should not be significantly absorbed by the scintillator material, so it can be detected by an external detector. Therefore, ions which can lead to localized electronic states in the band gap that can radiatively relax are often used as dopants in inorganic scintillators[48, 45, 51].

Tl is an element in the 3A group of the periodic table and in its neutral atomic state has the electronic configuration: [Xe] $4f^{14}5d^{10}6s^26p^1$. In ionic materials, Tl can be in the Tl^{3+} or Tl^+ oxidation state, depending on whether it gives up the electrons occupying the $6s$ states or not. The tendency of Tl to be more stable in the +1 state where the electronic configuration is [Xe] $4f^{14}5d^{10}6s^2$, with the $6s$ states still occupied, is often referred to as the "inert pair effect"[52, 53]. This behavior of s electrons in heavier elements like Tl is attributed to enhanced spin-orbit coupling (SOC) due to relativistic effects and can result in s electrons in the outermost shell existing as a lone-pair[54, 55, 56]. In a recent study[52], it was concluded that the formation of lone-pair is a result of an interplay of spin orbit coupling and hybridization with anion p orbitals, promoting local distortions around the cation site[56]. Tl^+ is optically active via the excited state $6s^16p^1$ to ground state $6s^26p^0$ transition[50, 47]. A schematic describing the single particle picture of the ground state and excited state of the Tl^+ ion, when acting as a doped activator ion, is shown in Figure 2.3. The excited state of alkali halides doped with Tl^+ as an activator ion results in a localized

exciton at the Tl site[44, 45]. In a single particle picture, this looks like a localized electron-hole pair on the Tl site. The formation of this configuration can be due to capture of an exciton at the Tl site or subsequent capture of an electron and then hole or vice versa[45].

Electronic structure of exciton states found in halide systems

Tl, when present as a dopant or part of the bulk in materials with halide ions (F^-, Cl^-, Br^- and I^-) can lead to multiple configurations of exciton states[44]. As described schematically in Figure 2.3, both electron and hole-like states of the bound exciton can localize on the Tl ion. In addition to these, the presence of halide ions provide an additional mechanism for localizing hole states called the V_k center[45]. This hole state can be visualized as a hole trapped between two Cl^- ions, formed by both ions reducing the distance between them. V_k centers are a common form of hole-like state found in binary halides and even in elpasolites of the same family as Tl_2LiYCl_6, such as Cs_2LiYCl_6[57]. As shown in the 7.1, Tl_2LiYCl_6 can form multiple stable electronic configurations for self-trapped excitons in the bulk, and two of them involve a V_k center. The relative stability of the excitons with and without a V_k like hole state can determine if Tl^+ ion can act as an intrinsic activator ion or if presence of other activator ions such as Ce^{3+}[40] is needed for designing an efficient scintillator material, like in the case of Cs_2LiYCl_6[57].

In the case of Tl^+ acting as an activator ion, the excited state configuration in alkali halides have an ns-np orbital character and leads to a complex fingerprint in the absorption spectrum for each host material determined by many effects[44]. These include the formation of self-trapped excitons with a variety of structures and the strong spin-orbit interaction associated with the thallium ion[56].

Structural distortions and bound exciton states in Tl_2LiYCl_6

Due to stabilization of the $6s$ electrons, Tl can also form purely covalent materials with sp bonding, such as the $TlCl_3$ molecule. As we will see later in chapter 7 for TLYC, although a wide-band gap ionic material, there is still a small level of covalent sp bonding between the Tl and Cl which changes the electronic properties of Tl_2LiYCl_6 in particular related to scintillation.

In addition to the above, Tl^+ ions can also display a dynamic Jahn-Teller effect due to $6s^2$ electrons [58, 59]. This leads to a complex structure of the absorption spectrum when used as a dopant in CsI[44]. Strong electron-phonon interaction are also known to have significant effects in the absorption/emission mechanisms of thallium doped alkali halides, causing broadening of absorption bands with increasing temperature and broad luminescence bands with large Stokes shift[47]. These properties result from a strong spin-orbit coupling and subsequent tendency of hybridization between $6s$ electrons and nearby halide p orbitals. These effects are usually coupled with local distortions, which further stabilize the orbital

hybridization. The distortion of local structure in the presence of Tl-X bonding, where X is a halide ion such as Cl^- has been studied in the literature[56], and it has been shown that the main driving force for this distortion is the lowering of anti-bonding interactions. We find similar effects in $Tl_2LiYCl_6$and the analysis is described in detail in sections 7.1 and 7.2.

More recently, ternary and quaternary halides are being considered for development of novel, more efficient scintillators. In this respect, the thallium high atomic mass is a very desirable feature to achieve higher stopping power, and materials where Tl^+ is present intrinsically i.e. in the undoped bulk, are emerging as candidates for development of more efficient scintillators [60]. Examples of such substitutions include crystals from perovskite (Tl_2LaX_5, X=Cl, Br, I) and elpasolite (Tl_2LiReX_6) families. In this respect, a relatively newer scintillator material is Tl_2LiYCl_6 (TLYC), an ordered double perovskite (elpasolite) structure with Tl^+ ion as the intrinsic activator ion in the bulk. Development of Tl_2LiYCl_6 as a scintillator material was motivated by the successful commercialization of Cs_2LiYCl_6 doped with Ce^{3+} as an efficient neutron and gamma ray detector material. Recently, ordered double perovskite halides (elpasolites) have been found to be efficient scintillators[61, 62] and Cs_2LiYCl_6 doped with Ce^{3+} has emerged as an example. The Ce^{3+} is a well known activation center with characteristic emission wavelength and fast emission[63]. When doped in Cs_2LiYCl_6, it acts as a site for exciton trapping and is responsible for the majority of observed light emission. Due to relatively smaller atomic mass of Cs^+, Cs_2LiYCl_6 has a low stopping power. To overcome this limitation, the substitution of Cs^+ with the heavier Tl^+ ion was considered. Contrary to Cs_2LiYCl_6 the observed spectra from Tl_2LiYCl_6 doped with Ce^{3+} showed that the majority of emission was not coming from the Ce^3[64]. Supported by the extensive studies on Tl^+ as a luminescence center when doped in other wideband gap insulators, it was hypothesized that the Tl^+ ions present in the bulk were responsible for the emission. In a Density Functional Theory study[57], it was found that a Y^{3+}-V_k like excited state is stable in Cs_2LiYCl_6. As described in 7.2, we find that even though V_k centers are stable in Tl_2LiYCl_6, the most stable exciton configuration is the one with hole-like state centered at Tl. In section 7.1, it is described how the high temperature cubic phase and subsequent lower symmetry phases show a distorted perovskite structure due to preferred local geometry resulting from hybridization of $6s^2$ electrons in Tl^+ with p orbitals from Cl^- ions. These distortions change the nature of the bound excitons from the one found in the undistorted analogue elpasolite structure, Cs_2LiYCl_6 (CLYC)[57].

Structure of Tl_2LiYCl_6

The structure of Tl_2LiYCl_6 has been studied using x-ray diffraction and neutron scattering techniques to assess the evolution of its structure as a function of temperature[65]. Similar to its Cs counterpart (Cs_2LiYCl_6), Tl_2LiYCl_6 is an $A_2BB'X_6$ ordered double perovskite, consisting of octahedral units of Li-Cl_6 and Y-Cl_6 and Tl at the 12 coordinated A site polyhedrons[65]. These Li-Cl and Y-Cl octahedral units are ordered and arranged alternately along the three axes. The cubic elpasolite phase of Tl_2LiYCl_6 has a $Fm\overline{3}m$ space

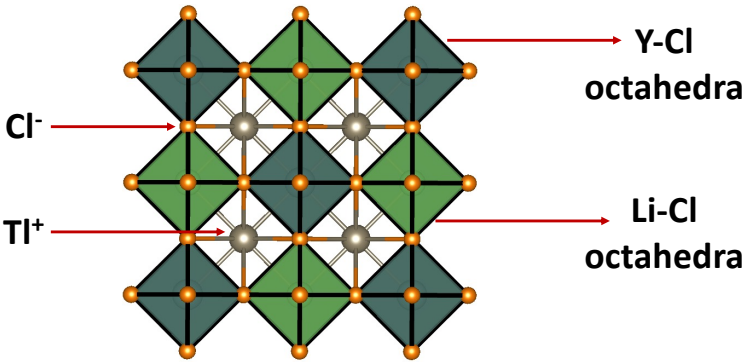


Figure 2.4: The 40 atom conventional unit cell for the cubic $Fm\bar{3}m$ phase of the elpasolite phase of Tl_2LiYCl_6. The gold and silver spheres represent Cl^- anions. The silver spheres represent Tl^+ ion in the A sites of the structure. The Li and Y ions are located in the B-site centered octahedra, indicated respectively with dark and light green shading.

group and a 40 atom conventional cell is illustrated in Figure 2.4. At lower temperatures, the structure of Tl_2LiYCl_6 deviates from this $Fm\bar{3}m$ symmetry, due to rotation of Li-Cl and Y-Cl octahedra and other distortions involving displacement of Tl^+ ions[65].

In the same study[65], it was found that Tl_2LiYCl_6 shows a structural phase transition with increase of temperature, from a tetragonal to cubic structure at 464K. In the low temperature tetragonal phase, Tl_2LiYCl_6 exhibits octahedral rotations, with Li-Cl and Y-Cl octahedra showing opposite rotations along the elongated tetragonal axis. No such rotations were found in the cubic structure resolved in x-ray diffraction and neutron scattering. Considering the possibility of dynamic distortions and limitations on time resolution for the above-mentioned experimental techniques[66, 67], we perform harmonic phonon analysis for the cubic phase and find that distortions also stabilize the cubic structure and these are similar to the ones found in the tetragonal and lowest energy triclinic phase of Tl_2LiYCl_6.

The theory of structural phase transitions in ordered double perovskite systems has been extensively developed.[68, 66]. In a comprehensive analysis of phase transitions across differ-

ent categories of ordered double perovskites[66], it was found that these systems can undergo multiple phase transitions from cubic to tetragonal to monoclinic phases, in the order of reducing symmetry. Depending upon the nature of the cations, these transitions can be of displacive, order-disorder or mixed character[69, 70, 68]. While the displacive nature mostly comes from octahedral rotation modes and polar displacement of cations, the order-disorder nature of the transition found in elpasolites with ammonium cation was attributed to different configurations of NH_4^+ cation in the octahedral cavity[66]. In principle, such local disordering can also occur in the cases where the charge density around the cation (for example, the ones with lone pair like Pb^{2+}, Sn^{2+} or Tl^+) is asymmetric, leading to multiple orientations stabilizing the local bonding by moving off the typical Wyckoff positions or exhibiting dynamic disorder. It was also pointed out that these systems (for example, $Cs_2NaNdCl_6$[66]) can show high anharmonicity in halide vibrational modes. Relative ionic size and lone pairs present on the A or B site cations play a crucial role in determining the final stabilizing distortion modes in perovskites[52, 71]. We rationalize that the distortions, with respect to the symmetric cubic structure in Tl_2LiYCl_6, might be present as dynamic distortions in the cubic phase. They influence the electronic character of the valence band and can play an important role in stabilizing the Tl centered exciton state, even at the temperatures where the thermally averaged final structure is observed to be cubic.

Chapter 3

Computational Methods

3.1 Electronic Structure Methods

When describing an interacting many-body system of ions and electrons under the Born-Oppenheimer approximation, the resulting Hamiltonian can be expressed as:

$$\hat{H}\Psi = (\hat{T} + \hat{V} + \hat{U})\Psi = E\Psi \tag{3.1}$$

where $\hat{T}, \hat{V}, \hat{U}$ are the kinetic energy, potential energy due to external field and electron-electron interaction respectively. For an extended system, exactly solving this equation becomes intractable, and the problem needs to be reformulated into other forms[72]. The primary computational method used in this research is Density Functional Theory (DFT). Since numerous comprehensive texts on DFT exist[72, 73, 74], here we give a very brief review and focus on the details more relevant to the research presented in this thesis. DFT for electronic structure allows the ground state energy to be expressed as a density functional instead of as a wavefunction functional[75]. The resulting equations are further reformulated using the Kohn Sham framework[76], which casts the problem in terms of a fictitious system of non-interacting electrons, chosen to have the same density as the real interacting system. The energy eigenvalues for the new *fictitious* system can be obtained by solving a system of equation

$$(-\frac{1}{2}\nabla^2 + V_{KS})\phi_i(\mathbf{r}) = \epsilon_i\phi_i(\mathbf{r}) \tag{3.2}$$

where

$$V_{KS}[n(\mathbf{r})] = V_{ion}(\mathbf{r}) + V_H[n(\mathbf{r})] + V_{XC}[n(\mathbf{r})] \tag{3.3}$$

with V_{ion}, V_H and V_{XC} denoting the ion, Hartree and the exchange-correlation potential, which can then be used to calculate overall density to solve the ground state energy functional.

$$n(\mathbf{r}) = \Sigma_{i=1}^{N}|\phi_i(\mathbf{r})|^2 \tag{3.4}$$

The Hartree potential term is defined as $V_H[n(\mathbf{r})] = \int \frac{d^3\mathbf{r'}n(\mathbf{r})}{|\mathbf{r}-\mathbf{r'}|}$ and can be thought of as a classical potential an electron experiences in the density field $n(\mathbf{r'})$ of the electrons. The exchange potential term is a quantum-mechanical term whose actual explicit functional form is not known and is the source of approximations. While the Kohn Sham formulation of DFT in itself is exact for calculating ground state properties, solving the above equation for most systems require making approximations about the electron exchange-correlation term. The research presented here is based on modifications of the Generalized gradient approximation (GGA)[77].

For the purpose of calculating bulk properties of correlated systems such as iron oxides and properties of systems with localized electronic states such as point defects in ionic systems (Fe_3O_4 and Fe_2O_3 in this thesis) and excitons (Tl_2LiYCl_6 in this thesis), we need to account for the self-interaction error inherent in the GGA approximation.

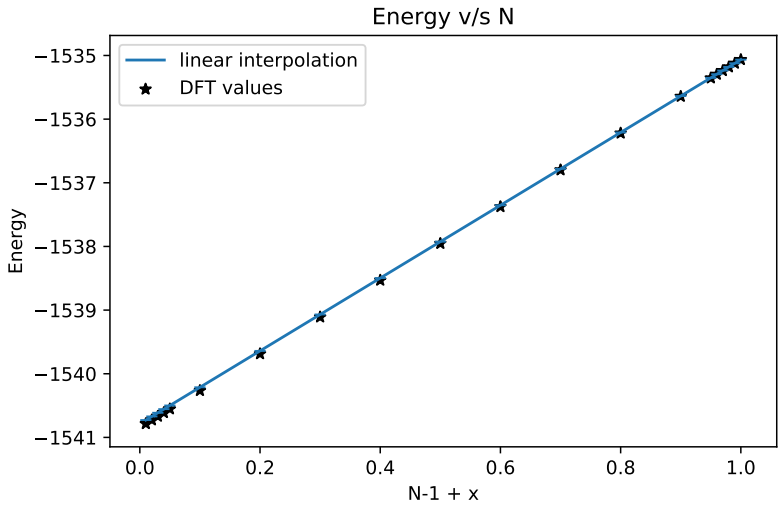


Figure 3.1: Dependence of total energy on number of electrons(N, defined relative to the neutral value) for the 224 atom monoclinic magnetite cell. The x-axis denotes the fractional number of electrons in the supercell, and the y-axis is the total energy from DFT+U calculation for U_{eff} = 4.1 eV

For systems with electrons occupying the relatively more localized d orbitals, such as iron-oxides, the self-interaction manifests itself in the form of delocalization of electrons resulting in incorrect electronic bandstructure[78, 79]. In this work, we employ the GGA+U correction scheme[79] which corrects for this delocalization error by utilizing a Hubbard-like term in the Hamiltonian to adjust the preference of an *nl* subshell to be occupied with respect to the rest of the system. A simplified final expression for the energy functional for

a single subshell nl is given as[79, 78]:

$$E^{DFT+U}[n(\mathbf{r})] = E^{DFT}[n(\mathbf{r})] + E^{Hub}[n^{I\sigma}_{m_l}] - E^{DC}[N^{I\sigma}] \tag{3.5}$$

where $n^{I\sigma}_{m_l}$ signifies the orbital on site I with magnetic quantum number m_l with spin index σ on which the Hubbard correction is applied to approximate the Coulomb energy associated with localizing an electron in that orbital. The $E^{DC}[N^{I\sigma}]$ term, which depends on the occupation of the orbital, accounts for removal of double-counting of interactions. This orbital dependent correction term promotes the localization of electron on certain orbitals with respect to others.

The self-interaction error in the GGA functional commonly manifests itself in the form of non-linear dependence of total energy on the amount of fractional charge added or removed from the system. Application of the +U correction can remove this non-linearity and this criterion has been chosen to select the +U value for magnetite in this work, as shown in figure 3.1. More details on this method are provided in previously published works[78, 80].

The methods described above improve the description of electronic states when the self-interaction error leads to delocalization of electrons in d-orbitals. We now pivot to electronic structure methods used to describe localized bound exciton states in Tl_2LiYCl_6. In this case, the s and p orbitals contribute to band-edges and we are not concerned with localizing electrons on subshells of particular sites in the bulk. Nevertheless, when describing localized electron and hole-like states created by hybridization of s and p orbitals, we need to reduce the delocalization caused by self-interaction in the GGA approximation.

An approach for correcting this self-interaction error (SIE), is to mix some fraction (α) of non-local exchange (E_X^{HF}) obtained from Hartree-Fock theory[72], with the semi-local exchange (E_X^{GGA}) obtained from GGA. The motivation behind mixing only a certain fraction of exact exchange is that semi-local exchange already includes some exchange contributions. In our case, we are using the PBE0 hybrid functional[81, 82] in which the local part is the PBE-GGA and non-local part is from the Hartree Fock exchange with mixing fraction α equal to $\frac{1}{4}$. In this formalism we have an exchange correlation energy of the form:

$$E_{XC}^{PBE0} = \frac{1}{4}E_X^{HF} + \frac{3}{4}E_X^{PBE} + E_C^{PBE} \tag{3.6}$$

where E_C^{PBE} is the PBE-GGA correlation. This form of hybrid functional with mixing fraction of 0.25, was proposed[81] based on the order of perturbation theory required to obtain desired properties for s-p hybridized systems by generally improving the description of localized states, due to reduced delocalization.

We employ PBE0 for simulating exciton states under the one particle approximation, to compare the exciton formation and corresponding emission energy across different configurations found in the lowest energy structure of Tl_2LiYCl_6. This approach has been previously

used to calculate exciton binding energies in an analogous system Cs_2LiYCl_6 [49], which we discuss in chapter 7 for comparison and understanding of the specific role of Tl-Cl bonding. Global Hybrid functionals such as PBE0, can be further improved upon by using system-dependent functional forms formulated to achieve the correct dielectric screening such as the dielectric-dependent range-separated hybrid functional based on the Coulomb-attenuating method (DD-RSH-CAM) and doubly screened hybrid functionals (DSH)[83, 84, 85, 86]. In future works, it would be worthwhile to explore whether these formalisms can provide a more accurate description of exciton and defect states in Tl_2LiYCl_6.

3.2 Computational Methods for magnetite (Fe_3O_4)

In this work, we present DFT-calculated properties of oxygen vacancies in the low-temperature monoclinic structure of Fe_3O_4. To understand the relationship between these results and associated defect properties in the cubic phase, we additionally undertake calculations of the relative energies of different supercell representations of this structure, possessing distinct models for the charge and spin ordering of Fe^{2+} and Fe^{3+} over the octahedral sites of the inverse spinel structure; the results are compared to measured transition enthalpies to assess the likely degree of short-range order in the cubic phase above the transition.

Supercell Models

The three different models for the structure of the cubic phase of Fe_3O_4 are illustrated in Fig. 3.2. Each model is based on a $2 \times 2 \times 2$ supercell of the conventional inverse spinel unit cell, containing 448 atoms. In model (a) the Fe^{2+} and Fe^{3+} are ordered over the sites of the octahedral lattice in the same pattern as observed in the low-temperature monoclinic phase, but the shape is constrained to be commensurate with the cubic inverse spinel structure; (b) corresponds to a special-quasirandom (SQS) structure, constructed by the gensqs method in the ATAT package [87, 88], where the Fe^{2+} and Fe^{3+} ions are modeled as being randomly arranged over the sites of the octahedral sublattice; (c) corresponds to a model where all sites on the octahedral sublattice are identical, such that the supercell maintains the full $Fd\overline{3}m$ space group symmetry of the cubic inverse spinel structure. In this high-symmetry model, where the octahedral Fe ions have the same local geometry, with undistorted Fe-O octahedra and identical Fe-O bond lengths, charge and spin cannot be identified as individual Fe^{3+} or Fe^{2+} cations.

DFT Calculation Details

DFT calculations, for both the above cubic supercell models, and the monoclinic structure considered for the defect studies, were performed using the projector augmented wave (PAW) method [89, 90], as implemented in the plane-wave-basis Vienna Ab-initio Simulation Package (VASP)[91]. The calculations made use of the Perdew-Burke-Ernzerhof implementa-

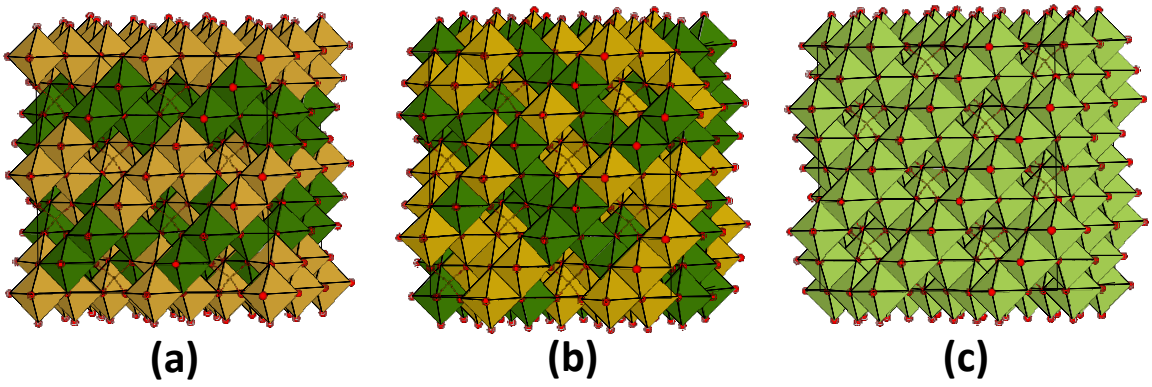


Figure 3.2: 448 atom supercells for cubic magnetite, representing different models for charge ordering on the octahedral sublattice. These models are created as a $2 \times 2 \times 2$ supercell of the conventional inverse spinel cubic unit cell, which consists of 56 atoms, making the total number of atoms equal to 448. This is in contrast to the monoclinic structure, which, in the conventional unit cell, contains 224 atoms. In each panel, only the oxygen positions (red circles) and octahedra (dark green, yellow and light green) are highlighted. All tetrahedral sublattice sites are occupied by Fe^{3+} (not shown). In panel (a) Fe^{3+} (dark green) and Fe^{2+} octahedral sites are ordered according to the configuration found in the low-temperature monoclinic structure (note that the cubic unit cells here are rotated relative to that for the monoclinic structure illustrated in Fig. 2.2). In panel (b) the Fe^{3+} and Fe^{2+} sites are arranged according to a special-quasirandom structure model for random configurational disorder on the octahedral sublattice. In panel (c) the light green octahedra denote an averaged Fe octahedral site with effective charge of 2.5

tion of the generalized gradient approximation (PBE-GGA)[77] with a Hubbard U correction applied to the Fe 3*d* electrons, based on the approach of Dudarev *et al.* [79]. Use was made of the PBE-GGA (POTCAR) potentials "Fe_pv" and "O" that include 3*p*,3*d*, 4*s* and 4*p* states (for iron) and 2*s* and 2*p* states (for oxygen) as valence, respectively.

A plane-wave cutoff of 520 eV and gamma-point k-point sampling was employed in the bulk structure optimizations for the 224-atom monoclinic and 448-atom cubic supercells. A reduced plane-wave cutoff of 450 eV and a gamma-only k-point sampling was used to relax the monoclinic cells with oxygen vacancies. Final energies were subsequently calculated using static calculations on the relaxed structures, with a gamma-centered $3 \times 3 \times 2$ k point mesh for the 224 atom monoclinic cell and $2 \times 2 \times 2$ k point mesh for the 448 atom cubic supercells, employing the tetrahedron integration method with Blöchl corrections [92]. Calculations were performed spin polarized with an energy convergence of 10^{-4} eV for electron density self-consistency, and force convergence of 0.01 eV/Åfor structural relaxations.

As discussed above, the value of the Hubbard model parameter U_{eff}=U-J was chosen based on the requirement of ensuring piecewise linearity for the energy versus electron occupation [93, 94, 95, 96, 78]. For the optimized bulk structure of monoclinic magnetite, this criterion leads to a value of U_{eff}=4.1 eV, which is close to that used in previous DFT studies of magnetite[97]. The +U correction was applied to Fe 3d states only. To investigate the sensitivity of the calculated results to the choice of the U_{eff} value, we undertook additional calculations obtained with a larger value of U_{eff}=5.3 eV (as used in Materials Project database for Fe due to better reproduction of thermochemical properties such as reaction enthalpies of Fe-O redox reactions [98, 99]). We find that the main effect of the higher value of U_{eff} is a lowering of the magnitude of oxygen vacancy formation energies, primarily due to a shift in the oxygen chemical potential. Importantly, this higher value of U_{eff} does not affect the main conclusions of the work concerning variations of defect structures and energies with local spin and charge environments.

Convergence to Targeted Charge and Magnetic Configurations

A primary focus of this work is to understand the effect of different local charge environments on defect properties, and hence it is essential that we are able to reproducibly converge each of the different calculations to a prescribed configuration of Fe^{3+} and Fe^{2+} ions. For the bulk monoclinic phase with and without an oxygen vacancy, as well as the different models for the cubic phase illustrated in Fig. 3.2, this was accomplished by introducing, at the beginning of the relaxation calculations, local distortions corresponding to octahedrally coordinated Fe^{3+} and Fe^{2+}. Specifically, the different Fe-O bond lengths around Fe^{3+} and Fe^{2+} sites were initialized by considering their average values in the relaxed monoclinic phase. On average, the calculated Fe-O bond lengths for Fe^{3+} centered oxygen octahedra were smaller than the corresponding Fe^{2+} centered octahedra by approximately 0.36 Å. Similarly, the magnetic configurations were seeded according to local moment of Fe^{3+} as 5 and Fe^{2+} as 4, assuming high spin configuration in an octahedral or tetrahedral coordination.

Once the systems were initialized as described above, we found that we were able to converge to the prescribed bulk charge and spin configurations by adiabatically ramping up the value of U_{eff}. Specifically, this value was ramped up gradually from values of 0.9 eV to the final value in sequential relaxation calculates with U_{eff} increased in increments of 0.2 eV. This methodology has previously been used in other complex oxides to avoid trapping the relaxed structure into a metastable state[100]. To identify the charge states on the Fe cations in the final relaxed configurations, we analyzed the values of the local moments, Fe-O bond lengths and the orbital occupancies. For the defect calculations, such analyses were especially important to ensure that the defect did not cause any long ranged effects on orbital occupation away from the ground-state configuration.

Methodology for Defect Calculations

Defect formation energies were calculated as a function of charge state employing the traditional dilute-density, grand-canonical formalism and appropriate corrections for artifacts arising from electrostatic interaction of image charges due to finite supercell sizes [101, 102, 103, 104, 105]. Specifically, the formation energy (E_{form}) of a defect in charge state q is given as:

$$E_{form} = E_{def} - E_{bulk} - \sum_{n=1} \mu_i \delta n_i + (E_f + E_{VBM})q + \delta E_{corrections} \tag{3.7}$$

where E_{def} is the total energy of the defect supercell, E_{bulk} is the reference total energy of the bulk supercell, μ is the chemical potential of atoms being added ($\delta n > 0$) or removed ($\delta n < 0$), E_f is the Fermi level referenced to valence band maxima (E_{VBM}) and $\delta E_{corrections}$ are the finite supercell size corrections [103].

In this work, for reducing conditions (the results on Oxygen vacancies in Chapter 5), the oxygen chemical potential (μ_O) required in Eq. 3.7 is set to a value corresponding to the zero-temperature reducing limit for magnetite, i.e., where bulk Fe_3O_4 is in equilibrium with Wustite-structured FeO. This value is obtained from the energies per formula unit for FeO and Fe_3O_4 as $\mu_O = E_{Fe_3O_4} - 3 * E_{FeO}$, where $E_{Fe_3O_4}$ was computed assuming the low-temperature monoclinic structure and E_{FeO} corresponds to FeO in a perfect rocksalt structure. For the defect formation energy calculations of iron vacancies and iron-oxygen divacancies, we have used chemical potentials corresponding to the oxidizing limit, given by the magnetite equilibrium with hematite (Fe_2O_3). This value is obtained from the energies per formula unit for Fe_2O_3 and Fe_3O_4 as $\mu_O = 3 * E_{Fe_2O_3} - 2 * E_{Fe_3O_4}$, where $E_{Fe_3O_4}$ was computed assuming the low-temperature monoclinic structure and $E_{Fe_2O_3}$ corresponds to Fe_2O_3 in a structure with R$\overline{3}c$ symmetry and anti-ferromagnetic magnetic ordering.

The formation energy of point defects is found to be generally sensitive to the accuracy of chemical potentials, and corrections to the DFT calculated energies are often employed to improve their accuracy [106, 107]. Here no such corrections have been applied, but could be added a-posteriori to adjust the defect energies reported here to correspond to improved models for the thermochemistry of the bulk phases. While such corrections would shift the values of the formation energies reported below, they would not alter the differences between calculated formation energies and binding energies of different charge and spin configurations of oxygen vacancies, iron vacancies and iron-oxygen di-vacancies for various local environments, which are the main focus of this work.

The values of the supercell corrections ($\delta E_{corrections}$) in Eq. 3.7 were derived using the formalism of Kumagai and Oba [103]. These *a posteriori* correction schemes are used in periodic-supercell charged-defect calculations to account for electrostatic interactions with periodic images, and include alignment of the electrostatic potentials in bulk and supercell systems. The approach of Kumagai and Oba[103] used here is an extension of the method

developed by Freysoldt et al[105, 101], and uses atomic site potentials rather than planar averaged potentials to account for systems with large atomic relaxations and anisotropic dielectric constants. The application of this approach requires knowledge of the dielectric constant, which was determined in the present calculations using density functional perturbation theory (DFPT) as implemented in VASP [108, 109]. Due to the high computational cost, we use a smaller 14 atom cell model for magnetite [110] to calculate the anisotropic dielectric tensor, with values varying between 13.19 and 19.76 for different crystallographic axes. To probe the effects of spin state of delocalized electrons arising from the introduction of an oxygen vacancy, we also perform constrained calculations for various values of the total magnetic moment of the supercell depending on the defect charge state.

3.3 Computational Methods for hematite

The computational methods employed in hematite DFT simulations are the same as the published work on thermokinetics[111], on which the work in this thesis is based. The choice of the same convergence parameters, pseudopotentials and +U values is made in order to compare the thermodynamics of iron-oxygen vacancy cluster (referred to as di-vacancy) and the electron polaron to the published data on iron and oxygen vacancies. For the same reason, we have also used the same chemical potential values and dielectric constants for the defect formation energy calculations.

3.4 Computational Methods for Tl_2LiYCl_6

Density Functional Theory simulations for structural relaxation, bulk electronic Density of States and harmonic phonon analysis in this work were performed using the Vienna Ab-initio Simulation Package (VASP) [112, 90]. Constrained Density Functional Theory simulations for modelling excited states were performed with CP2K [113, 114, 115, 116] using the PBE0[81] hybrid functional to accurately capture localized states. A more detailed description of simulation parameters is provided below for each type of calculation.

Details of structural relaxation and Density of States calculations

All DFT calculations performed using VASP [112, 90] employed the GGA-PBE functional [77], and the projector augmented wave (PAW) [91] method with a plane wave basis set. The unit cells of different ordered double perovskite halides (Tl_2LiYCl_6, Rb_2LiYCl_6, Cs_2LiYCl_6) were relaxed using a plane wave cut off of 520 eV for bulk structure optimization and a gamma-centered k-point mesh with density of 1000 k-points/atom until a force tolerance of 0.01 eV/Åfor ionic convergence, and an electronic self-consistency tolerance of 0.0001 eV was reached. To compute properties of unperturbed cubic elpasolite and tetragonal structures, the ion positions were initialized at the respective Wyckoff sites for the respective space groups while keeping the overall symmetry fixed during the structural relaxation.

Properties of perturbed supercells were created by applying an initial perturbation to ion positions by drawing the individual perturbations from a random distribution of magnitudes from a Gaussian distribution centered at 0.15 Å. The lattice constants of the supercell were kept fixed during the relaxation of perturbed supercells. The final energy and Density of States were calculated using the tetrahedral Bloechl method [92, 89] as implemented in VASP. The wavefunctions were further analyzed to look at bonding and anti-bonding character of Tl-Cl hybridization within Crystal Orbital Hamilton Population (COHP)[117, 118] analysis using the LOBSTER software [119, 120]. Electronic band structure calculations were also performed using VASP along the high symmetry pathways generated using the *seekpath* algorithm[121]. Final plots and calculation of electron and hole effective masses was performed using SUMO[122].

Phonon Calculations

The phonon band structure and phonon Density of States for cubic Cs_2LiYCl_6 and Rb_2LiYCl_6, and cubic and tetragonal phases of Tl_2LiYCl_6 were calculated using the Density Functional Perturbation Theory (DFPT) [123, 124] with non-analytical corrections for Born charges for cells with 40 atoms as implemented in VASP[124]. To get accurate force constants (second-order response to ionic displacement) from VASP DFPT calculations, a $4 \times 4 \times 4$ k mesh was used for the 40 atom conventional cells for cubic and tetragonal structures with an energy cutoff of 600 eV for the plane-wave basis and an energy convergence criterion of 10^{-8} eV. Phonopy [125] was used for parsing the calculated force constants and performing non-analytical corrections to account for long-range electronic screening due to polarization of electronic charges[109] from the Born effective charges also calculated using VASP[108]. The energy eigenvalues of the dynamical matrix at a point $\mathbf{q}$ in the Brillouin zone, were calculated along the high symmetry lines generated using *seekpath* algorithm[121], and the phonon dispersion was calculated and plotted by interpolation between those points using the plotting package SUMO[122].

Excited State

The excited state calculations were performed for a 320 atom tetragonal supercell using the PBE0[81, 82] hybrid functional as implemented in CP2K [113, 114, 115, 116]. CP2K uses a mixed Gaussian and Plane Waves basis approach [126, 127] in combination with the Auxiliary Density Matrix Method (ADMM) [128] for the evaluation of the exact-exchange and the Orbital Transformation (OT) method [129] for the wavefunction optimization. The efficient ADMM implementation of the exact exchange part of hybrid functionals in CP2K allowed us to simulate systems of hundreds of atoms as required to accurately model the atomic relaxation of the hole and exciton states which are localized in nature and cannot be effectively modelled using GGA approximation. We use GTH (Goedecker-Teter-Hutter) pseudopotentials [130, 131] and MOLOPT basis sets [126] as provided in CP2K library.

Excitons (electron-hole pair) states can be classified as singlet or triplet, depending upon the net spin they possess. This terminology is derived from the description of two spin-$\frac{1}{2}$ particle system in terms of the single particle spins to label the basis states, where there are three degenerate states with total Spin equal to 1 called the triplet states and one state with total spin angular momentum 0 called the singlet state. To generate a triplet-like excited state within the DFT approximation with single particle approximation, we used a constrained approach, where we fixed the multiplicity of the system to constrain the occupation to the different spin channels. The multiplicity(M) in our case is defined as $M = 2S + 1$, where S is the total spin angular momentum (sum of all the electron spins). For excited state calculation with collinear spins, we fix the multiplicity to 3 which forces the system to relax in a state where the HOMO (Highest Occupied Molecular orbital) and LUMO (Lowest Unoccupied Molecular orbital) state of the supercell representing excited state belong to different spin channels, creating an approximate triplet-like excited state. This is because the multiplicity equal to 3 in our system is achieved by removing an electron from the ground state HOMO and placing it in a higher unoccupied state. The net multiplicity is then given by $M = 2(\frac{1}{2}+\frac{1}{2})+1 = 3$, which we specify as a constraint in our PBE0 calculations of excited state. Classification of exciton singlet and triplet states in terms of net spin associated with them is not well-defined in the case of systems with strong spin-orbit coupling (SOC). This is because SOC couples the spin degrees of freedom with the lattice degrees of freedom, which no longer allows the independent description of spin degrees of freedom in terms of belonging to up and down spin channels[132]. Since s electrons in Tl show enhanced spin-orbit coupling (SOC) due to relativistic effects[54, 55, 56], a more accurate treatment of exciton states in Tl_2LiYCl_6 will require including this effect when calculating exciton configurations and binding energies. In the work presented in this thesis, we do not include the SOC effects in calculating properties of bound exciton in Tl_2LiYCl_6 and perform constrained collinear calculations using PBE0. Hence, in the subsequent text we refer to the excited state as triplet-like, even though that description is not well-defined for systems with strong spin-orbit coupling. The convergence criterion for relaxation of excited state structures is a force tolerance of 0.01 eV/Åfor ionic convergence, and an electronic self-consistency tolerance of 0.0001 eV.

To calculate the binding energy of excitons, we then employ the Δ-SCF approach[133, 134, 135, 136] where we take the difference in final energies of the two energy-minimized states with different constrained occupations, created as described above. This approach can be employed, for systems where the HOMO and LUMO states can be unambiguously identified, and their occupancy can be constrained (like our case of localized electron and hole states) in order to calculate the difference in total energies of excited and ground state. Constrained PBE0 calculations with Δ-SCF approach to calculate the binding energies has been used in previous studies of halide perovskites with localized bound states and shows a varying degree of agreement with experiment in the range of 0.1-0.6 eV, depending on the material[137, 138, 139]. This approach does not take into account the two particle character of the bound exciton state, and therefore does not capture the energetics and

correlation effects of interacting electron and hole states. Therefore, it is expected that the binding energies calculated using this method will be over-estimated with respect to the experimentally measured emission energies.

Chapter 4

Modelling Magnetite using DFT: Role of charge ordering

4.1 Results on Charge Ordering in Bulk Magnetite

In this section, we begin by comparing the bulk energetics of the low-temperature monoclinic structure of magnetite and the different supercell models of the cubic phase, described in the previous section. A comparison of these energies with measured transition enthalpies support the picture of pronounced short-range order at low to intermediate temperatures in the cubic phase, consistent with the long-range charge order in the monoclinic structure. Having thus established the relevance of the monoclinic ordering for higher temperature structures, we focus on the results for oxygen vacancy defects calculated in this low-temperature monoclinic structure, in the following chapters.

Charge-Ordering Energetics in Cubic Magnetite

The exact occupation of tetrahedral and octahedral sites by Fe^{3+} and Fe^{2+} ions depends on temperature. Magnetite is known to exist as an inverse spinel structure in its cubic phase at room temperature, with Fe^{2+} and Fe^{3+} cations disordered over the sites of the octahedral sublattice. Inverse spinels undergo two types of disordering transitions, generally with increasing temperature:

- Disorder of 2+ and 3+ cations in the octahderal sublattice where the tetrahedral sites remain occupied by 3+ cations
- Disordering of 2+ and 3+ cations between octahedral and tetrahderal sites where terahderal sites can also be occupied by 2+ charged cations.

This temperature dependent cation ordering has been explored in detail in previous studies of spinel systems[140, 141]. More specifically, thermochemistry and spectroscopic measure-

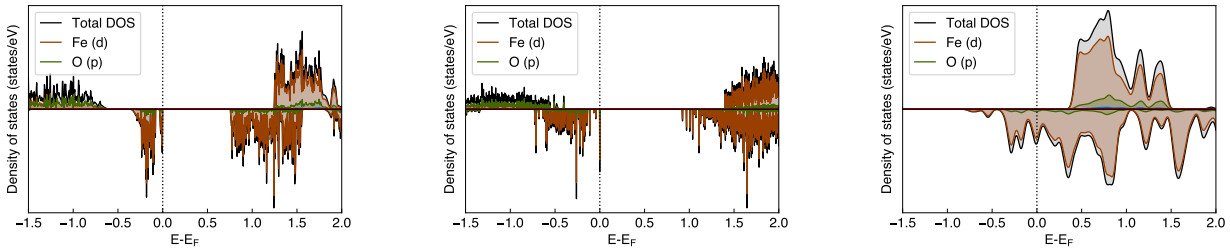
Cubic Supercell	Charge Configuration	Energy (meV/fu)
(a)	Low-Temperature Monoclinic Phase	1
(b)	Quasi-Random	57
(c)	Identical Charge States	233

Table 4.1: DFT-calculated energies for the three supercell models of the cubic phase of magnetite. The first column lists the supercell model as illustrated in Fig. 3.2, the second describes the configuration of the Fe^{2+} and Fe^{3+} cations over the octahedral sublattice, and the third lists the calculated energy difference, per formula-unit (fu), relative to the ground state low-temperature monoclinic phase.

ments on magnetite have established existence of an inverse spinel structure above the Verwey transition temperature with increasing degree of Fe^{2+}/Fe^{3+} cation mixing within the octahedral sublattice, and between octahedral and tetrahedral sublattice at higher temperatures.[142, 14]

Table 4.1 lists DFT-calculated energies for the three supercell models of the cubic phase of magnetite illustrated in Fig. 3.2. All the energy values are given per Fe_3O_4 formula unit (fu), relative to the low-temperature (T) monoclinic structure. The first model (a) is a supercell where the charge ordering for the Fe^{3+} and Fe^{2+} cations over the octahedral sites is identical to that of the low-T phase, but the supercell shape is structurally distorted relative to this monoclinic structure to be cubic. The energy difference associated with this cell-shape distortion is computed to be 1 meV/fu. In model (b) the Fe^{3+} and Fe^{2+} cations are disordered in a quasi-random configuration, while the supercell is again maintained to be cubic. This charge disordering raises the energy by 56 meV/fu relative to model (a). Finally, in model (c) the local distortions that stabilize the individual Fe^{3+} and Fe^{2+} charge states are disallowed, leading to a supercell where each octahedral cation has the same local geometry and charge, leading to a state that is 232 meV/fu higher in energy than model (a).

The relative energies of the different models for cubic magnetite can be compared to the measured latent heat for the Verwey order-disorder transition, which has been reported to have a value of 6.85 meV/fu [143]. This number is much closer in magnitude to the calculated energy difference between the low-T phase and model (a) for the cubic magnetite phase, than it is for models (b) and (c). Given that the disordering energy, i.e., the energy difference between models (a) and (b), is nearly an order of magnitude larger than this measured latent heat, this comparison suggests that there is significant short-range order in the charge configuration for the cubic phase near the Verwey transition. This conclusion is consistent with diffuse scattering measurements [15] that demonstrate that the electron localization patterns from the low-T phase survive as short-ranged correlations in the high temperature phase. It is also consistent with a recent study[14] involving a combination of theory and core-level



(a) Low temperature derived (b) Quasi-Random Ordering (c) Averaged charge

Figure 4.1: Electronic density of states for the three different charge ordering models on the octahedral sublattice for 448 atom supercells of cubic magnetite. The labels (a), (b) and (c) correspond to charge-ordering models described in 3.2. In this plot, the value of the Fermi energy (E_{Fermi}) corresponds to the highest occupied state. DOS for spin-up (spin-down) electrons are plotted as positive (negative) values.

X-ray spectroscopy measurements indicating that local charge environments similar to the low-temperature phase persist up to 330 K. Even above this temperature the charge order is only gradually broken with locally correlated Fe^{2+} and Fe^{3+} sites present up to 500 K [14].

The electronic density of states for the structural models described in Fig. 3.2a-3.2c, are plotted in Fig. 4.1a- 4.1c, respectively. The results illustrate that the presence of a band gap in the calculated electronic structure requires breaking the symmetry to allow for distinguishable Fe^{2+} and Fe^{3+} sites, as in Fig. 4.1a and 4.1b, while models that preserve the perfect cubic symmetry produce a half-metallic bandstructure, as in Fig. 4.1c.

Overall, the comparison of calculated results in Table 4.1 with experimental thermodynamic, scattering, and spectroscopy measurements suggests that understanding defect properties in the low-T monoclinic structure will likely provide insights into these same properties in the cubic magnetite phase at low to intermediate temperatures where local charge order similar to that in the low-T phase appears to be present. We thus proceed in the chapters that follow to focus exclusively on calculated results for the low-T phase, using the 224-atom unit cell illustrated in Fig. 2.2. We note that focusing on the low-T phase for these defect calculations, rather than any of the cubic supercell models, also presents a practical advantage in that it avoids the problem of defects triggering global structural transformations away from the bulk reference structure when performing relaxations in a supercell that is not the ground state.

Chapter 5

DFT Study of Local Environment Effects on Oxygen Vacancy Properties in Magnetite

In this chapter we present results of DFT calculations for oxygen vacancies in magnetite (Fe_3O_4) Results are obtained following the methods described in the section 3.2 in chapter 3.

5.1 Oxygen Vacancy Charge and Spin Environments

We categorize the local environment around the oxygen vacancies in magnetite in terms of the charge state of Fe ions in the nearest-neighbor shell *before the vacancy is introduced*. In the low-T monoclinic structure, each oxygen site is surrounded by four Fe ions, one of them belonging to the tetrahedral sublattice and the rest to the octahedral sublattice, as illustrated in Fig. 5.1. Due to underlying charge order, the tetrahedrally coordinated cation site is always occupied by Fe^{3+}, while the octahedral sites can be occupied by either Fe^{3+} or Fe^{2+}. This leads to the presence in the low-T phase of four different types of oxygen environments classified as having three, two, one, or zero octahedrally coordinated Fe^{2+}. In the following, we refer to the central oxygen-vacancy site and the nearest-neighbor shell of four cations as the "vacancy core" and the Fe ions in the next-nearest shell as "neighbors" to the core.

Depending on the oxidation state of Fe ions in the core, different charge and spin configurations associated with the oxygen vacancy can be found for neutral, +1 and +2 defect charge states. For example, the two excess electrons left behind by the formation of a neutral oxygen vacancy can be localized on the Fe cations within the core, localized on a neighboring Fe^{3+} cation (i.e., reducing it to Fe^{2+}) bound to the core, or a combination of these possibilities. Further, associated with these charge arrangements can be different spin configurations.

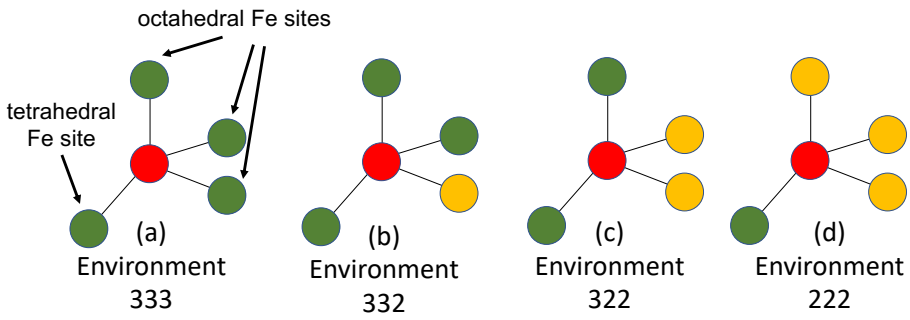


Figure 5.1: Fe coordination around O vacancy in bulk monoclinic. The red circles denote the oxygen site, the green and yellow circles denote Fe^{3+} and Fe^{2+} respectively. All the schematics (a)-(d) have the same arrangement for octahedral and tetrahedral sites as shown in (a) but differ in number of Fe^{3+}/Fe^{2+} ions occupying the octahedral sites.

To describe the charge and spin configuration of the oxygen vacancy we will use the following notation that extends the usual Kröger-Vink notation:

$$ENV : SPIN : CHARGE$$

where the environment (ENV=333, 332, 322, or 222) is specified by the charge on the three octahedral Fe cations within the core before the vacancy is introduced (see Fig. 5.1), the spin configurations ($SPIN$) of the excess electrons are specified as up (U) or down (D), and the charge configuration is indicated using Kröger-Vink notation for the core ($V_O^{\bullet}$, V_O or V_O') and bound electrons (Fe_{Fe}') or holes ($Fe_{Fe}^{\bullet}$) on Fe cations that are neighbors to, but outside, the core. In this notation, the spin configuration labels for the electrons are made with reference to the magnetic order in the low-T magnetite phase. Magnetite remains ferrimagnetic until about 850 K, and the net moments of Fe ions in the octahedral versus tetrahedral sublattices are oppositely aligned. We define the net spin of the octahedral sublattice as "spin-up" and that of the tetrahedral sublattice as "spin-down". By using constrained total magnetic moments in the DFT calculations, we can converge the defect calculations in different spin states to determine the lowest energy configuration. In the sections that follow we discuss first neutral vacancies, then positively charged vacancies, where the charge state is expressed relative to the bulk, and represents that of the total vacancy complex, i.e., including the core and any neighboring Fe atoms outside the core undergoing redox with localized holes or electrons bound to the core.

5.2 Neutral Oxygen Vacancies

Calculated formation energies (E_{form}) for neutral oxygen vacancies are listed in Table 5.1. Results are presented for each of the four charge environments illustrated in Fig. 5.1, the three spin configurations for the two excess electrons, and the corresponding charge configuration around the oxygen site prior to introducing the vacancy. A large spread of 1.09 eV (which is on the order of the formation energy itself) is calculated for E_{form} across the different defect states.

Environment	Spin Configuration	Charge Configuration	$E_{form}(eV)$
333	UD	V_O^X	0.96
	DD	V_O^X	1.80
	UU	$V_O^\bullet$-Fe'_{Fe}	1.18
332	UD	V_O^X	0.80
	DD	V_O^X	1.87
	UU	$V_O^\bullet$-Fe'_{Fe}	1.15
322	UD	V_O^X	0.85
	DD	V_O^X	1.81
	UU	$V_O^\bullet$-Fe'_{Fe}	1.10
222	UD	V_O^X	1.22
	DD	$V_O^\bullet$-Fe'_{Fe}	1.89
	UU	$V_O^\bullet$-Fe'_{Fe}	1.03

Table 5.1: Formation energies of neutral oxygen vacancies. The first three columns specify the environment, spin and charge configurations, and the fourth lists the corresponding calculated defect formation energy.

We discuss first the origin of the variations in E_{form} for the charge environments containing more than one Fe^{3+} ion in the vacancy core, i.e., environments labeled 333, 332 and 322 in Fig. 5.1. To facilitate this discussion we note that for the high-spin configurations present in magnetite (with electronic configuration of octahedral Fe^{3+} as ${t_{2g}}^3{e_g}^2$, tetrahedral Fe^{3+} as ${e_g}^2{t_{2g}}^3$ and octahedral Fe^{2+} as ${t_{2g}}^4{e_g}^2$), an extra electron from the neutral vacancy can occupy a low-lying t_{2g} orbital when Fe^{3+} is octahedrally coordinated, and a low-lying e_g orbital when Fe^{3+} is tetrahedral coordinated. In both cases, the added electron has spin opposite to the previous net local moment on that ion, thus reducing the net local moment on that sublattice.

The top three rows of Fig. 5.2 illustrate the calculated spin and charge configurations for the three charge environments with more than one Fe^{3+} cation. The figure highlights the fact that, since the spins of the additional electrons are strongly tied to the Fe sublattice to which they are localized, constraining the electrons to be in any one of the three spin

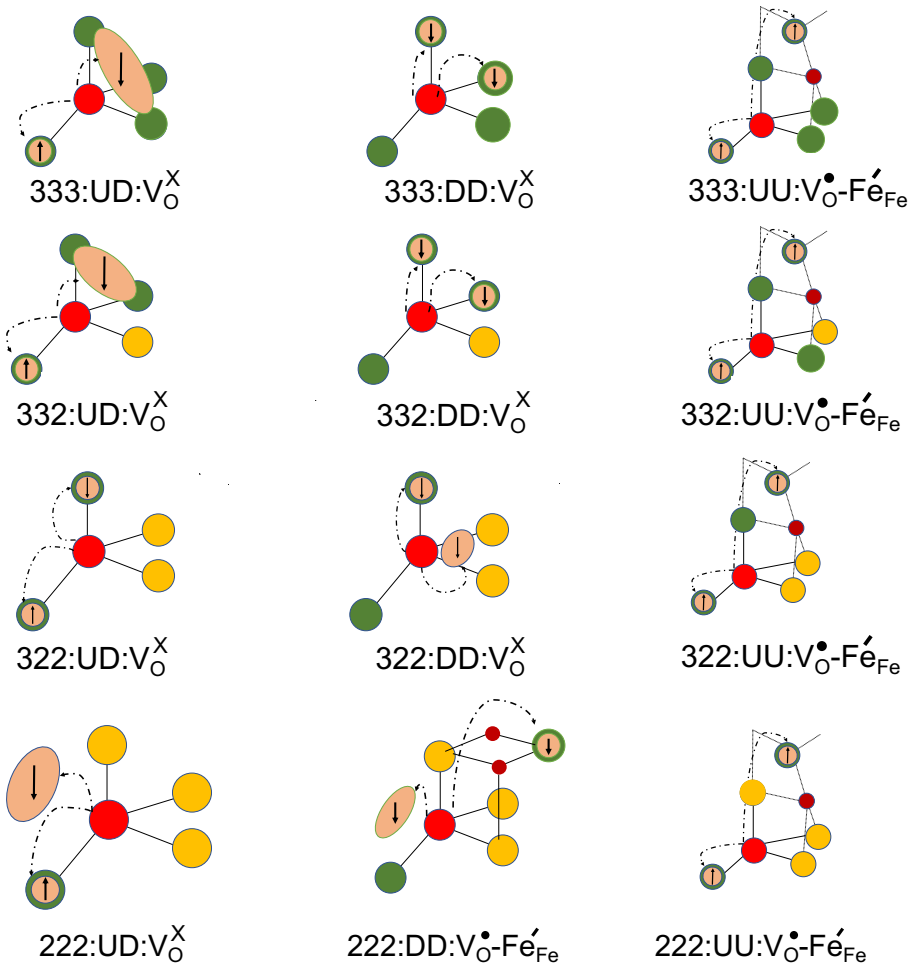


Figure 5.2: Charge redistribution around a neutral oxygen vacancy for different spin states of the excess electrons for 333 (first row), 332 (second row), 322 (third row) and 222 (fourth row) charge environments. Images in the left, middle and right column correspond to Up-Down, Down-Down and Up-Up spin configurations, respectively. In each figure, the location of the extra electrons is shown schematically as an orange circle or an ellipse connected by dashed lines to the position of the removed oxygen ion (red circle). For cases where the electron is localized on an Fe^{3+} ion (green spheres) the orange electron cloud is centered on that ion. For the case where the electron is distributed between sites, the orange ellipse is centered off an ion site. Fe^{2+} ions are shown as yellow spheres. The arrows indicate the spin state (up or down) of the electrons. The small red spheres indicate oxygen sites outside the vacancy core centered on the central, larger red sphere.

configurations also changes the Fe sublattice on which it ends up. Specifically, the UU configuration, Fig. 5.2 right column, leads to both electrons being localized on Fe^{3+} ions on the

tetrahedral sublattice, one within the core and one in a neighboring tetrahedral site. For the DD configuration, Fig. 5.2 middle column, the electrons localize on two octahedral Fe^{3+} sites within the core for configurations 333 and 332, while for 322 one electron localizes on an octahedral Fe^{3+} and the other is localized between the remaining ions in the core. For the UD configuration, Fig. 5.2 left column, the "spin-up" electron is always localized on the tetrahedral coordinated Fe^{3+} inside the vacancy core, while the"spin-down" electron can be localized on a single or multiple Fe^{3+} sites, depending on how many Fe^{3+} are inside the vacancy core. The different charge and spin configurations illustrated in Fig. 5.2 result in the differences in formation energies for neutral oxygen vacancies listed in Table 5.1. For each of the charge environments with more than one Fe^{3+} in the core, we find that the energetically most favorable spin configuration is UD, i.e., with the two excess electrons having opposite spin. This result is consistent with the finding from a previous computational study[27] on oxygen vacancies in magnetite that a small concentration of oxygen vacancies does not change the overall net magnetic moment of the material.

We consider next the case of a neutral oxygen vacancy where there is one Fe^{3+} within the vacancy core, i.e., the environment labeled 222 in Fig. 5.1. As shown in Table 5.1, the dependence of formation energies on the electron spin configuration differs qualitatively from the cases described above. Specifically, for the 222 environment, the lowest energy state corresponds to both electrons occupying the spin-up channel (UU). This result can again be analyzed by considering how the two excess electrons are distributed on Fe sites around the vacancy site, as illustrated in the bottom row of Fig. 5.2.

For the UD spin configuration, one of the electrons is localized on the tetrahedral Fe^{3+} ion present in the vacancy core, with the other occupying a much more delocalized state formed from hybridization of the d orbitals of the three Fe^{2+} octahedral ions. As shown in Table 5.1, the value of E_{form} in this configuration is 0.26-0.42 eV higher than those for the UD spin configurations for the charge environments containing more than one Fe^{3+} in the core. As can be seen from the density of states in Fig. 5.3(b), this higher-energy state correlates with the presence of a high-energy mid-gap impurity state related to the delocalized electron.

The lowest-energy neutral oxygen vacancy for the 222 environment corresponds to the UU spin configuration illustrated in Fig. 5.2. Here the electrons localize on tetrahedral Fe^{3+} ions, one in the vacancy core and the other in a neighboring tetrahedral site. As shown in Fig. 5.3(c), the stability of this state correlates with the absence of a mid-gap state, in contrast to the UD spin configuration. The preferential localization of electrons on Fe^{3+} rather than Fe^{2+} can be rationalized by the observation that Fe ions prefer to exist in 2+ and 3+ valence state, as evidenced by prevalence of naturally occurring oxides such FeO, Fe_2O_3 and Fe_3O_4.

To understand the role of lattice relaxations, we also compared the net structural relaxation around the vacancy site for all the local environments and spin configurations for

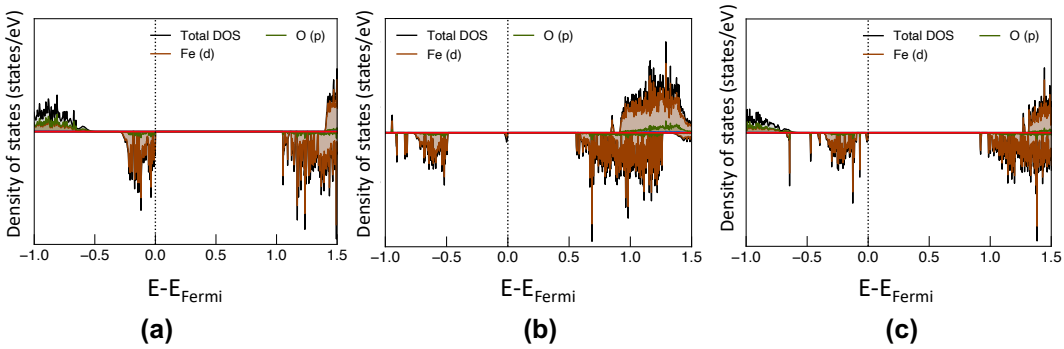


Figure 5.3: Total and partial electron density of states (DOS) for (a) bulk monoclinic Fe_3O_4, and neutral oxygen-vacancy supercells with (b) 222:UD:V_O and (c) 222:UU:$V_O^{\bullet}$-Fe_{Fe}' defect configurations. The mid-gap electronic state in the 222:UD:V_O oxygen vacancy is absent for the 222:UU:$V_O^{\bullet}$-Fe_{Fe}' configuration. In this plot, the value of the Fermi energy (E_{Fermi}) corresponds to the highest occupied state. DOS for spin-up (spin-down) electrons are plotted as positive (negative) values.

the neutral oxygen vacancy, and found the changes in bond lengths with respect to the unrelaxed structure (bulk 224 atom cell with the oxygen atom removed) across different spin configurations to be very similar. This emphasizes the dominant role of electrostatic and exchange interactions in determining the relative stability of different spin configurations and the energetic favorability of the neutral core for the 333, 332 and 322 environments. We note that the 332:UD:V_O configuration involves an electron shared between two Fe ions that were initially in the 3+ oxidation state, and this configuration could in principle result from pre-existing symmetries in the initial configuration. To check this, we performed two additional relaxation runs for the 332:UD:V_O configuration with initial states perturbed to break symmetry: (a) we explicitly created a distorted local environment on a Fe^{3+} outside the vacancy core to promote localization of an electron on that site and (b) we applied random perturbations to all ions in the initial structure, where the displacement vectors were drawn from a normal distribution of standard deviation 0.15 Å. In both cases, the relaxation did not lead to a lower energy structure or localize the electron on a single Fe^{3+} in the vacancy core Thus, at this level of DFT theory, the configuration with the electron shared between the two Fe^{3+} cations appears to be the lowest-energy defect configuration state for the 332:UD:V_O oxygen vacancy.

5.3 Positively Charged Oxygen Vacancies

Calculated formation energies (E_{form}) for positively charged oxygen vacancies are listed in Table 5.2, for the value of the Fermi energy corresponding to the bulk system's valence band maximum (VBM), i.e., for $E_f = 0$ in Eq. 3.7. Results are presented for +1 and +2 de-

fect charge states in each of the four oxygen environments illustrated in Fig. 5.1. For the +1 defect charge state, the lowest-energy configuration corresponds to the extra electron taking the spin-up configuration and formation energies for only this configuration are presented. A spread of 0.12 eV is calculated for the values of E_{form} for the +1 charged vacancies. Only one localized +2 charged vacancy configuration is found to be stable in the calculations, as described below.

Environment	Defect Charge	Spin Configuration	Charge Configuration	Hole Binding Energy (meV)	$E_{form}(eV)$
333	+1	U	V_O^X-$Fe_{Fe}^\bullet$	70	0.55
	+2	N/A	V_O^X-2$Fe_{Fe}^\bullet$	120	0.27
332	+1	U	V_O^X-$Fe_{Fe}^\bullet$	60	0.43
322	+1	U	V_O^X-$Fe_{Fe}^\bullet$	10	0.50
222	+1	U	$V_O^\bullet$	N/A	0.48

Table 5.2: Formation energies of positively-charged oxygen vacancies. The first column specifies the environment, the second the defect charge, and the third and fourth the spin and charge configurations, respectively. The fourth column lists the calculated binding energy of the localized holes to the vacancy core (with "N/A" implying the defect configuration does not involve a localized hole). The corresponding calculated defect formation energy is given in the final column.

We consider first the +1 charged oxygen vacancies for the three oxygen environments containing more than one Fe^{3+} cation in the core, i.e., the 333, 332 and 322 environments illustrated in Fig. 5.1. The lowest-energy defect states in these cases can be understood with reference to the lowest-energy defect configurations for the neutral vacancies, by the binding of a localized hole ($Fe_{Fe}^\bullet$) on an Fe^{2+} cation (thereby oxidizing it to Fe^{3+}) that is outside, but a nearest neighbor to, the vacancy core. The resulting +1 charged V_O-$Fe_{Fe}^\bullet$ defect structures are illustrated in the case of the 332 environment in Fig. 5.4(a).

An important consideration related to the stability of these defects is the magnitude of the binding energy of the localized hole to the vacancy core, as reported in the fifth column of Table 5.2. These binding energies are computed from the difference in formation energy of the charged defect cluster, and the formation energies of the neutral vacancy and an isolated $Fe_{Fe}^\bullet$ hole localized on a Fe^{2+} in the bulk magnetite structure. For the latter, we use the lowest polaron formation energy out of the eight different Fe^{2+} Wyckoff sites. For the oxygen vacancies in the 333 and 332 configurations these calculated binding energies are large in magnitude, ranging between 60-70 meV, suggesting that the V_O-$Fe_{Fe}^\bullet$ are stable with respect to dissociation into isolated V_O and $Fe_{Fe}^\bullet$ defects up to relatively high temperatures (since, e.g., $T = E_b/k_B$ ∼812 K for a binding energy of E_b=0.07 eV). For the oxygen vacancies at the

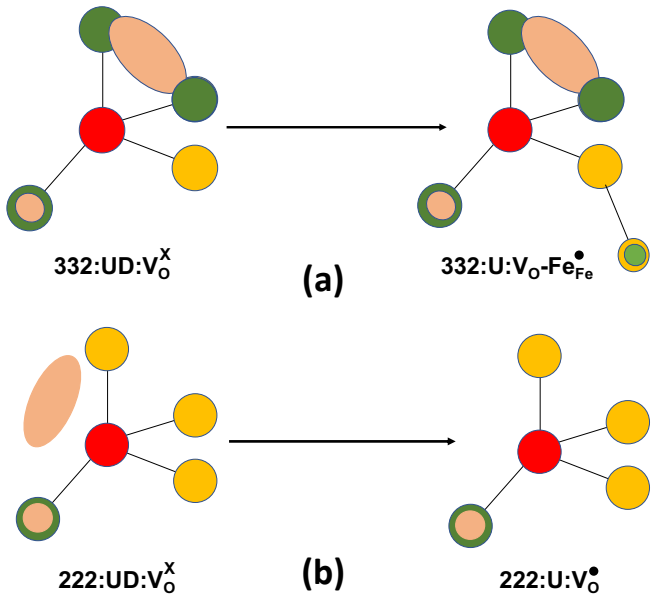


Figure 5.4: Charge redistribution around a +1 charged oxygen vacancy for (a) the 322 environment containing more than one Fe^{3+} in the vacancy core, and (b) the 222 environment containing one Fe^{3+} in the vacancy core. For both cases, the configuration of the corresponding neutral vacancy is shown on the left and that of the positively charged vacancy on the right. As in Fig. 5.2, the location of the extra electron is shown schematically as an orange circle or ellipse. The green circle on the top right figure is the localized hole on the octahedral Fe^{2+} site outside the vacancy core.

322 site, the polaron binding energy is comparatively much smaller in magnitude and would be expected to dissociate into a distinct neutral vacancy and isolated hole at relatively low T.

As was the case for the neutral vacancy, the stable configuration for the +1 charged oxygen vacancy in the 222 environment is distinct from that for the environments containing more than one Fe^{3+} cation in the core. In this case, illustrated in Fig. 5.4(b), the core itself becomes positively charged and there are no bound holes. This $V_O^{\bullet}$ configuration can be viewed as a result of removing the delocalized core electron or the bound electron in the 222:UD:V_O as illustrated in Fig. 5.4(b) (or, equivalently by removing the bound electron in the lowest energy 222:UU:$V_O^{\bullet}$-$Fe_{Fe}^{\prime}$ neutral configuration).

Finally, we consider +2 charged oxygen vacancies. In this case, we were only able to stabilize the doubly charged state for the 333 oxygen environment. In this case, the defect configuration corresponds to a configuration V_O-$2Fe_{Fe}^{\bullet}$, corresponding to the binding to the neutral vacancy core of two $Fe_{Fe}^{\bullet}$ holes localized on Fe^{2+} cation sites that are nearest neighbors to the vacancy core. In Table 5.2 we include the calculated value of the binding of the

second hole to the corresponding +1-charged V_O-$Fe^{\bullet}_{Fe}$ defect, which is large in magnitude, with a value of 120 meV. For the remainder of the charge environments we found that the localized holes formed in a +2 charged supercells were not bound to the vacancy, and we therefore do not report these as distinct vacancy defects in Table 5.2 (since they would dissociate to individual +1 charged vacancies and localized holes).

5.4 Discussion

The results for the calculated vacancy formation energies are summarized graphically in Fig. 5.5, which plots E_{form} versus Fermi energy (E_f). Results are presented for all the neutral vacancy configurations, for each of the four oxygen environments and the three different spin configurations. For the +1 charged oxygen vacancies, the lowest energy configuration for each environment is plotted. For the +2 defect charge state, we plot only the formation energy of the 333 environment, since for the remaining environments the additional hole that carried the positive charge was not bound to the +1 charged vacancy core. The results display visually the variation of E_{form} with local environment, defect charge and spin configuration.

A primary result of the present calculations is the variation of E_{form} with local environment in the low-T monoclinic phase, which should be also relevant for the short-ranged ordered cubic phase at low to intermediate temperatures, as discussed above. These variations in E_{form} are highlighted in Fig. 5.6, which plots results for the lowest-energy defect configuration for each charge state, for each of the four different charge environments. The figure illustrates that all the environments should feature positively charged vacancies for values of the Fermi energy near the VBM. For E_f=0, the lowest values of E_{form} vary with local environment by roughly 0.2 eV. At higher values of E_f the stable charge state, transitions to neutral at charge transition levels that vary with local environment between E_f=0.35 eV to 0.55 eV. Beyond these transition levels, the lowest values of E_{form} again vary across the local environments by approximately 0.2 eV.

These variations in formation energies are particularly interesting in the context of ionic diffusion, where they can produce complex energy landscapes, and lead to an important role of short-range order in influencing the formation of percolating pathways for low energy oxygen hops. In the long range ordered monoclinic phase, we find that all the oxygen vacancy sites with the lowest energy configurations are connected in a percolating cluster and the vacancy would not have to pass through the higher energy configurations as it migrates through the lattice. If migration barriers for hopping are similar, this should lead to percolating diffusion pathways in the cubic phase if the degree of SRO is strong and similar to the long-range order present in the monoclinic phase. However, these percolating pathways could become disrupted as the degree of disorder increases.

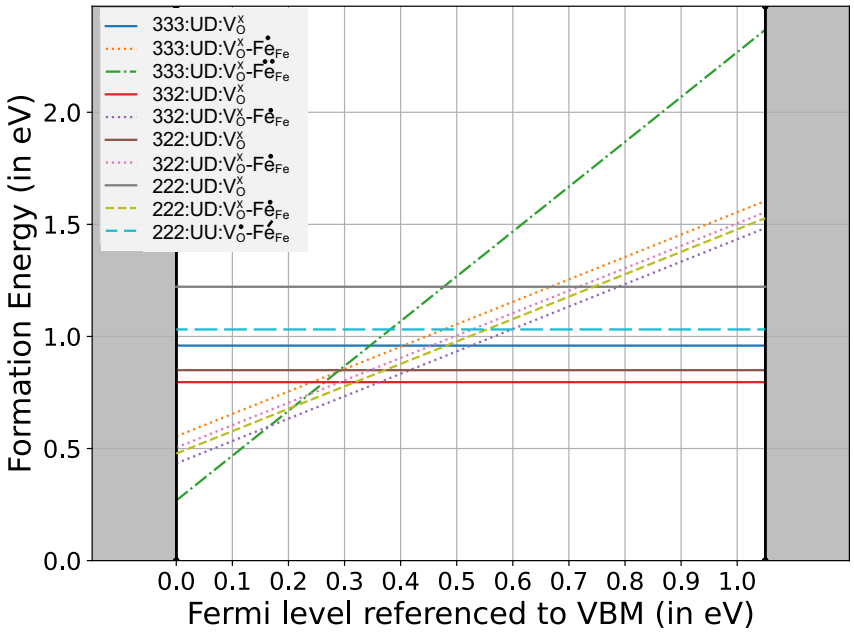


Figure 5.5: Formation energies for oxygen vacancies in the low-T monoclinic phase of magnetite. Results are presented for three charge states, across all the distinct local environments. The legend gives the charge and spin configurations, following the notation described in the text. Results are plotted for the range of Fermi energy spanning the band gap calculated for the bulk monoclinic structure of magnetite.

The calculated results also highlight the importance of the relative timescales of charge transport and spin relaxation times on ion diffusion. In particular, if oxygen ion hops occur on timescales that are fast relative to charge and spin equilibration, the results in Tables 5.1 and 5.2 show that the variation in oxygen vacancy energies could rise significantly. For example, the energy of a neutral vacancy hopping from its equilibrium configuration in a 322 environment would increase by 0.37 eV if it were to hop into a 222 environment with the same spin configuration, compared to 0.17 eV if the spins equilibrated from the UD to the UU configuration. Similarly, hops of the positively charged vacancies could be accompanied by changes in charge state if the hopping of the bound holes is slow, leading to variations in energy by several more tenths of an eV depending on the position of the Fermi level. The situation is even more complex if one considers that the above picture is derived from static calculations, and could be strongly altered by dynamical charge fluctuations.

Overall, these results suggest that models for diffusion in magnetite at low temperatures should account for the variations in local environment and charge and spin configuration on vacancy energetics, and the ways in which cation ordering affect the distribution of neighbor-

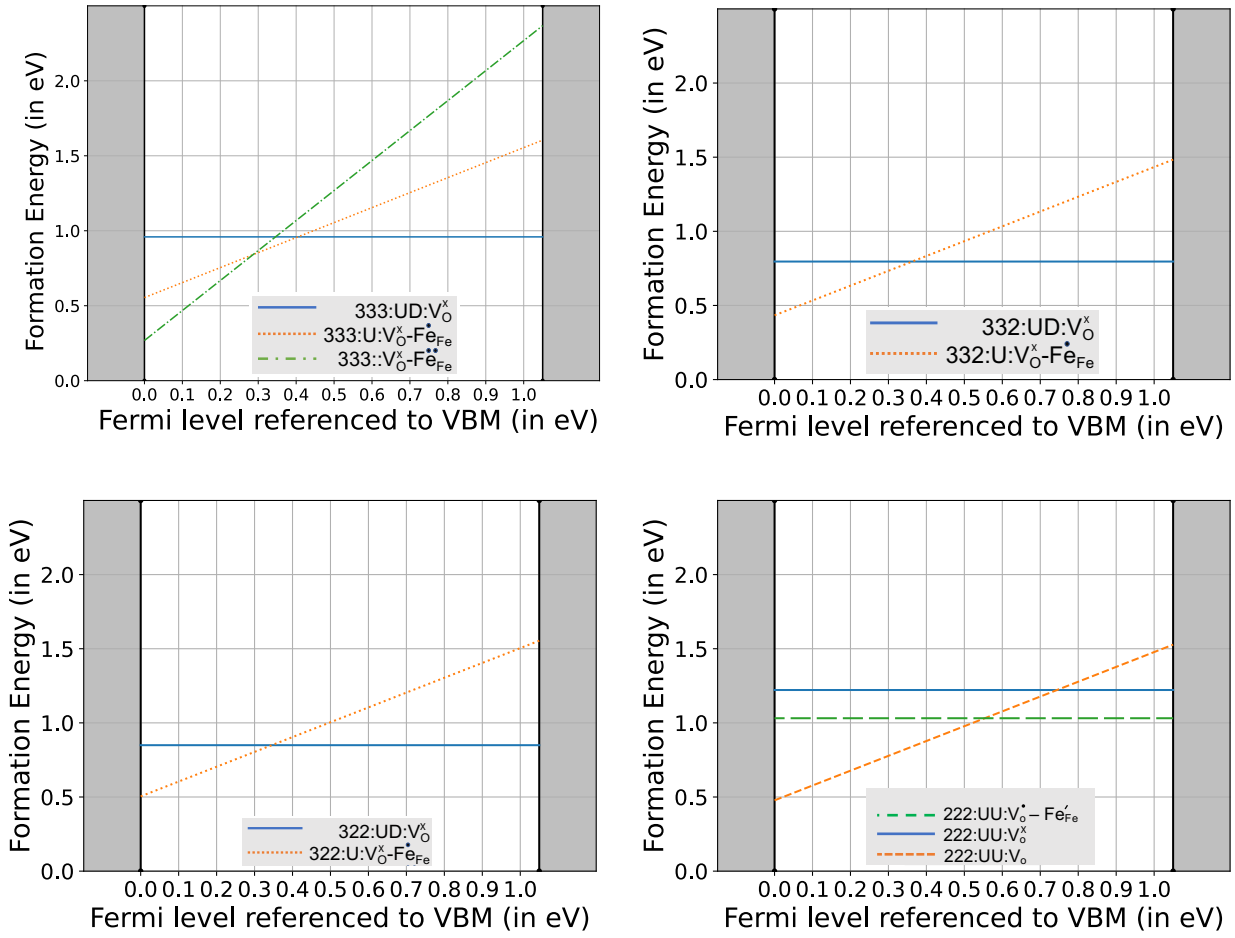


Figure 5.6: Formation energies for oxygen vacancies in the four different local environments, as labeled in the legends.

ing site energetics. This point is consistent with findings of recent studies of ionic diffusion in CeO_2 [144, 145] and spinels such as $FeAl_2O_4$ [146], which have shown that the charge redistribution on nearby cation sites as oxygen ions migrate through the lattice affect the effective migration barriers for vacancy hops. Further, temperature-accelerated dynamics for Mg-based spinels [147] highlight how the distribution of chemical species of different charges dramatically changes the overall migration pathways for defects through the crystal, leading to multiple degenerate pathways and complex landscapes where defects become trapped in local super basins.

Finally, it is worthwhile to compare the current calculated results to available experimental data for oxygen vacancies, as summarized in the Introduction. While we are not aware of published values for measured vacancy formation energies in magnetite, available activation

energies (i.e., the sum of the formation and migration energies) derived from experimental measurements of oxygen diffusion have been published [13, 10, 23], and vary between 0.5 eV to 2.0 eV, depending upon temperature and synthesis conditions. These values are primarily for diffusion at high temperatures, where magnetite exists in a cubic spinel phase in which charge short-range order is likely to be weak. While this complicates a direct comparison with the present calculations, it is reassuring that the calculated vacancy formation energies (for values of E_f near the VBM that would be consistent with the known p-type character of magnetite) are smaller than or comparable in magnitude to the measured high-T activation energies for oxygen diffusion under highly reducing conditions where the vacancy- mediated mechanism is active. Additionally, in the previous experimental analysis[11, 12], the vacancies in magnetite are assumed to be neutral, owing to the Fe^{2+}/Fe^{3+} redox based charge screening. In qualitative agreement with this picture, we observe in our calculations that the formation of neutral vacancies involves reduction of Fe^{3+} near the vacancy site.

5.5 Conclusions

The results presented in this work highlight a significant role of the local arrangement of Fe^{2+} and Fe^{3+} cations in determining stable oxygen-vacancy defect configurations in low-temperature magnetite, and the dependence of their formation energies on charge state and spin configuration. Results have been presented for the the low-temperature monoclinic phase of magnetite, but are argued to be also relevant to the cubic phase over a range of temperatures above the Verwey transition, where short range ordering is expected to lead to a similar distribution of local environments. Key findings include variations in stable defect formation energies by around 0.2 eV for a specific local environment, and $\sim$0.6-1.0 eV due to changes in spin configuration. The results also highlight two different types of stable configurations for neutral vacancies, i.e., those involving localization of the electrons within the vacancy "core" when there is more than one nearest neighbor Fe^{3+} cation, and one involving binding of a localized electron on a more distant Fe^{3+} cation to the core when there is only one Fe^{3+} cation. Further, positively charged vacancies were found to involve the binding of localized holes to the vacancy core. The results suggest important effects of local order on the pathways and rates of ionic hopping in magnetite that should be accounted for in transport models at low and intermediate temperatures, where local charge order is pronounced.

Chapter 6

Defect Complexes in Iron Oxides

In chapter 5, calculated results for oxygen vacancies in magnetite were presented. Oxygen vacancies are a dominant minority defect in oxygen-deficient or reducing conditions, with Fe interstitials being the predominant defects because of their low formation energies[11, 12]. In oxidizing conditions, the dominant defect type changes to iron vacancies. As discussed in chapter 2, oxygen transport under such conditions is hypothesized to be mediated by an iron-oxygen vacancy complex[23].

In this chapter we present calculated results showing that under oxidizing conditions, oxygen-iron di-vacancies have formation energies comparable to iron vacancies, and are strongly bound. We also analyze the possibility of clustering of iron and oxygen vacancies in hematite (Fe_2O_3). The methods used to obtain the calculated results are obtained in section 3.2 and 3.3 in chapter 3 for magnetite and hematite, respectively.

This chapter is organized as follows: We begin with studying the formation energies and charge redistribution around iron vacancies in magnetite (Fe_3O_4) in different environments and charge states. Similar to previous studies[30, 33], the formation energies of neutral iron vacancies in the tetrahedral sublattice are higher than ones on the octahedral sublattice by around 1.13-2.2 eV depending on the local environments. Hence, in the subsequent text, we focus on iron vacancies on octahedral sites for detailed analysis. The following sections then perform similar analysis for iron-oxygen di-vacancies and also calculate the binding energies of these clusters. At the end of this chapter, we provide results and discussion on iron-oxygen di-vacancies in hematite (Fe_2O_3), which is another oxide found as a component of multi-oxide scales that can form upon oxidation of iron.

6.1 Iron vacancies for octahedral sites in magnetite

Similar to our previous work on oxygen vacancies, we describe the charge and spin configuration of the iron vacancy using an extended Kröger-Vink notation. Focussing on vacancies

on the octahedral sublattice, with six octahedrally coordinated Fe ions in the next-nearest-neighbor shell, for conciseness, we modify the notation for Fe vacancies slightly from our previous work on oxygen vacancies

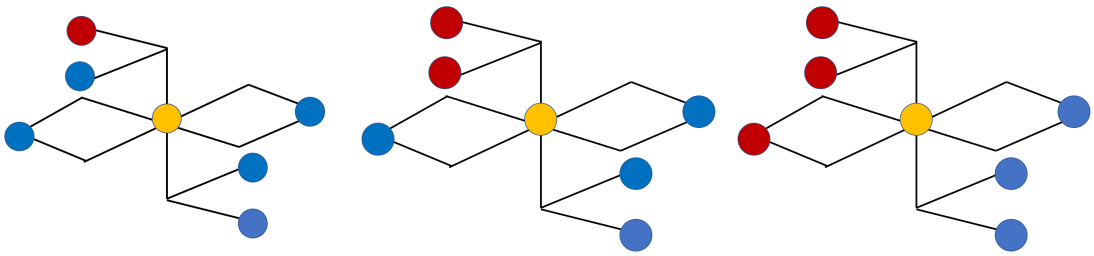
$$ENV : SPIN : CHARGE$$

where the environment (ENV=3_n2_{6-n}, the superscripts denoting the number of Fe ions of the Fe^{3+} or Fe^{2+} type in the local environment) is specified by the charge on the octahedral Fe cations within the core before the vacancy is introduced (see Figure 6.1 and 6.2), the spin configurations ($SPIN$) of the excess electrons/holes are specified as up (U) or down (D), and the charge configuration is indicated using Kröger-Vink notation for the core (V'_{Fe}, V_{Fe} or $V^{\bullet}_{Fe}$) and bound electrons (Fe'_{Fe}) or holes ($Fe^{\bullet}_{Fe}$) on Fe cations that are neighbors to, but outside the core. In this notation, the spin configuration labels for the electrons are made with reference to the magnetic order in the low-T magnetite phase. Magnetite remains ferrimagnetic until about 850 K, and the net moments of Fe ions in the octahedral versus tetrahedral sublattices are oppositely aligned. We define the net spin of the octahedral sublattice as "spin-up" and that of the tetrahedral sublattice as "spin-down". We perform unconstrained spin-polarized DFT calculations for Fe vacancies and denote the spin state of the defect in terms of the spins of localized holes or electrons, present due to the defect.

Local environments for iron vacancies in magnetite

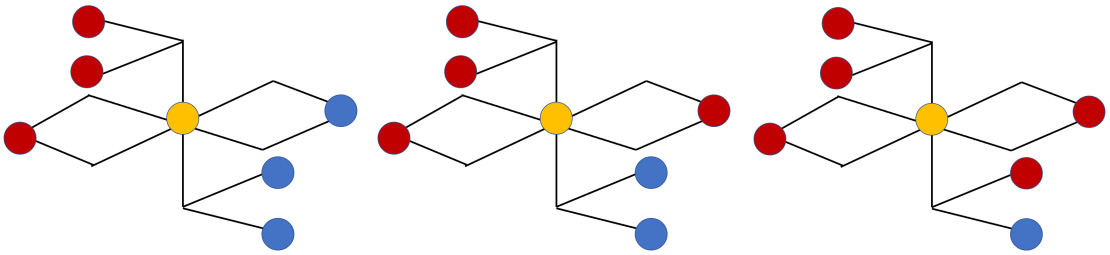
We first describe the formation energies of iron vacancies in the monoclinic charge ordered phase of magnetite. Similar to the case of oxygen vacancies described in the previous chapter, the iron vacancies in the low temperature monoclinic phase can be classified on the basis of the relative number of Fe^{3+} and Fe^{2+} in the next-nearest-neighbor shell, the nearest ions being O^{2-}. The choice of this criterion for classification is motivated by the role of Fe^{3+} and Fe^{2+} as hole and electron localization sites, respectively. Each iron site in this structure has six Fe ions in the neighborhood, each of which can be occupied by either an Fe^{3+} or an Fe^{2+}. In the 224 atom monoclinic cells there are eight different Wyckoff sites for octahedral Fe^{2+} and Fe^{3+} each. Each of these eight sites fall in to one of five categories of local environments found around octahedral Fe sites. Schematics depicting different local chemical environments around the Fe^{2+} and Fe^{3+} sites on the octahedral sublattice are shown in Figure 6.1 and Figure 6.2.

Charge redistribution around iron vacancies can be described in terms of localized holes on the octahedral sublattice. All the octahedrally coordinated Fe^{3+} sites have at least three Fe^{2+} in the first nearest-neighbor shell, so there are three available sites for hole localization close to the vacancy site. In the case of Fe^{2+} sites, as shown in Figure 6.1, the three possible environments are 3_32_3, 3_42_2 and 3_52_1 with three, two and one Fe^{2+} sites in the core, respectively. Therefore for neutral and -1 charge states, the excess holes need to be localized outside the core for some of these environments.



(a) $3_5 2_1$ (b) $3_4 2_2$ (c) $3_3 2_3$

Figure 6.1: Local environments around Fe^{2+} sites on the octahedral sublattice of the monoclinic phase of magnetite. The red, blue and yellow circles denote Fe^{2+}, Fe^{3+} and the octahedrally-coordinated Fe^{2+} vacancy sites, respectively.



(a) $3_3 2_3$ (b) $3_2 2_4$ (c) $3_1 2_5$

Figure 6.2: Local environments around Fe^{3+} sites on the octahedral sublattice of the monoclinic phase of magnetite. The red, blue and yellow circles denote Fe^{2+}, Fe^{3+} and the octahedrally-coordinated Fe^{3+} vacancy sites, respectively.

Formation Energies of Octahedral Iron Vacancies

In the monoclinic structure of magnetite (Fe_3O_4), there are sixteen distinct octahedral iron sites, eight of which are occupied by Fe^{3+} and the other eight occupied by Fe^{2+}. The formation energy values for the different sites with the same charge environments are listed in 6.1 (for Fermi level at the valence band edge) and plotted versus Fermi level in Figure 6.3. As illustrated in the Figure 6.3, the octahedrally coordinated iron vacancies can exist in charge states ranging from -3 to neutral. At Fermi levels close to the valence band maxima, the neutral charge states are preferred. There is no discernible trend in how formation energies vary as a function of local environment. This is likely due to very similar charge localization for all environments for each charge state. Within the environments where multiple Wyckoff positions exist, the range of formation energies for neutral iron vacancies can range from 0.1 to 0.28 eV. The presence of multiple values of formation energies within the same local

Site Occupancy prior to vacancy formation	Iron vacancy configuration	Charge Configuration	$E_{form}(eV)$ for different sites
Fe^{2+}	$3_3 2_3$:DD:0	V_{Fe}^{X}	1.88, 1.96, 1.86
Fe^{2+}	$3_3 2_3$:D:-1	$V_{Fe}^{\prime}$	2.47, 2.52, 2.51
Fe^{2+}	$3_3 2_3$::-2	$V_{Fe}^{\prime\prime}$	3.29, 3.32, 3.27
Fe^{2+}	$3_4 2_2$:DD:0	V_{Fe}^{X}	1.66, 1.9, 1.8, 1.84
Fe^{2+}	$3_4 2_2$:D:-1	$V_{Fe}^{\prime}$	2.24, 2.53, 2.44, 2.5
Fe^{2+}	$3_4 2_2$::-2	$V_{Fe}^{\prime\prime}$	3.08, 3.28, 3.21, 3.22
Fe^{2+}	$3_5 2_1$:DD:0	$V_{Fe}^{\prime} + h^{\bullet}$	1.79
Fe^{2+}	$3_5 2_1$:D:-1	$V_{Fe}^{\prime}$	2.28
Fe^{2+}	$3_5 2_1$::-2	$V_{Fe}^{\prime\prime}$	3.06
Fe^{3+}	$3_1 2_5$:DDD:0	V_{Fe}^{X}	1.94
Fe^{3+}	$3_1 2_5$:DD:-1	$V_{Fe}^{\prime}$	2.59
Fe^{3+}	$3_1 2_5$:D:-2	$V_{Fe}^{\prime\prime}$	3.46
Fe^{3+}	$3_1 2_5$::-3	$V_{Fe}^{\prime\prime\prime}$	4.61
Fe^{3+}	$3_2 2_4$:DDD:0	V_{Fe}^{X}	1.87, 2.0, 1.89, 2.08
Fe^{3+}	$3_2 2_4$:DD:-1	$V_{Fe}^{\prime}$	2.49, 2.6, 2.48, 2.67
Fe^{3+}	$3_2 2_4$:D:-2	$V_{Fe}^{\prime\prime}$	N/A, 3.49, N/A, 3.52
Fe^{3+}	$3_3 2_3$:DDD:0	V_{Fe}^{X}	1.96, 2.15, 1.87
Fe^{3+}	$3_3 2_3$:DD:-1	$V_{Fe}^{\prime}$	2.58, 2.74, 2.48
Fe^{3+}	$3_3 2_3$:D:-2	$V_{Fe}^{\prime\prime}$	3.4, 3.51, 3.32

Table 6.1: Formation energies of iron vacancies with neutral, -1,-2 and -3 charge states calculated for Fermi level at the valence band maxima. The first three columns specify the environment, spin and charge configurations, and the fourth lists the corresponding calculated defect formation energy. The first three rows are the environments around octahedral Fe^{2+} sites, whereas the last three rows denote the local environments around Fe^{3+} sites on octahedral sublattice.

environment can be understood from observing how the charges are localized. For example, for the $3_2 2_4$ environment, there are four different Wyckoff sites, which require redistribution of three holes for the neutral configuration. The formation energies for this environment are 1.87 eV, 1.89 eV, 2.00 eV and 2.08 eV. In the first two environments, all the localized holes are in different octahedral planes, minimizing the repulsion between like-charges, which can potentially explain slightly lower values of formation energies.

Charge redistribution around iron vacancies

Similar to oxygen vacancies described in the previous chapter, formation of iron vacancies is also accompanied by redistribution of charges around the core. Removing a cation

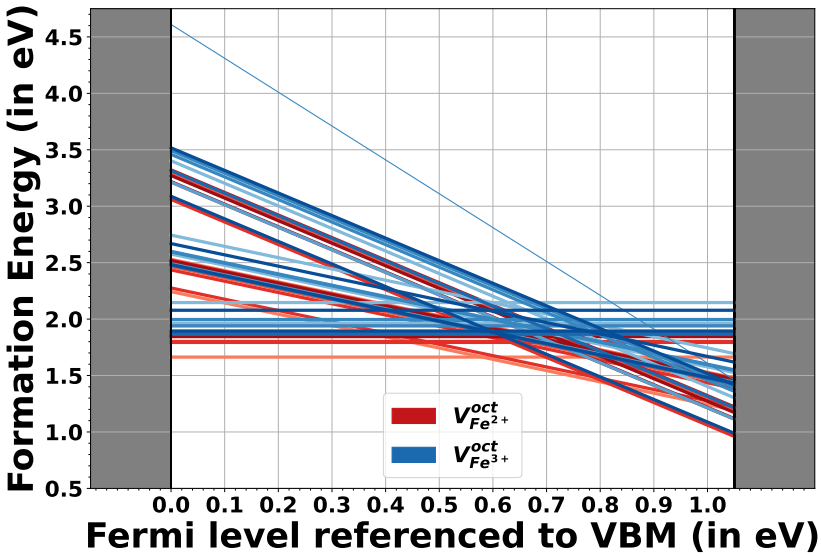


Figure 6.3: Formation energy of iron vacancies in magnetite for sixteen different Wyckoff sites and three charge states: 0, -1, -2 and -3. The red lines depict the vacancies at Fe^{2+} sites and the blue lines represent the vacancies at the Fe^{3+} sites. The -3 charge state is only depicted for $3_5 2_1$ environment, as for the rest is is not stable with respect to decomposition to -2 charged vacancies and an unbound electron polaron.

can result in neutral or negatively charged vacancies. In case of magnetite, Fe exists in the form of Fe^{3+} or Fe^{2+}. Creating a neutral vacancy can require redistributing either +3 or +2 positive charge (in the form of localized holes) around the vacancy site. This is in contrast to the neutral oxygen vacancies, where the neutral vacancy is accompanied by redistributing electrons around the vacancy site. As a result, the charge redistribution in the case of Fe vacancies will require the presence of Fe^{2+} ions as they can act as a site for localizing holes due to the possibility of being oxidized to Fe^{3+}. As described in Figures 6.1 and 6.2, all the Fe^{3+} sites have at least three Fe^{2+} in the next nearest-neighbor shell, whereas the Fe^{2+} ions can have three, two or one Fe^{2+} ions in the nearest-neighbor shell.

We performed charged defect calculations for the charge states ranging from -3 to 0 for all the sixteen Wyckoff positions for octahedrally coordinated Fe^{2+} and Fe^{3+} sites. For each charge state for each configuration, the defect configuration consists of an iron vacancy, localized holes in the next nearest-neighbor shell ("Fe vacancy core") and localized holes outside the core. The Fe vacancy core can be neutral or negatively charged.

The core charges and charges outside the core are described in Tables 6.2 and 6.3. For

the case of neutral Fe^{2+} vacancies, the two holes are localized inside the vacancy core, on two of the six nearest octahedral iron sites. In the case of the $3_5 2_1$ environment, since only one Fe^{2+} site is available, the one hole is localized outside the vacancy core. This hole is bound to the vacancy core with binding energy of around 0.14 eV. For the -1 and -2 charge states, the charge is contained within the vacancy core, which consists of the six nearest-neighbor iron sites, with one and zero holes localized inside the core. Additionally, the configurations with overall -3 charge for vacancies at Fe^{2+} sites, result in a -2 charged core with an excess electron which is not bound to the core.

We consider next the vacancies on Fe^{3+} sites. The neutral and -1 charged vacancies have all the charge contained within the core. For -2 charged configurations, two of the $3_2 2_4$ environments relax to a defect configuration with -2 core charge whereas the other two maintained a -1 charged core with an excess unbound electron outside the core. For -3 charged defects, all but one defect configuration relax to a -2 charged core with an unbound electron, the other one being a -3 charged core. The latter defect configuration is much higher in energy than the rest and the calculated results suggest it will not be found in significant concentration under equilibrium conditions in magnetite for Fermi levels close to valence band maxima(VBM).

6.2 Brief Discussion on iron vacancies in magnetite

Here I discuss briefly how the results presented here for Fe vacancies compare to the current literature and the interpretation of these results. In experimental diffusion studies, the dominant mechanism for diffusion of iron at high oxygen chemical potentials is through the diffusion of iron vacancies[11, 12]. As observed by change in slope of curves of iron tracer diffusion coefficient as a function of partial pressure of oxygen, the cation diffusion mechanism changes from interstitialcy type in reducing conditions to vacancy type in oxidizing condition. Previous computational studies on iron vacancies have either focused on the hopping of iron vacancies in metallic cubic spinel and relative formation energies of tetrahedral and octahedral sites (with no charge ordering on the octahedral sublattice)[30] or considered only neutral charge state of iron vacancies[32, 33]. Across different studies, supercell sizes, charge ordering on octahedral sublattice, +U values and chemical potentials for iron are different, so it is not possible to provide a quantitative comparison. We therefore, restrict ourselves to a qualitative discussion in the following.

In the studies mentioned above, similar to our results, it is found that the iron vacancies at the tetrahedral sites have much higher formation energy than the ones on octahedral sublattice. For iron vacancy calculations in the half metallic inverse spinel structure[29], it is found that the formation of iron vacancies is accompanied by change in net magnetic moment of the supercell due to redistribution of holes. However, as the electronic structure

Environment	Charge state	Core charge	Binding Energy
$3_3 2_3$	0	0	N/A
	-1	-1	N/A
	-2	-2	N/A
	-3	-2	Excess e^- not bound
$3_4 2_2$	0	0	N/A
	-1	-1	N/A
	-2	-2	N/A
	-3	-2	Excess e^- not bound
$3_5 2_1$	0	-1	0.143 eV
	-1	-1	N/A
	-2	-2	N/A
	-3	-2	Excess e^- not bound

Table 6.2: Charge redistribution around Fe^{2+} vacancy sites. The first column lists the environment by denoting the number of 3+ and 2+ Fe neighbors (see main text). The second column gives the charge state of the defect, and the third the charge within the core after relaxing the defect configuration. For cases where the core charge differs from the overall defect charge, the binding energy of the excess electron or hole localized outside the core is given in the fourth column. In only one such case (the neutral vacancy for the $3_5 2_1$ configuration) is the excess localized charge outside the core bound.

of the bulk cell used in those studies is half-metallic, this excess charge is delocalized over all the octahedral sites in the defect supercell. Including correct energetics of vacancy formation which can capture the associated redox of ions is crucial to model not just iron transport but also formation of phases such as maghemite during oxidation of magnetite, which is a result of ordering of iron vacancies on the magnetite cation sublattice. The results above would be useful in interpreting the interplay between vacancy formation and changes in redox state of iron ions in these complex oxide systems.

6.3 Iron-Oxygen di-vacancy in magnetite

We now shift our focus to the iron-oxygen di-vacancy in iron oxides, beginning with magnetite. Using similar methods as the oxygen vacancies, we performed defect calculations for di-vacancies in magnetite. The chemical potentials used to calculate formation energies for iron vacancies and iron-oxygen divacancies however correspond to conditions, characterized by maintaining an equilibrium between magnetite (Fe_3O_4) and hematite (Fe_2O_3). The computational details are given in section 3.2 in chapter 3. In previous experimental diffusion studies, the clustering of oxygen vacancies with iron vacancies is hypothesized as the defects

Environment	Charge state	core charge	Binding Energy
$3_3 2_3$	0	0	N/A
	-1	-1	N/A
	-2	-2	N/A
	-3	-2	Excess e^- not bound
$3_2 2_4$	0	0	N/A
	-1	-1	N/A
	-2	-2	N/A
		-1	Excess e^- not bound
	-3	-2	Excess e^- not bound
$3_1 2_5$	0	0	N/A
	-1	-1	N/A
	-2	-2	N/A
	-3	-2	Excess e^- not bound
	-3	-3	N/A

Table 6.3: Charge redistribution around Fe^{3+} vacancy sites. The first column lists the environment by denoting the number of 3+ and 2+ Fe neighbors (see main text). The second column gives the charge state of the defect, and the third the charge within the core after relaxing the defect configuration. For cases where the core charge differs from the overall defect charge, the binding energy of the excess electron or hole localized outside the core is given in the fourth column. Note that the excess electrons outside the core for the -3 charge states of the vacancy are not bound to the core.

responsible for oxygen transport under oxygen rich conditions[23]. Considering this, we calculate iron-oxygen di-vacancy configurations for each of the four environments described in chapter 5.

Local chemical environments for iron-oxygen di-vacancies in magnetite (Fe_3O_4)

For each of the four oxygen environments described in chapter 5, we create four different di-vacancies, depending on which iron site in the vacancy core is part of the oxygen vacancy-iron vacancy complex. Three of these iron-oxygen divacancies involve the iron vacancy in the octahedral sublattice whereas the other involves the iron ions in the tetrahedral sites. The different possible configurations are schematically depicted in Figure 6.4. The "di-vacancy core" is defined as the iron and oxygen vacancy sites plus all the nearest iron neighbors for the oxygen and iron site involved in the di-vacancy.

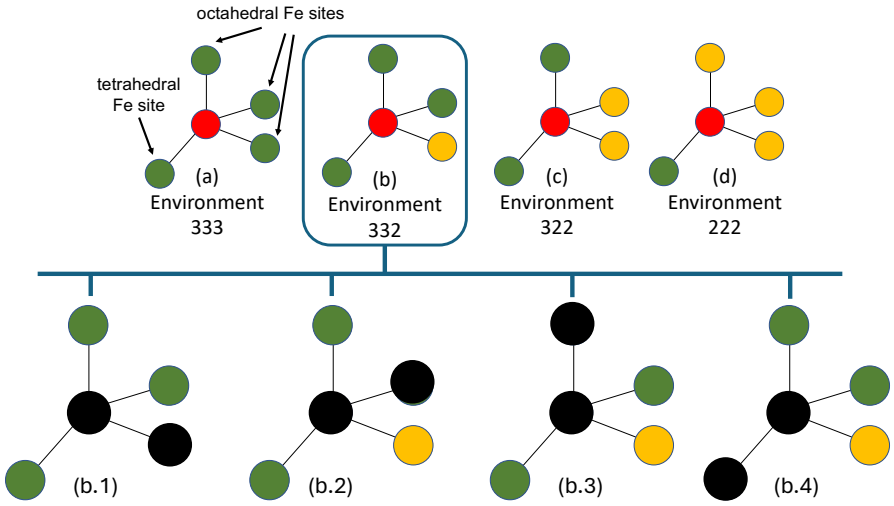


Figure 6.4: Different configurations for iron oxygen di-vacancies in magnetite. The top row shows the four environments of an oxygen site, following the representation introduced in Figure 5.1. For the 332 environment, four distinct Fe-O di-vacancy configurations are illustrated by the black spheres, along with numbers (1-4) corresponding to each.

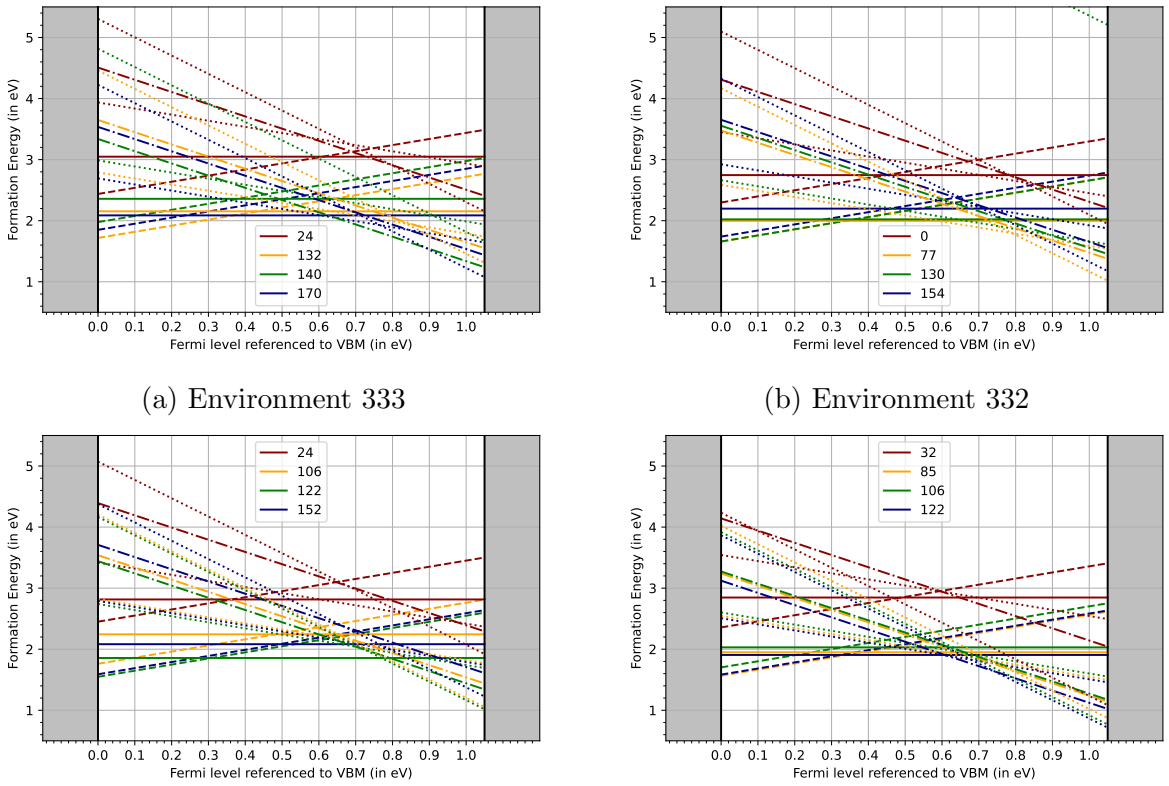
Formation Energies of Fe-O di-vacancies

For a particular oxygen vacancy site, the formation energy of the di-vacancy depends on which Fe vacancy site in the core is bound to the oxygen vacancy. The calculated formation energies for each of the four iron sites as given in Table 6.4 for the Fermi level at the valence band edge. Results are plotted as a function of Fermi level for each oxygen position in Figure 6.5. As can be seen for all the four oxygen sites, the di-vacancy which involves creating a vacancy at the tetrahedral Fe site has higher formation energy than the one involving the octahedral Fe site for the same oxygen vacancy site.

Next, we decompose the formation energy of divacancies in terms of charge states to see if there are any preferred environments for a specific charge state. As can be seen in Figure 6.6, the most stable oxygen vacancy sites for a particular charge state changes from 223 to 222 as the overall charge of the di-vacancy becomes more negative.

Charge redistribution around iron Oxygen divacancies

Similar to oxygen and iron vacancies, we can analyze the charge redistribution around the di-vacancy by identifying sites of localized holes and electrons and their position relative to the di-vacancy site. Depending on the charge state of the iron vacancy site in the di-vacancy, the amount of charge that needs to be redistributed around the di-vacancy might change. For instance, creating a neutral di-vacancy for an O^{2-} - Fe^{2+} pair does not require creating



(a) Environment 333

(b) Environment 332

(c) Environment 322

(d) Environment 222

Figure 6.5: Formation energies for different charge states of iron-oxygen di-vacancies formed at the four different oxygen sites in magnetite. The legends in each plot denote the index of iron vacancies around the oxygen vacancy in the 448 atom monoclinic supercell. The indices between 0-63 denote tetrahedral Fe^{3+} sites. The indices 64-127 and 128-192 denote octahedral iron sites occupied with Fe^{2+} and Fe^{3+} ions, respectively.

excess electrons or holes, whereas creating a neutral di-vacancy for an O^{2-} - Fe^{3+} pair will require localizing an excess negative charge in the defect supercell, either by removing a hole with respect to the +1 charged configuration or by localizing an electron on a neighboring Fe^{3+} site. This Fe^{3+} site can be either inside or outside the "di-vacancy core" (explained below), and can be bound or unbound to the "di-vacancy core". The analysis of charge redistribution around various di-vacancy sites and the binding energy of charges outside the core is provided in the following section.

Core and bound charges in the Fe-O divacancies

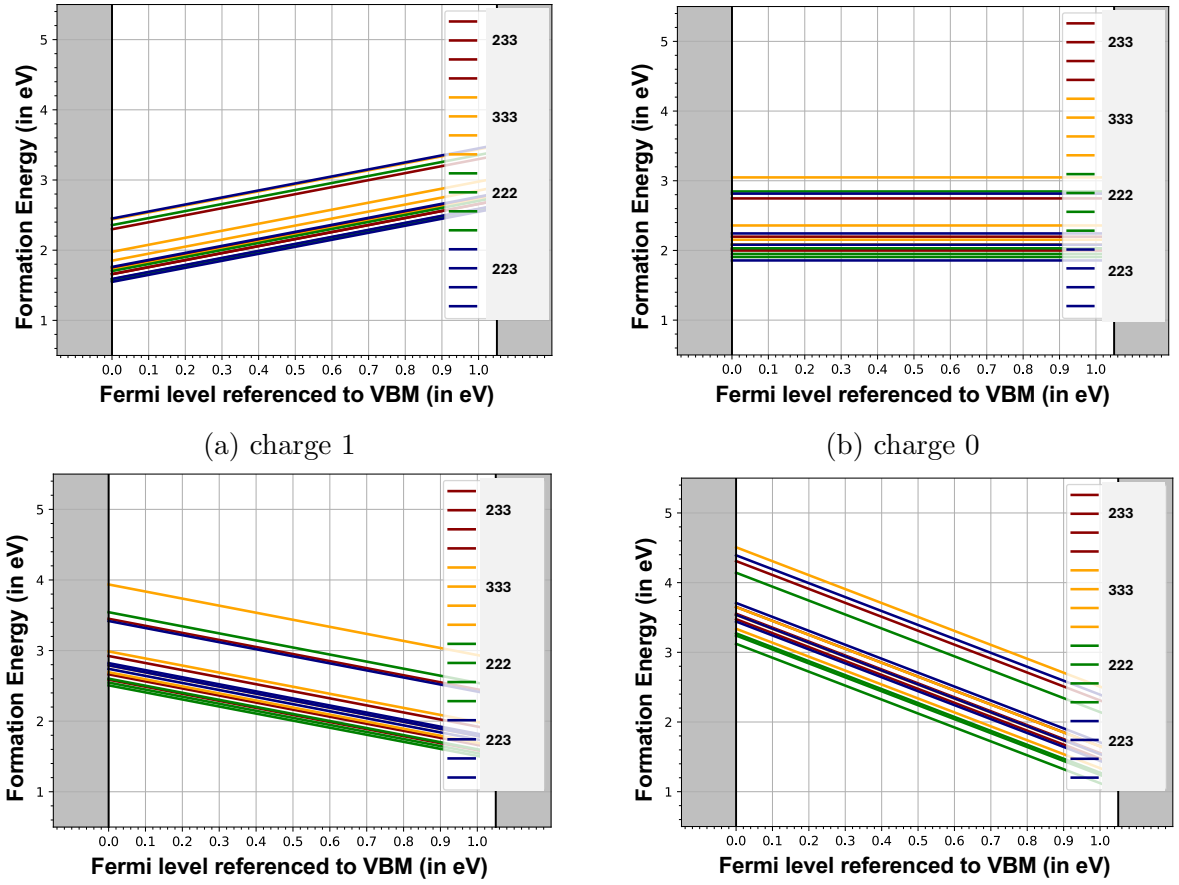
The "di-vacancy core" is defined as the iron and oxygen vacancy sites plus all the nearest iron neighbors for the oxygen and iron site involved in the di-vacancy. Depending on the

Oxygen vacancy environment	iron site valence	$E_{form}(eV)[neutral]$	$E_{form}(eV)[+1]$
333	+3	2.15	1.72
	+3	2.36	1.98
	+3	2.09	1.85
	+3 (tet)	2.75	2.44
332	+3	2.02	1.66
	+3	2.19	1.74
	+2	2.00	1.66
	+3 (tet)	3.05	2.30
322	+3	2.08	1.59
	+2	2.24	1.76
	+2	1.86	1.55
	+3 (tet)	2.82	2.45
222	+3	1.91	1.58
	+2	1.95	1.57
	+2	2.03	1.70
	+3 (tet)	2.85	2.36

Table 6.4: Formation energies of neutral and +1 charged iron-oxygen divacancies. The first two columns specify the oxygen environment and charge configurations of the Fe cation site, respectively. The third and fourth columns lists the corresponding calculated defect formation energy for the neutral and +1 charged di-vacancy configurations, with the value of the Fermi energy corresponding to the valence band edge.

overall charge state and the oxygen vacancy site local environment, the charge redistribution can involve either only the iron sites in the "di-vacancy core" or the iron ions outside it. We describe the core charges for different di-vacancy sites in Figure 6.7 and then discuss the binding energy of localized holes and electrons for the cases where the excess charge, defined as the difference in the defect charge state and core charge, is non-zero.

As can be seen in Figure 6.7, the core charges of distinct di-vacancy sites vary differently with overall charge state of the defect. The excess charges outside the core can be bound or unbound to the core. For the case where the charge outside the core is an electron, the binding energy to the core is calculated by taking a difference between the defect formation energy with the sum of formation energy of the defect with a single electron localized on the lowest-energy Fe^{3+} site, and the formation of the di-vacancy at same oxygen-iron vacancy site but a higher charge state with the same core charge. Similarly, for the defect configurations with excess holes localized outside the core, the binding energy of the out-of-core hole is calculated by taking a difference of defect formation energy with the sum of formation energy of the hole localized on the most stable Fe^{2+} site, and the di-vacancy with the same



(a) charge 1

(b) charge 0

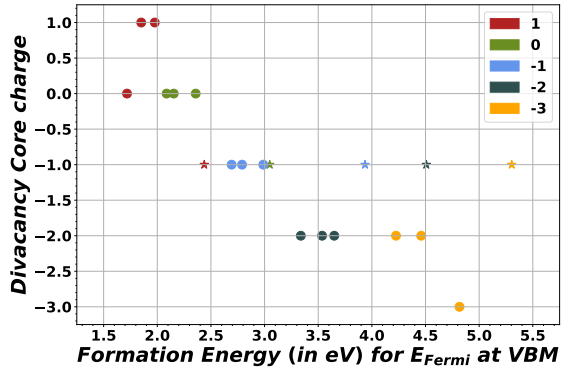
(c) charge -1

(d) charge -2

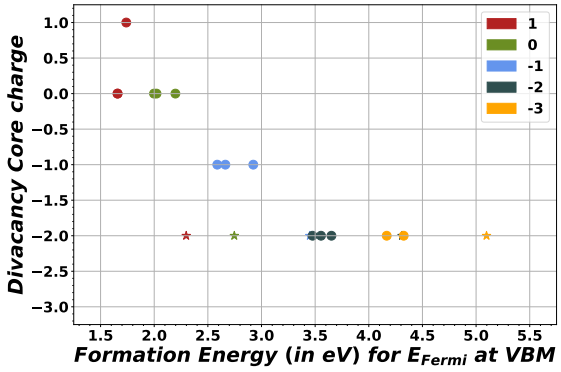
Figure 6.6: Formation energies of iron-oxygen di-vacancies formed at the four different oxygen sites in magnetite for charge states +1, 0, -1 and -2. The colors for the lines correspond to different environments for the oxygen and iron vacancies as described in the text and legend. The -3 charged di-vacancies are not stable except for a single configuration as described in the text.

oxygen-iron vacancy sites but a lower charge state with the same core charge.

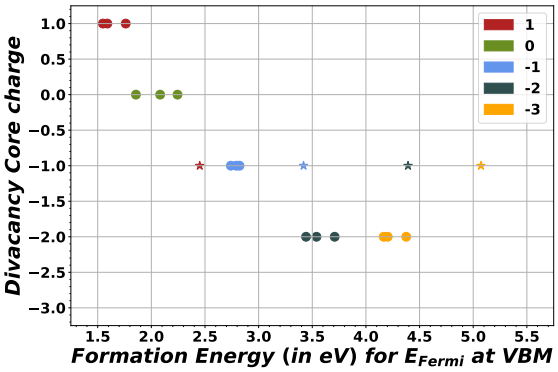
We focus initially on divacancies where the iron vacancy exists on the octahedral sublattice. For all cases but one, a -3 charged di-vacancy has either a -2 or -1 charged core. In all the cases where the core charge is -2 for -3 charged defect configuration, the excess electron(localized on a previous Fe^{3+} site) is not bound to the core. In our model of magnetite, this will effectively mean that the -3 charge state for di-vacancy is not stable at these sites and will always decompose into a -2 charged di-vacancy (if stable) and excess electron polaron. This holds true in our magnetite calculations, irrespective of whether the octahedral



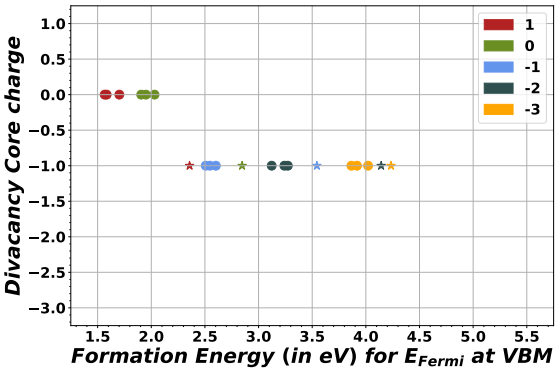
(a) Environment 333



(b) Environment 332



(c) Environment 322



(d) Environment 222

Figure 6.7: Core charges and Formation Energy for different defect charge states for each of the di-vacancy local environments, classified based on the oxygen site involved in the di-vacancy. The points denoted by "o" and "*" denote the divacancies with iron vacancy on octahedral and tetrahedral sublattices, respectively. The formation energy for charged defects is calculated for the Fermi energy at the valence band maximum (VBM). The colors of the symbols correspond to the defect charge stage, as given in the legend.

iron site involved in the di-vacancy is Fe^{2+} or Fe^{3+} in the bulk.

The divacancies with 222 oxygen environment, exhibit a different trend, where all the negatively charged defect states have a -1 charged core. The -1 charged di-vacancy consist of the Fe and O ion removed plus an electron localized on the tetrahedral site closest to the oxygen vacancy site. This core charge distribution is maintained and the -2 and -3 di-vacancy configurations consist of one and two excess electrons localized on Fe^{3+} sites, respectively. In both of these cases, either the excess electrons outside the core are unbound or have very

small binding energy ($\sim$ 5 meV). As can be seen from the plots in Figure 6.7, all the neutral and -1 charged divacancies have the charge located inside the "di-vacancy core". In the case of +1 charged di-vacancy core, both +1 charged and neutral cores are stable. Depending upon the local environment around the oxygen vacancy sites, for all cases of +1 charged di-vacancy with neutral core:

- 222 environment: Excess hole is either very weakly bound to the core ($\sim$ 40 meV) or unbound
- 333 environment: Excess hole is more strongly bound by $\sim$100 meV.
- 233 environment: Excess hole is more strongly bound by $\sim$120 meV.
- 223 environment: All the cores are +1 charged. No excess holes.

Interestingly, for all the four classes of divacancies, different defect configurations maintain their core charge across different charge states. The 332 environment is stable with -2 core charge, whereas the rest of the environments prefer to maintain a -1 charged core.

Binding Energies of di-vacancies in magnetite

In the presence of any external doping or externally biased Fermi level, magnetite is known to exist as a p-type semiconductor. Here, we will restrict ourselves to Fermi levels close the valence band maximum (VBM) while discussing binding energies of the di-vacancies. Assuming Fermi level is within 0.3 eV from the VBM, as described in chapter 5, all the oxygen vacancy sites except the ones in the 333 environment are most stable in the +1 state. For the oxygen vacancy in the 333 environment, the +2 charge state is most stable. In this range of Fermi level, all the iron vacancies are neutral. Considering only the most stable charge states for Fermi level at the valence band maximum, we can calculate the binding energy of iron-oxygen di-vacancies using the defect reaction:

$$V^{\bullet}_{\text{Fe–O}} \longrightarrow V^{\text{X}}_{\text{Fe}} + V^{\bullet}_{\text{O}} \tag{6.1}$$

for all oxygen sites except 333, where

$$V^{\bullet}_{\text{Fe–O}} \longrightarrow V^{\text{X}}_{\text{Fe}} + V^{\bullet\bullet}_{\text{O}} + e^{-} \tag{6.2}$$

As can be seen from the binding energy values listed in Table 6.5, the iron and oxygen divacancies in magnetite are strongly bound. Moreover, the formation energies of these divacancies are smaller than the iron vacancies under oxidizing conditions. This provides support to the previous hypothesis of iron-oxygen divacancies playing an important role in oxygen transport in magnetite under oxidizing conditions.[23].

Environment	Iron site charge	$E_{binding}(eV)$
333	+3	0.22
	+3	0.44
	+3	0.28
332	+3	0.43
	+3	0.77
	+2	0.67
322	+3	0.99
	+2	0.54
	+2	0.82
222	+2	0.8
	+2	0.58
	+2	0.76

Table 6.5: Binding energies of +1 charged iron-oxygen divacancies for the Fermi level at the valence band maxima. The first two columns specify the oxygen environment and charge state of the Fe site before the vacancy is introduced. The third column lists the corresponding calculated di-vacancy binding energy as described in the text.

Brief discussion of results on iron-oxygen di-vacancies in magnetite

Di-vacancies consisting of cation and anion vacancies, bound to each other have been hypothesized in several experimental[148, 149, 36] and theoretical studies[38, 37], but are relatively less studied computationally. Specifically, in the case of magnetite, the presence of cation-anion di-vacancies [23] has been speculated. At higher oxygen partial pressures, where the formation of oxygen vacancies is less favorable, iron-oxygen divacancies have been hypothesized as the dominant defect contributing to oxygen transport in magnetite. The presence of these divacancies is also mentioned in other iron based spinels in the context of the influence of oxygen vacancies on cation transport [37]. Though point defects such as vacancies and interstitials are usually considered as playing the dominant role in mass transport, the formation of defect complexes can be an important factor in determining the overall transport rates and mechanisms. Specially under irradiation, formation of defect complexes is not uncommon and has been extensively studied in some materials with applications in extreme environments[150, 35, 34]. The early fast neutron irradiation experiments on MgO, Al_2O_3 and $MgAl_2O_4$ demonstrated that the spinel system ($MgAl_2O_4$) exhibits a much lower swelling under irradiation, and motivated further experimental and computational studies to understand the role of chemistry and cation ordering on radiation tolerance of these systems[34, 147]. Under extreme environment conditions such as irradiation, initially point defects are formed in non-equilibrium conditions which then equilibrate to thermodynamic

concentrations with processes of diffusion and annihilation by other point and planar defects as well as inducing disorder on cation sublattices[34].

Based on the results in previous sections of this chapter, we can conclude that there is a strong energetic driving force for oxygen and iron vacancies to form clusters. For Fermi energies close to the VBM, the formation energies of divacancies, stable in the +1 charge state, are comparable to the neutral iron vacancies. For all the considered environments, the divacancies involving iron vacancies in the tetrahedral site are higher in energy than those with the iron vacancy on the octahedral sublattice. Moreover, the range of formation energies of divacancies with iron vacancy at the octahedral site vary from 0.08 eV to 0.38 eV within the same environment.

In previous work done on diffusion of cation-anion di-vacancy in $MgAl_2O_4$[37], it was found that rotation is required for these di-vacancies to diffuse in the spinel lattice. Assuming similar barriers, this will make di-vacancy reorientation at some sites much more likely than others, and the relative stability of different orientations of di-vacancies can play an important role in determining the principal diffusion pathways. The same study also found that the di-vacancies involving vacancies in the tetrahedral site are kinetically unstable and relaxed to the configuration with cation vacancies on the octahedral sublattice. For both of these defects, the mobility of di-vacancies is highly reduced compared to the mobility of the mono-vacancies. If the same trend persists for magnetite, the formation of di-vacancies can play a crucial role in understanding the transport processes when this material is irradiated. The study on $MgAl_2O_4$ was performed using empirical potentials and employed Temperature Accelarated Dynamics (TAD) based methods to simulate long time scales. This was shown to be crucial for modelling diffusion of di-vacancies as the lowest energy di-vacancies need to escape a superbasin of states to achieve a net migration. For magnetite, we are limited by the unavailability of empirical or machine learned force-fields which can capture the complex interactions and redox associated with formation and transport of point defects. Considering the technological importance of iron oxides and understanding the point defect properties in these systems, we briefly discuss the importance and possible future directions to model transport properties of defects in iron oxides in chapter 8.

6.4 Iron Oxygen di-vacancy in Fe_2O_3 (Hematite)

We end the discussion on defect complexes by briefly looking at a different iron oxide: Fe_2O_3 (hematite). Additional calculations of cation-anion divacancies in this system were performed to support a better understanding of point defects formed when oxidized iron films are irradiated, since both magnetite and hematite can be a part of the multiphase scale when iron is oxidized[151]. Unlike magnetite, hematite contains Fe cations only in the 3+ oxidation state. Therefore, undoped hematite tends to be n-type at finite temperature, due to the presence of stable electron polarons formed by reduction of Fe^{3+} ions to Fe^{2+}[152].

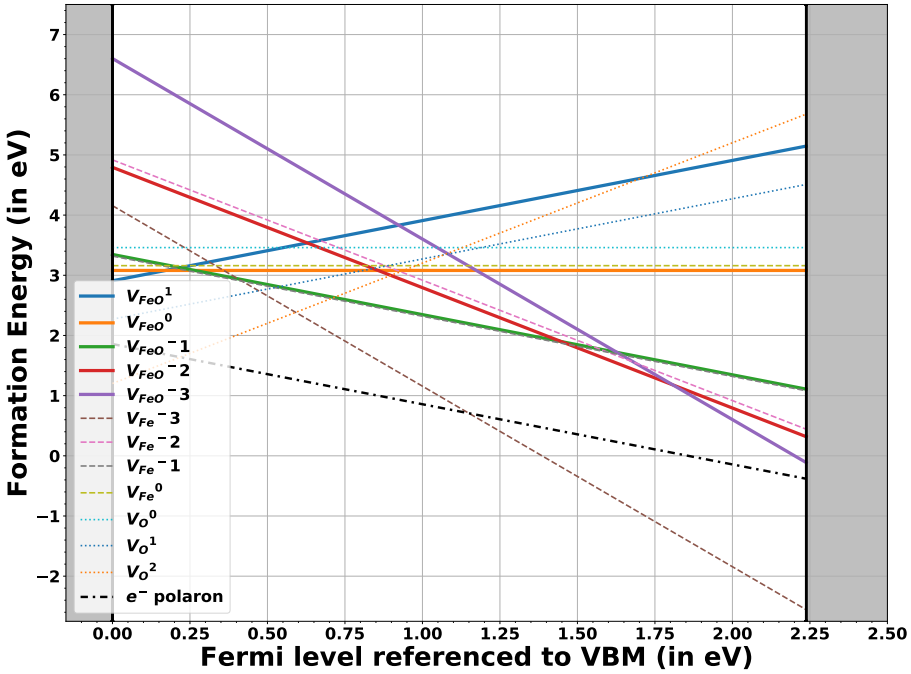


Figure 6.8: The formation energies of iron-oxygen divacancies, iron vacancies and oxygen vacancies in Fe_2O_3(hematite). The solid lines, dashed lines and the dotted lines denote the formation energies of the di-vacancy, iron vacancy and the oxygen vacancy, respectively.

A significant volume of work has been done on understanding point defects such as vacancies and interstitials in hematite. Here, we build on such previous calculations by examining the divacancies and their binding energy. More specifically, the results presented here are an extension of the work performed at LANL[153, 111]. The computational details are the same as described in reference[111], including all the DFT parameters, supercell sizes and the convergence criterion. Additionally, we have used the same values for chemical potential for oxygen and iron. We compare the formation energies of the di-vacancy with iron and oxygen vacancies and calculate the binding energy with respect to the decomposition into iron and oxygen vacancies as well as free electrons. The formation energies of different charge states of the di-vacancy as well as the iron and oxygen vacancies are shown in Figure 6.8.

As can be seen in Figure 6.8, the dominant defect for Fermi levels above the mid-gap (n-type) region is the -3 charged iron vacancies. For Fermi levels higher than 0.75 eV above the valence band maxima (VBM), the second most stable vacancy is the iron-oxygen di-vacancy, with the most stable vacancy being the -3 charged iron vacancy. The formation energies of all oxygen vacancies are higher for these values of the Fermi level. The most stable charge

state of the di-vacancy changes from +1 to -3 across the bandgap. For the Fermi levels above mid-gap, the divacancies can form in multiple charge states, transitioning from -1 to -3. The binding energy of the divacancies along with the associated defect reaction are shown in the Table 6.6.

Charge State	Defect Reaction	$E_{binding}(eV)$
-1	$V'_{Fe-O} + 2e^- \longrightarrow V'''_{Fe} + V^X_O$	0.56
-2	$V''_{Fe-O} + 1e^- \longrightarrow V'''_{Fe} + V^X_O$	0.97
-3	$V'''_{Fe-O} \longrightarrow V'''_{Fe} + V^X_O$	1.01

Table 6.6: Binding energies of iron-oxygen divacancies for Fermi levels above the mid-gap. The first two columns specify the di-vacancy charge state and the respective defect reaction, where V'''_{Fe} and V^X_O are the most stable configurations for the iron and oxygen vacancies used to calculate the binding energy. The third column shows the binding energy for the reaction in column two.

The results in Table 6.6 indicate a significant energetic driving force for the oxygen vacancies to bind to the iron vacancies in hematite. Iron vacancies still remain the dominant vacancy type defect for Fermi levels above the midgap, as their formation energy is lower than that of the di-vacancy (around 2.44 eV for Fermi levels close to the conduction band minima (CBM)). In extreme environments, such as when the oxide is being irradiated, initially a non-equilibrium concentration of iron and oxygen vacancies can exist. The stability of the iron-oxygen di-vacancy can subsequently influence how irradiated hematite relaxes back to the state with equilibrium defect concentrations. It is likely that the migration barriers and diffusion pathways for divacancies in hematite are significantly different from the iron vacancies, and therefore if iron-oxygen divacancies are less mobile (like the case for $MgAl_2O_4$ spinels[37]), the formation of iron-oxygen divacancies can also slow down the iron vacancy diffusion driven relaxation mechanisms after irradiation.

We also note, that including the thermodynamics of electron polarons is important for modelling di-vacancy binding energy, at least in the low temperature regimes where the number of free carriers is limited. The band-gap of hematite is about 2.2 eV[154]. Therefore, for temperatures below 600C[154], hematite shows polaronic conduction. At these temperatures, electron polarons are known to exist and mediate charge transport in hematite[155, 152]. When calculating the binding energy of the di-vacancies with respect to decomposition into iron and oxygen vacancies, if the electronic charge is involved in the defect reaction, the value of binding energy depends on whether the negative charge is going to a band-like state or a localized polaronic state. For instance, for the defect reaction $V'_{Fe-O} + 2e^- \longrightarrow V'''_{Fe} + V^X_O$, the binding energy of di-vacancies is 0.56 eV when the formation energy of e^- corresponds to electron polaron and around 4.27eV when the e^- corresponds to the charge exchanged

with the electron reference potential (VBM in our convention). This enormous difference comes from the localization energy of the electron polaron. At temperatures below 400C where the free charge carrier concentration is low, the former should provide a better estimate of binding energies of di-vacancies. Correctly capturing binding energies is essential for reaction-diffusion based modelling[156, 39], often used to simulate the irradiation effect at the mesoscale. Recent experimental studies have explored the effect of irradiation on iron oxide films[151, 39], and we hope that these results would motivate a critical assessment of the role of iron-oxygen vacancy complexes in studying complex phenomenons such as the effect of irradiation on oxide film growth and transport through these films.

Chapter 7

Density Functional Theory study of structure and optical properties of the elpasolite scintillator Tl_2LiYCl_6

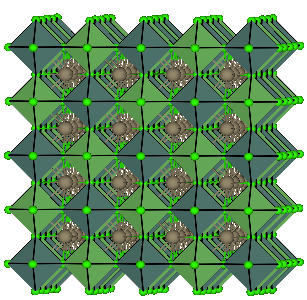
In this work, the primary objective is to understand the nature of bound exciton responsible for observed emission in Tl_2LiYCl_6 (TLYC), a promising scintillator material[64]. We study different structural phases and associated local distortions of Tl-Cl environments in this material with the objective of understanding different bound excitons stable in bulk TLYC. This chapter is organized as follows: We begin by performing harmonic phonon analysis of the cubic elpasolite phase of three materials systems from the elpasolite crystal system: Cs_2LiYCl_6, Rb_2LiYCl_6 and Tl_2LiYCl_6. We provide rationalization for differences in phonon dispersion curves and unstable phonon modes found in the later two. For this purpose, we isolate the ion size from the Tl $6s^2$ chemistry by comparing Rb_2LiYCl_6 and Tl_2LiYCl_6 (where Tl+ and Rb+ have very similar ionic radii), attributing the presence of certain phonon modes to the presence of Tl^+ ions. We then systematically explore lower symmetry phases and polymorphic representation[67] of cubic elpasolite phase of Tl_2LiYCl_6, comparing local environments and Tl-Cl bonding. Finally, we systematically analyze the coupling between structural and electronic properties in Tl_2LiYCl_6 by comparing the bulk electronic structure and local Tl-Cl orbital overlap in different phases of Tl_2LiYCl_6 to highlight the role of distortions.This analysis shows that the bulk electronic density of states exhibit different contributions from Tl^+ near the valence band maximum for undistorted ($Fm\bar{3}m$) and distorted cubic structures (see Figure 7.9a and 7.9b) as well as the tetragonal ($P4_2/n$ and $P4_2$) and the triclinic P1 phases in Figures 7.9d, 7.9c and 7.9e. The discussion is concluded by comparing the nature of stable Tl bound excitons found in the room-temperature tetragonal phase of Tl_2LiYCl_6 with the room-temperature cubic elpasolite phase of Cs_2LiYCl_6.

7.1 Structural Analysis of bulk Tl_2LiYCl_6

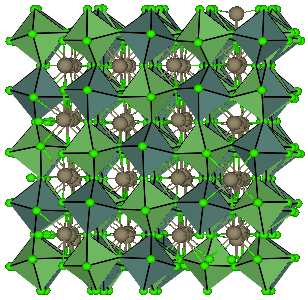
As mentioned in section 2.2, unlike Cs_2LiYCl_6, which shows an exciton emission with a V_K like hole state, the majority of visible light emission from bulk Tl_2LiYCl_6 is hypothesized to originate from Tl^+ ions[64]. In order to study the structural origins of this effect, we first compare the structure of bulk Tl_2LiYCl_6 with its other elpasolite counterparts, Cs_2LiYCl_6 and Rb_2LiYCl_6. Rb_2LiYCl_6 was chosen for this comparison because of similar Shannon ionic radii (1.72 Å) of 12-coordinated Rb^+ and (1.70 Å) of 12-coordinated Tl^+ [157]. The role of relative size of ions in determining the distortions present in the low symmetry phases in perovskites is well-studied in the literature [158, 68, 159]. Previous studies undertaken for elpasolites or other ordered double perovksites [66, 70] have focused on the phase transitions in these systems using a group-theoretical analysis. These studies predict the possible structural distortions and corresponding space groups for second order phase transitions in elpasolites. These possible space groups are calculated taking into account octahedral rotations and specific modes of polar displacement of cations with respect to the high temperature $Fm\bar{3}m$ cubic phase.

The experimentally measured space group for the room temperature tetragonal phase of Tl_2LiYCl_6 is $P4_2$ [65]. To understand the factors stabilizing different distorted structures of Tl_2LiYCl_6, we perform a systematic study of relative energies and local distortions in these structures. We find, from our DFT simulations, that the energy of the tetragonal phase can be lowered by additional distortions. This is further validated by harmonic phonon analysis of the tetragonal structure in $P4_2$ and $P4_2/n$ symmetry, which shows the presence of unstable phonon modes. We also evaluate the polymorphous representation [67] for the cubic elpasolite phase of Tl_2LiYCl_6. It has been suggested in recent literature [67], that these representations can give an approximate picture of the effect of local distortions on electronic structure in high symmetry cubic elpasolite phases that are unstable at zero temperature, considering only the effects of static displacements. For some halide perovskite systems, it has been shown[160] that static distortions and thermal effects in the form of dynamic distortions can have an additive effect on electronic band structure, with both leading to an increase in bandgap due to higher hybridization.

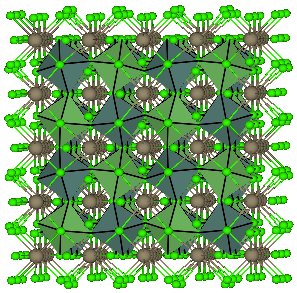
For the purpose of analyzing the effect of local distortions on the nature of bulk exciton states, we utilize the different supercell models for Tl_2LiYCl_6 illustrated in Figure 7.1. These structures include the high-symmetry cubic elpasolite structure shown in Figure 7.1a and several different distorted versions of this structure. These distorted structures include a polymorphous representation of the cubic elpasolite phase[Figure 7.1b], as well as tetragonal structure [Figures 7.1c and 7.1d] and a triclinic structure in Figure 7.1e. These structures are discussed further below.



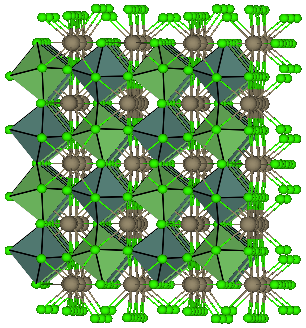
(a) Cubic elpasolite structure Tl_2LiYCl_6



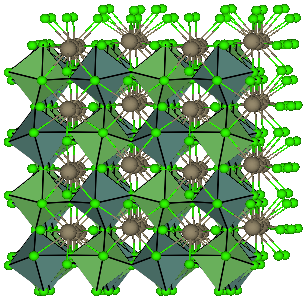
(b) Polymorphous representation of cubic Tl_2LiYCl_6 including static displacements



(c) Tetragonal Tl_2LiYCl_6 with space group $P4_2/n$



(d) Tetragonal Tl_2LiYCl_6- $P4_2$



(e) Triclinic Tl_2LiYCl_6 with space group P1

Figure 7.1: Different structures of Tl_2LiYCl_6 used in this paper to analyze the role of distortions on total energy and bulk electronic structure. The dark green and light green octahedra in these figures correspond to Y-Cl and Li-Cl respectively. The grey spheres correspond to Tl ions. For all the figures, the directions of the lattice vectors are along [100], [010] and [001] directions with these axes aligned with the reference cubic elpasolite phase shown in panel (a).

Comparison of different elpasolite systems

The structure of perovskite-derivative compounds can be characterized into a combination of three categories of distortions from the highest symmetry cubic elpasolite phase: (I) co-operative octahedral rotation, (II) displacement of metal ion at the center of the octahedra, and (III) distortions of octahedra. Whether a combination of these distortion modes lowers the energy relative to the reference cubic structure depends on the ratio of ionic radii of constituent ions and any additional local bonding effects.

Parameters such as Goldschmidt factors [158] are often used to determine whether any

octahedral rotations may lower the energy based on the ion size effects. The Goldschmidt factor (t)[71] for an ordered double perovskite is defined as:

$$t = \sqrt{2}(R_A + R_X)/(R_B + R'_B + 2R_X) \tag{7.1}$$

where R_B and R'_B are the ionic radii of cations at the center of the halide octahedra (Li and Y in our case), R_A is the radius of 12-coordinated cation (here Tl^+) in the undistorted cubic structure and R_X denotes the anion radius (here Cl^-).

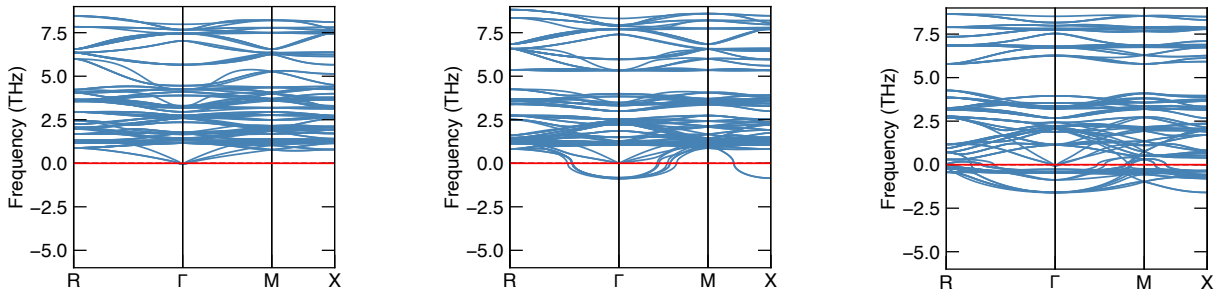
Any deviation of t from the ideal value of one indicates the possibility that octahedral rotations can lower the energy. Tl_2LiYCl_6 has a Goldschmidt tolerance factor of 0.94, suggesting that octahedral rotations are likely to be energetically favorable. In addition to ion size effects, lone pair effects can also result in distortion of anion polyhedra [161, 162, 52]. In the case of Tl_2LiYCl_6, the Tl^+ ion has an electronic configuration of [Xe]$6s^2$ where the electrons in the $6s$ orbital can hybridize with nearby Cl $3p$ orbitals if the local symmetry is broken [163, 59, 58]. This hybridization, if stable, results in further lowering of energy. Based on analyses of the contribution from both Tl-s and Cl-p orbitals at the valence band maximum, we investigate the hypothesis that Tl-Cl orbital overlap contributes to stabilization of distorted Tl_2LiYCl_6 structures [49, 47]. In order to systematically study the role of distortions and their chemical origins, we examine the structures derived from the phonon modes of the high symmetry cubic elpasolite phase, as well as the polymorphic representations. The use of the latter is motivated by previous studies on halide perovskites where a static supercell representation of distortions lowering total energy has been shown to be an improved model of the electronic bandstructure [160, 67], compared to the reference undistorted cubic elpasolite phase.

To distinguish between ion size and hybridization effects, we compare the distortion modes in cubic elpasolite phase of Tl_2LiYCl_6 with those in the same structure for Rb_2LiYCl_6 and Cs_2LiYCl_6. Cs_2LiYCl_6 is expected to be stable in $Fm\bar{3}m$ phase, based on its Goldschmidt factor value of 0.99, and its lack of lone-pair electrons. By contrast, both Rb_2LiYCl_6 and Tl_2LiYCl_6 have Goldschmidt factors of $t = 0.94$, due to the similar values of the Shannon radii for Rb^+ and Tl^+ [164]. Hence, differences in unstable phonon modes and distortions away from the cubic elpasolite phase for these two structures can be attributed to the $6s^2$ electrons in Tl^+ that are absent for Rb^+.

Analysis of Phonon dispersion curves and distortions in the cubic elpasolite phase

Phonon analysis under harmonic approximation is often used to look at possible soft modes which contribute to phase transitions in perovskites from a high symmetry to lower symmetry phase [165]. In some cases, though harmonically unstable at 0 K, the cubic structure might be anharmonically stabilized at high-temperatures, resulting in a phase which

has average cubic symmetry but is dynamically distorted [166, 167]. In both cases, the distortions, dynamic or static, indicate stabilizing effects of local bonding enabled by the local symmetry breaking. The calculated phonon dispersion curves for Tl_2LiYCl_6, Rb_2LiYCl_6 and Cs_2LiYCl_6 are shown in Figure 7.2.



(a) Cs_2LiYCl_6 (b) Rb_2LiYCl_6 (c) Tl_2LiYCl_6

Figure 7.2: Comparison of calculated phonon dispersion curves for cubic elpasolite structures of Cs_2LiYCl_6, Rb_2LiYCl_6 and Tl_2LiYCl_6. The number of unstable modes increase progressively from Cs_2LiYCl_6, to Rb_2LiYCl_6 to Tl_2LiYCl_6 owing to different interaction of Cs^+, Rb^+ and Tl^+ with Cl^- ions

The unstable (imaginary frequency) phonon modes are plotted with negative frequency values in Figure 7.2. As expected from the observed thermodynamic stability of the cubic elpasolite phase of Cs_2LiYCl_6[57] and the Goldschmidt factor close to 1, there are no unstable phonon modes calculated for this compound (see Figure 7.2a). As noted above, Rb_2LiYCl_6 has a Goldschmidt factor of 0.94 similar to Tl_2LiYCl_6, so that it can possibly lower its energy by octahedral rotation. In agreement with this analysis, we find degenerate unstable phonon modes for this compound in Figure 7.2b, that correspond to rotations of the Li-Cl and Y-Cl octahedra. The most unstable phonon modes in Tl_2LiYCl_6, plotted in 7.2b, also correspond to similar octahedral rotations. This indicates that the principal factor causing distortion away from ideal $Fm\bar{3}m$ symmetry is the relatively smaller size of the A site cation for both Tl_2LiYCl_6 and Rb_2LiYCl_6.

Even though the ionic radii are similar, the phonon dispersion curves for Tl_2LiYCl_6 show many more unstable modes in comparison to Rb_2LiYCl_6. Considering the absence of unbonded ns^2 electrons in Rb^+, this is possibly due to additional interactions between Tl-s and Cl-p orbitals in Tl_2LiYCl_6, which are absent in Rb_2LiYCl_6. This is further supported by element-wise decomposition of the phonon density of states, plotted in Figure 7.2c which shows that the unstable modes near zero frequency have a dominant character originating

from the Tl^+ ions.

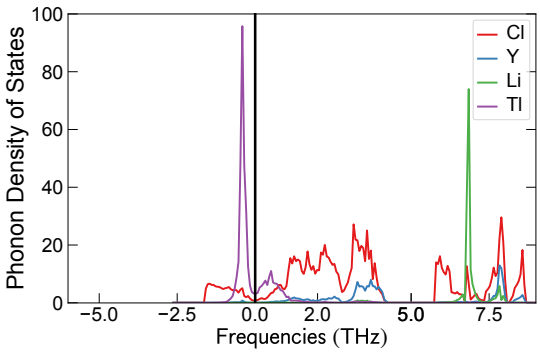


Figure 7.3: Cubic Tl_2LiYCl_6 phonon density of states. Colors are element-wise projections illustrating the contribution from Tl, Cl, Li and Y, and the vertical black line denotes zero frequency. The negative frequencies values correspond to the unstable modes in phonon dispersion curve for cubic Tl_2LiYCl_6.

For Tl_2LiYCl_6, the most unstable modes (i.e, those with the largest magnitude of the imaginary frequencies) characterized by largest displacements for with larger absolute value of negative (imaginary) frequencies are mostly contributed by Cl^-, with octahedral rotation being the most unstable mode. The sharp peak in the phonon density of states (Figure 7.3) in the frequency range -0.5 to 0.0, is derived from modes with dominant contribution from Tl displacements, that appear to be rattle-like in nature. There have been numerous studies on Tl containing compounds displaying rattle modes[168, 169], which originate from the comparatively smaller size of Tl^+ ion, allowing for motion of Tl^+ ion into anion coordination polyhedra. Octahedral rotations also contribute towards reducing the available volume in Tl-Cl polyhedra.

Polymorphous representation of cubic elpasolite phase

As described above, the cubic elpasolite phase of Tl_2LiYCl_6 is harmonically unstable and therefore will dynamically sample multiple Tl-Cl bonding motifs at finite temperature. The resulting distribution of distorted local environments lowers the energy. We will also show in subsequent sections in this chapter that these distortions enable localization of excitons on Tl sites.

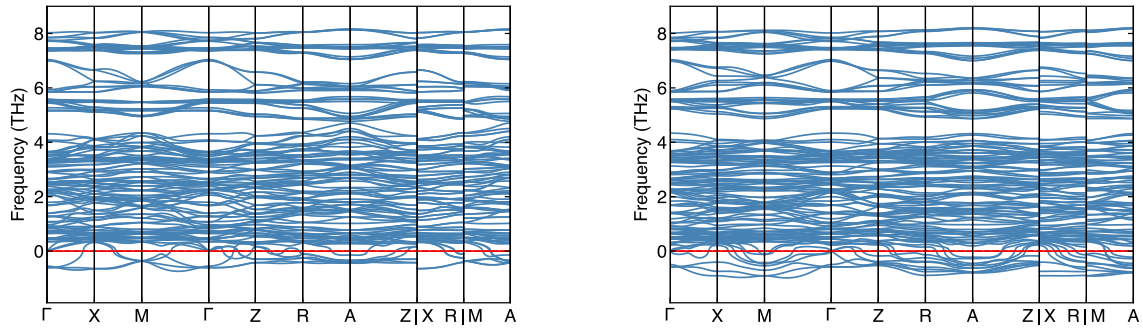
To account for these distortions in the modeling of the finite-temperature cubic elpasolite phase, we created supercells representing polymorphous representations of the cubic elpasolite phase by creating a 320 atom supercell and relaxing the internal coordinates of all ions, keeping the supercell shape and size fixed, after an initial random perturbations of the ions

by 0.15 Å. The energy of the resulting structures is lower than the high symmetry cubic elpasolite phase but higher than the triclinic ground state. The energy lowering distortions enable the Tl-Cl bonding environments observed also in the ground state phase. This is discussed in more detail in subsection 7.1. Moreover, different randomly initialized structures relax to different local minima, but differing in energy by less than 10 meV per formula unit.

Structural distortions and stability in the tetragonal phase

In this section, we present harmonic phonon analysis and a discussion of the role of different distortion modes in the tetragonal phase of Tl_2LiYCl_6. Neutron diffraction characterization by Onken et. al[65] demonstrates that Tl_2LiYCl_6 undergoes a phase transition from the cubic elpasolite phase to a tetragonal structure as the temperature is lowered below 464 K. This experimental study[65] concluded that this tetragonal structure has $P4_2$ symmetry, but it was also noted that it is challenging to extract the exact Wyckoff positions from fits to the neutron scattering data, leading to uncertainties in the exact space group.[65]. Previous theoretical work considering structural phase transitions in ordered double perovskites lists the possible space group symmetries during the phase transition from cubic to lower symmetries resulting from octahedral rotations[66]. The octahedral rotation mode experimentally observed in the tetragonal phase of Tl_2LiYCl_6 using neutron diffraction is $a^-a^-c^+$ in Glazer notation[170]. This corresponds to rotation of Li-Cl and Y-Cl octahedra in along all three axes, with two being in phase and one in opposite phase. According to group theoretical analysis of ordered double perovskites, this mode of rotation leads to a tetragonal phase with $P4_2/n$ space group[66, 69, 70]. As described in a previous study[66], depending on the modes of distortions, different space groups with symmetry commensurate with tetragonal Bravais lattice are possible. For tetragonal Tl_2LiYCl_6, we consider two different space groups: $P4_2/n$ (observed experimentally for Sr_2MnMoO_6[171]) and $P4_2$ (experimentally determined for Tl_2LiYCl_6[65]). Both of these structures incorporate the octahedral rotations corresponding to the most unstable mode of the cubic elpasolite Tl_2LiYCl_6 structure, as shown in the Figure 7.2. In the $P4_2$ phase, in addition to the octahedral rotations, polar displacement of cations with respect to anion sublattice are also present.

Compared to the cubic phase, there are a fewer number of unstable phonon modes in both of the tetragonal structures. In both the $P4_2$ and $P4_2/n$ crystal structures, the unstable modes are associated with either displacement of Tl within the space between the rotated octahedra or a combination of displacement of Tl ions with rotation and distortion of Li-Cl or Y-Cl octahedra. Bands with smaller imaginary frequency and very small curvature (almost flat bands), for example, at the high symmetry point A in both $P4_2$ and $P4_2/n$ structures, correspond to "rattle-like" motion of Tl ions. At finite temperatures, some of these unstable modes can be renormalized, making the structure anharmonically stable. Additionally, in some of the previously studied elpasolite systems[66], a monoclinic structure is found to be the ground state. Keeping this in mind, we study more distorted structures for Tl_2LiYCl_6 with different local Tl-Cl bonding environment. An examination of how different distortions



(a) Phonon dispersion curves of $P4_2/n$ Tl_2LiYCl_6

(b) Phonon dispersion curves of $P4_2$ Tl_2LiYCl_6

Figure 7.4: Calculated phonon dispersion curves of (a)$P4_2/n$ and (b)$P4_2$ spacegroups of Tl_2LiYCl_6. The $P4_2$ space group was reported based on refinements in neutron diffraction experiments on room-temperature Tl_2LiYCl_6. The $P4_2/n$ structure is derived from the octahedral rotations as described in the text. Both structures exhibit unstable phonon modes, originating from displacement of both Tl and Cl

modify the bulk electronic structure provides insights into exciton emission in Tl based elpasolites, which are likely to have dynamical distortions away from the average tetragonal structure at room temperature.

Ground state structure of Tl_2LiYCl_6

Considering that both of the tetragonal phases discussed above show unstable phonon modes, we attempt to find computationally the ground state structure of Tl_2LiYCl_6. In our first iteration, we randomly perturbed the internal coordinates of ions and then allowed the structure to relax with cell shape and volume fixed. This internal relaxation run generates a structure with monoclinic space group $P\bar{1}$. After performing a relaxation of the cell shape and volume, we obtain cell shape distortions that lead to a slightly lower energy and a reduction in symmetry to the P1 space group that cannot be reduced to a standard primitive cell of size less than the 320-atom size of the supercell, based on an analysis using *spglib* [172]. We note that other lower-energy structures may be possible with higher symmetry, if other supercells commensurate with this symmetry were to be considered. However, due to computational limitations, and the likely small changes in energy that would result, further analysis was not undertaken, and phonon analysis of the triclinic structure was not undertaken.

Summarizing the results on different structures of Tl_2LiYCl_6, we report the total energy per formula unit for different structures in Table 7.1. A general trend to observe is

that the Tl-Cl bond distances for the first four nearest neighbors around Tl^+ ion decreases, as we move down the list of structures with decreasing symmetry. As shown in the next section from the bulk electronic density of states, these phases of Tl_2LiYCl_6 exhibit different Tl contribution at band edges, owing to progressively more distorted Tl-Cl environments.

Structure	Energy relative to cubic elpasolite phase per formula unit(eV)	Lattice parameters Lengths (in Å)	Lattice parameters Angles
Cubic ($Fm\bar{3}m$)	0.00	(7.342 , 7.342 , 7.342)	(60°, 60°, 60°)
Tetragonal ($P4_2/n$)	-0.11	(10.310 , 10.310 , 10.500)	(90.0°, 90.0°, 90.0°)
Tetragonal ($P4_2$)	-0.12	(10.367 , 10.367 , 10.400)	(90.0°, 90.0°, 90.00°)
Triclinic (P1)	-0.15	(20.68 , 20.80 , 20.81)	(91.06°, 90.13°, 90.13°)

Table 7.1: Energy per formula unit relative to cubic elpasolite phase for different phases of Tl_2LiYCl_6. The first column gives the structure symmetry, the second the energy relative to the reference cubic phase, and the third and fourth provide the lattice parameters and cell angles for the primitive unit cells.

Tl-Cl local environments

To describe and compare the local environments involving Tl and Cl, we use Tl-Cl distances around each Tl as a metric. In the cubic cell with $Fm\bar{3}m$ symmetry, each Tl^+ ion has 12 nearest neighbor Cl^- ions which are equidistant from the Tl^+ at the center, with a calculated bond length of 3.67 Å. Upon octahedral rotation and distortion, this symmetry is broken, and we obtain multiple Tl-Cl distances around each Tl^+. We plot in Figure 7.5 the bond lengths for each of the 12 Tl-Cl bonds around each of the Tl^+ ions. For the cubic $Fm\bar{3}m$ phase with no distortions, the results yield a straight horizontal line, as depicted by black markers in Figure 7.5. We plot these curves for all 64 Tl^+ ions for the distorted cubic, the $P4_2/n$ tetragonal structure and the 320 atom triclinic structure to show how the local environments in these structures are related to each other. We also plot the distribution of Tl-Cl bond lengths in the polymorphous representation of cubic structure to show how the local distortions are distributed to create bonding motifs similar to the low symmetry tetragonal and triclinic phase.

If we only take into account the nearest neighbor Tl-Cl bond distances, all the Tl sites in the ground state structure with P1 symmetry appear to have identical chemical environment (i.e the same distribution of Tl-Cl bond lengths), even though they are distinct Wyckoff sites. This preference for the same distribution of first nearest neighbor bond lengths is driven by maximizing the overlap of Tls and Clp orbitals, as shown in the Crystal Orbital Hamiltonian Population (COHP) plots in Figure 7.8. In order to achieve this bonding for each atomic site, the structure has to be distorted.

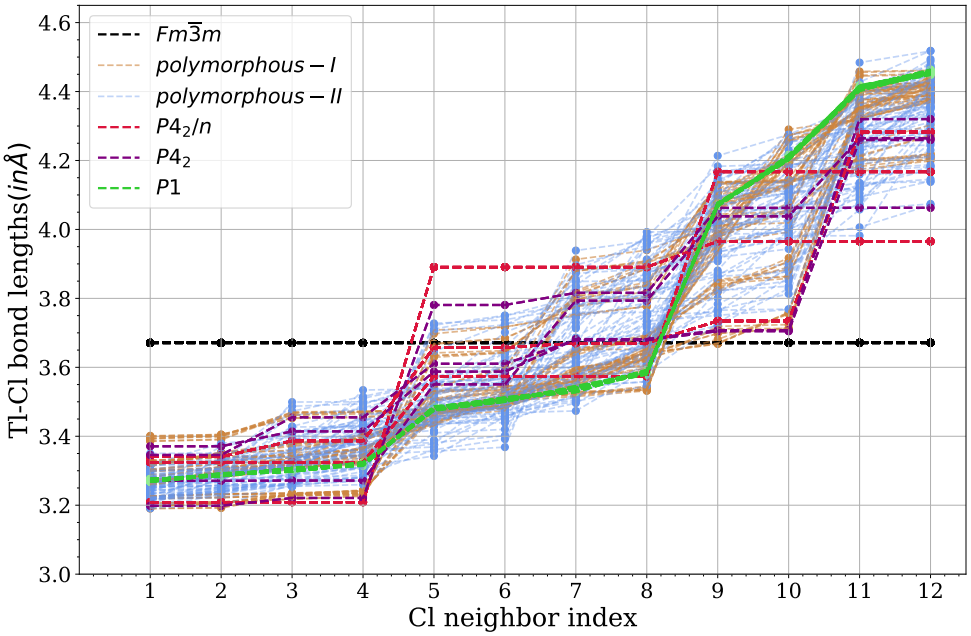


Figure 7.5: Comparison of Tl-Cl bond distances for different structures of Tl_2LiYCl_6: Fm$\bar{3}$m cubic elpasolite phase, the $P4_2/n$ and $P4_2$ tetragonal phases, P$\bar{1}$ and P1 triclinic phases and the polymorphous models of cubic structure. For each structure, the bond length to each of the 12 Cl neighbors of the distinct Tl atoms are plotted and values are connected by lines. The bond lengths are ordered by increasing value, such that the Cl neighbor index 1 (12) corresponds to the shortest (largest) bond length.

Finally, we also provide a quantitative measure of similarity between different structures, by performing a similarity analysis using a structural descriptor called many-body tensor representation (MBTR)[173], as implemented in the package DScribe [174, 175, 176]. In previous studies [62], similar methods have been used to predict formation energy of numerous elpasolite systems by creating a feature vector describing the complete structures using the averages of local structure descriptors. Here, we use MBTR as a global descriptor based on distances between Tl and Cl sites in various Tl_2LiYCl_6 structures described in this chapter. The general form of MBTR output vector of order (k) two representing a structure is of the form:

$$f_2^{MBTR}(x, z_1, z_2) = \sum_{i,j=1}^{N_a} w_2(i,j) D(x, g_{k=2}(i,j)) C_{z_1,Z_i} C_{z_2,Z_j} \tag{7.2}$$

where z_1,z_2 are atomic numbers of species, $w_2(i,j)$ is assigns weight to contributions from site i and j, $D(x, g_k(i,j))$, is a broadening function acting on $g_{k=2}(i,j)$, a function which describes some relation between sites i and j, transforming a chain of k atoms into a scalar

and C is an element correlation matrix. For the results presented in this chapter, we only consider Tl and Cl sites and use a Gaussian broadening function D on $g_2(i, j)$, which uses distances between sites i and j to create a scalar output. For the weighting scheme, we employ an exponential weighing of form $\exp^{-sx}$, thereby reducing the weight for sites farther away. The resulting MBTR vectors for different structures for Tl_2LiYCl_6, are plotted in Figure 7.6.

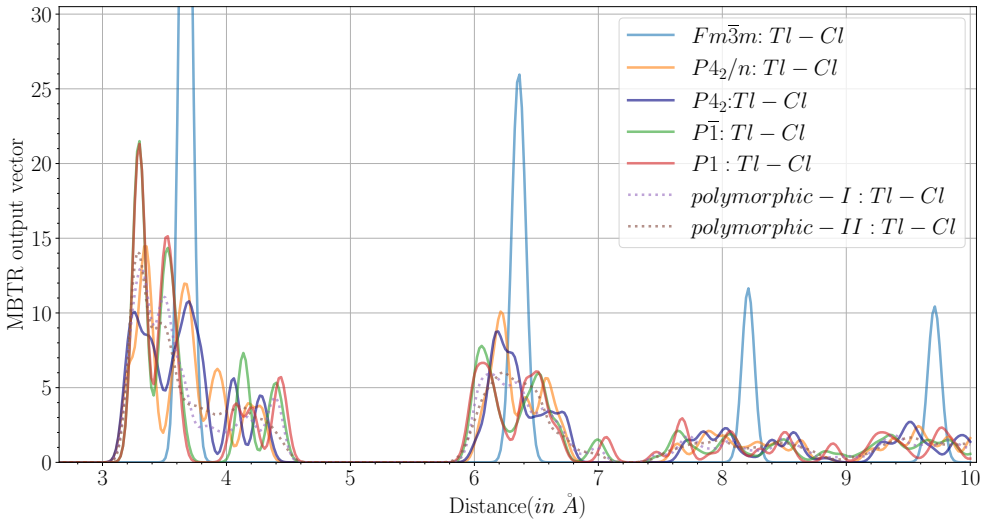


Figure 7.6: Many-body tensor representation of different structures for Tl_2LiYCl_6. The different colors correspond to the different structures of Tl_2LiYCl_6: $Fm\bar{3}m$ cubic elpasolite phase, the $P4_2/n$ and $P4_2$ tetragonal phases, $P\bar{1}$ and P1 triclinic phases and the polymorphous models of cubic structure. The x-axis and y-axis denote the Tl-Cl distances and the MBTR vector calculated using equation 7.2 as described in the text to describe each of the structure in terms of Tl-Cl bond distances.

We then calculate the similarity between different structures by applying a *pdist* distance metric. A visual representation is shown in Figure 7.7. As can be seen in Figure 7.7, $P\bar{1}$ and P1 structures have very similar description in terms of local environments. Both polymorphous representations, when described using a feature vector based on local chemical environments, are more similar to the ground state P1 phase than the cubic $Fm\bar{3}m$ or tetragonal $P4_2/n$ and $P4_2$ phase. These results support the hypothesis that the preferred local distortions in high temperature phases are derived from the ground state Tl-Cl local environments.

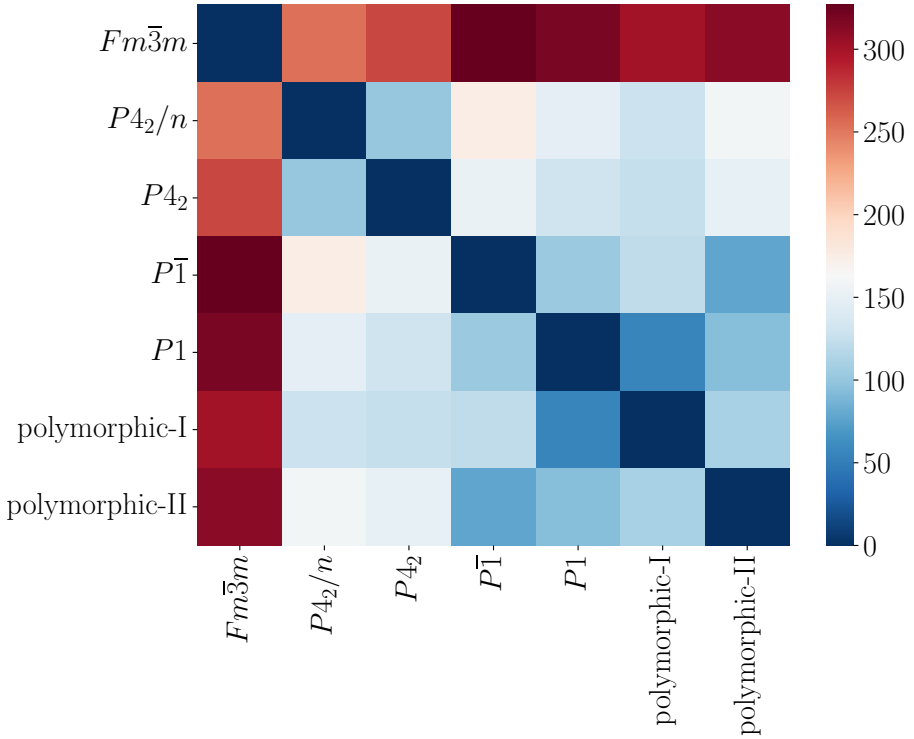


Figure 7.7: A heatmap describing similarity between different phases and polymorphous representation of Tl_2LiYCl_6. From left to right and top to bottom, the phases are $Fm\bar{3}m$, $P4_2/n$, $P4_2$, $P\bar{1}$, P1 and two different polymorphic representations of cubic cell.

7.2 Electronic and Optical properties of cubic and other low energy phases of Tl_2LiYCl_6

We now focus on understanding the atomistic origins of observed emission from bulk Tl_2LiYCl_6. As described in the previous experimental studies [64], the exciton state responsible for observed emission is likely centered on the Tl^+ ions. This is in contrast to the findings in computational investigations of bound excitons in bulk Cs_2LiYCl_6, where the stable exciton was from a V_k like hole state and an electron state centered on a nearby Y ion [57].

We start by investigating the orbital character of bulk valence and conduction band edges in Tl_2LiYCl_6. Previous work on electronic structure of scintillator materials highlight the importance of hole trapping states near the valence band maximum in order to stabilize a bound exciton. More specifically, for ternary halide scintillators with Tl as part of the bulk, such as Tl_2LaCl_5, calculations have shown the presence of Tl states at the valence band maximum. It was suggested that the presence of these states aids the hole trapping at

Tl^+ sites which leads to exciton capture on this ion[49, 163]. In ordered double perovskites, the contributions of different elements to states at the band edges primarily depends on the structure and on the relative electronegativities of constituent ions. As reviewed extensively in previous sections, Tl_2LiYCl_6 has a significantly different structure than Cs_2LiYCl_6 which explains the difference in exciton responsible for observed emission. Here, we focus on the room temperature tetragonal phase of Tl_2LiYCl_6, and compare stability and emission energies of different possible exciton states in that system using PBE0 constrained electronic structure calculations.

Bulk Electronic Structure of Tl_2LiYCl_6: Effect of distortions

As shown in the Figure 7.9, the distortion of Tl-Cl coordination plays an important role in determining the Tl contribution to the electronic states at the valence and conduction band edges. The Tl contribution in undistorted cubic elpasolite Tl_2LiYCl_6 is negligible at the valence band edges, as shown in Figure 7.9. As the octahedral rotations and distortions are included in Tl_2LiYCl_6, the contribution of Tl at the band-edges increases.

For further understanding of the electronic driving forces for distortions, we can perform a Crystal Orbital Hamiltonian Population (COHP) analysis[117, 118], which can decompose the electronic states into bonding and anti-bonding contributions for different orbital overlap. In Figure 7.8, we show COHP plots for the undistorted cubic ($Fm\bar{3}m$) and the tetragonal phases ($P4_2/n$ and $P4_2$). As shown in element decomposed electronic density of states in Figure 7.9, the Tl contribution increases significantly with lattice distortions. The COHP plots generated using LOBSTER software[119, 120] show that the Tl-Cl hybridized states are anti-bonding in nature right below the valence band maximum. Similar character of electronic density of states has been previously found to be a signature of lone pairs in Pb based oxides [52, 53]. The anti-bonding states are formed by the overlap of Tl-6s and Cl-3p orbitals. The presence of distortions removes the symmetry constraints, allowing interaction between unoccupied cation 6p states with the anti-bonding orbitals resulting in a net stabilizing effect[52]. Although Tl shows significantly less lone pair effects than Pb[52], we believe that similar effects are likely to be at play here, even though at a lower magnitude than the Pb counterparts. The antibonding character of the valence-band is also seen in TlBr[56, 53], an alkali halide scintillator.

The absence of Tl s states at the valence band maximum in undistorted cubic Tl_2LiYCl_6 with $Fm\bar{3}m$ symmetry provides a possible explanation for the difference in nature of self-trapped exciton state in Tl_2LiYCl_6 and Cs_2LiYCl_6. Apart from acting as an intrinsic activation center, Tl^+ ion also leads to preference for distorted (dynamic or static) Tl-Cl local environments, to maximize the overlap of Tl 6s and Cl 3p orbitals. Due to Tl^+ ion being a preferred hole trapping site, we show in the following section that the structure of the stable bound exciton is also different in these two systems.

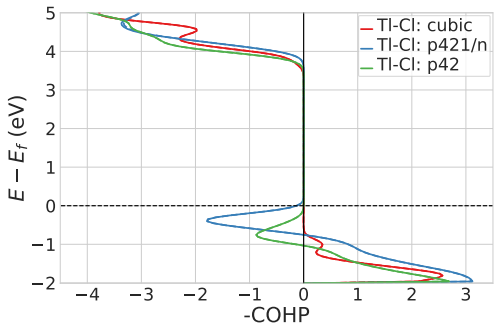


Figure 7.8: Crystal Orbital Hamiltonian Population plots for Tl_2LiYCl_6

Electronic Structure of excited state in Tl_2LiYCl_6

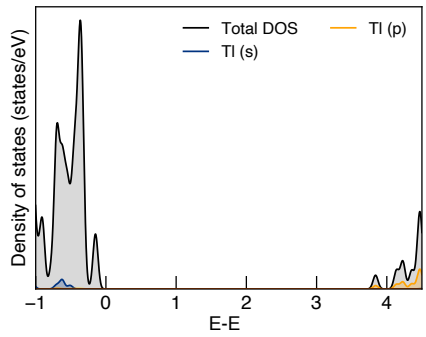
To study the electronic structure of bound exciton states in Tl_2LiYCl_6, we performed constrained DFT calculations using the ground state structure of Tl_2LiYCl_6 with P1 symmetry. As described in section 3.4, due to the importance of achieving correct localization of hole and electrons, we used PBE0 hybrid functional[81] to perform the constrained DFT simulations. The resulting hole and electron wavefunctions are shown in Figure 7.10.

As can be seen in Figure 7.10, in the distorted P1 triclinic structure of Tl_2LiYCl_6, we can form three types of excitons: V_k like hole state and an electron state centered on nearby Y, V_k like hole state and an electron state centered on nearby Li ion or both electron and hole states centered on Tl ion. The relative energies and approximate emission energies are given in Table 7.2.

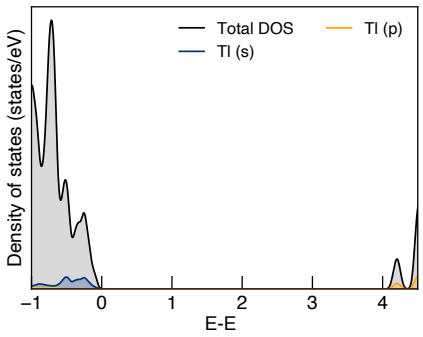
Configuration	Relative Formation Energy (eV)	Emission Energy (eV)
Tl-centered	0	3.30
Tl+V_k(Y)	0.095	1.79
Tl+V_k(Li)	0.405	1.73

Table 7.2: Formation energies and emission energies of different configurations of excitons in triclinic P1 Tl_2LiYCl_6. All the formation energies are relative to the lowest energy exciton configurations found.

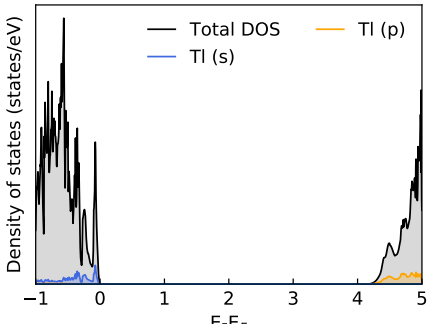
In distorted P1 triclinic P1 Tl_2LiYCl_6, we find three stable exciton states. Out of these three, the exciton centered at the Tl^+ ion is the most stable. The other possible bound exciton, which is found in other halide materials, has a V_k-like hole state in which a hole is localized on two adjacent halides (Cl^- in this case). The V_k-like hole state is stabilized by the two halide ions moving closer. We see that in triclinic P1 Tl_2LiYCl_6, we can form two



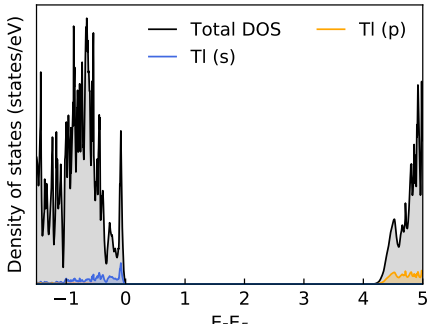
(a) Cubic elpasolite Tl_2LiYCl_6



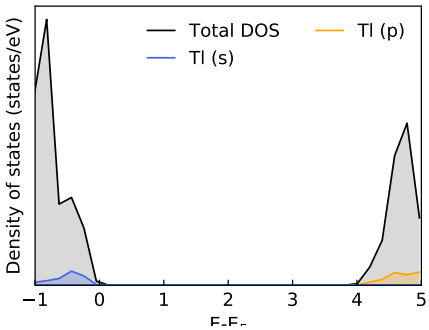
(b) Cubic $Tl_2LiYCl_6$with distortions



(c) Tetragonal Tl_2LiYCl_6- $P4_2/n$



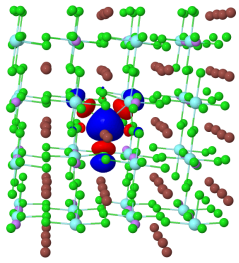
(d) Tetragonal Tl_2LiYCl_6- $P4_2$



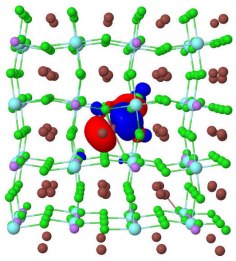
(e) Triclinic Tl_2LiYCl_6- P1

Figure 7.9: Density of states with Tl contribution for different structures of Tl_2LiYCl_6

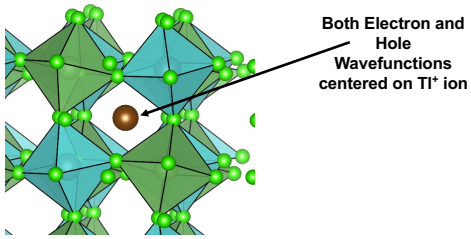
such excitons. Both of these excitons contain a V_k-like hole state but differ in localization of the electron at Y^{3+} and Li^{+}. Out of these two, the exciton centered at Y^{3+} appears to be much more stable, with formation energy comparable to the Tl centered counterpart. At non-zero temperature, it is possible that both of these excitons can co-exist. However, the calculated emission energies are significantly different from the values measured experimen-



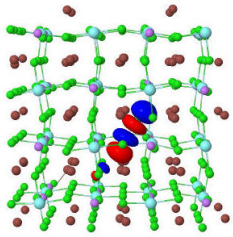
(a) Hole state Wavefunction centered at Tl



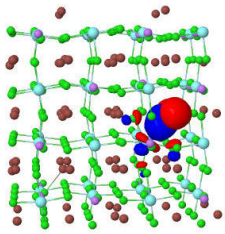
(b) Electon state Wavefunction centered at Tl



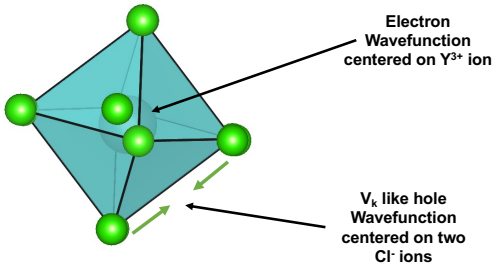
(c)



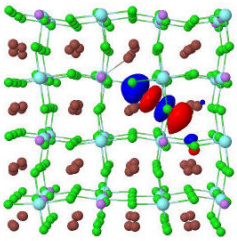
(d) Vk like hole state wavefunction



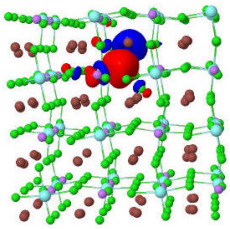
(e) Electron state wavefunction centered at Y^{3+}



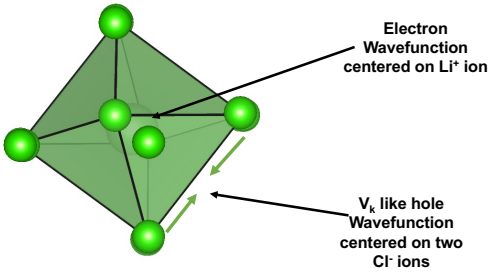
(f)



(g) Vk like hole state wavefunction



(h) Electron state wavefunctions centered at Li^+



(i)

Figure 7.10: Different exciton configurations found in triclinic P1 Tl_2LiYCl_6 structure. Subfigure (a) shows the Tl-centered electron and hole wavefunctions for most stable exciton configuration. (b) and (c) correspond to bound exciton with a V_k like hole state and electron localized on Y^{3+} and Li^+ respectively. All the Tl sites in the triclinic structure have identical nearest neighbor local environment.

tally[64]. The approximate emission energies are calculated using the Δ-SCF approach using PBE0 calculations, as explained in more detail in section 3.4.

Comparing with experimental data, the emission energy of the Tl^+ centered exciton agrees better with the broad emission peak at 2.9 eV as seen in the measured emission spectra[64]. We hypothesize that the migration from a Y^{3+} to a nearby Tl^+ site must be very fast, resulting in net emission from Tl^+.

Previous DFT studies undertaken for undoped bulk Cs_2LiYCl_6 found an excitonic emission attributed to the recombination of a V_k like hole state and an electron state centered on nearby Y ion [57]. Comparing the hole state of the exciton in Tl_2LiYCl_6 with that of the bound exciton in Cs_2LiYCl_6 (which exists as a perfect cubic structure at room temperature) we can see the influence of Tl states at the valence band maximum. Similar to Tl doped alkali halides such as CsI:Tl, both hole and electron wavefunctions are localized on the same Tl^+ ion. This is possible as Tl^+ can act as a hole trap due to the presence of $6s$ orbitals, unlike Cs^+. In the case of Tl_2LiYCl_6, as a result of the structural distortions, Tl-s states are present at the valence band maximum and can efficiently trap a hole.

Here, we would like to note that the structural distortions in the P1 groundstate structure are crucial in stabilizing different exciton configurations. For cubic Tl_2LiYCl_6 and tetragonal Tl_2LiYCl_6 with $P4_2/n$ symmetry, we tried initializing the structure for constrained hybrid calculation, by displacing two adjacent Cl^- ions towards each other and allowing the structure to relax under the multiplicity constraint. We were unable to form a localized bound exciton with V_k like hole state. The hole state of this exciton resembled a V_k center, but the electron state was delocalized. We find that in the above simulation, the highest occupied orbital (corresponding to the electronic part of exciton) is delocalized over several Tl ions. This configuration is also higher in energy than the bound exciton, with both electron and hole densities centered on a single Tl^+ ion.

In case of tetragonal Tl_2LiYCl_6 with $P4_2/n$ symmetry, there are three distinct Tl^+ sites based on the first nearest neighbor Tl-Cl bond distances. In a separate set of PBE0 calculations, we were able to stabilize Tl-centered bound excitons on each of these sites by creating initial distortions which reduces local Tl-Cl bond distances, and then performing structural relaxation as described in section 3.4. The resulting exciton formation with respect to the most stable configuration and binding energies are listed in table 7.3. The most stable bound exciton is found on the Tl site with the lowest average first nearest neighbor Tl-Cl bond lengths. Compared to the binding energy of Tl-centered exciton in the triclinic structure (3.30 eV) described in the beginning of this section, the binding energy of the most stable exciton in the tetragonal structure with $P4_2/n$ symmetry (3.11 eV) is closer to the experimentally measured broad peak in emission spectra (2.9 eV)[64].

In a separate set of DFT simulations, modelling a localized hole state in this system, we find that it is possible to localize both a Tl centered hole and a hole centered on adjacent Cl ions in the form of a V_k center. The Tl localized hole is lower in energy than the V_k type

Configuration	Relative Formation Energy (eV)	Emission Energy (eV)
Tl-centered-I	0	3.11
Tl-centered-II	0.45	3.01
Tl-centered-III	0.62	3.61

Table 7.3: Formation energies and emission energies of different configurations of excitons localized on three distinct Tl sites in tetragonal Tl_2LiYCl_6 with $P4_2/n$ symmetry. All the formation energies are relative to the lowest energy exciton configurations found.

hole. This further supports the hypothesis that in the case of a bound exciton formation by subsequent carrier capture, the probability of electron trapping on a Tl site with a bound hole will be larger. A more accurate and definitive validation will require calculating carrier capture cross-sections and carrier transport, which can provide a better understanding of materials modelling of scintillators and can inform future materials search efforts.

For the sake of completeness and comparison with Cs_2LiYCl_6, existing as a cubic elpasolite at room temperature, we also performed similar constrained DFT simulations in the polymorphic representation of the cubic elpasolite phase of Tl_2LiYCl_6 which has overall a cubic supercell but with local distortions similar to the low energy P1 phase as can be seen by structural similarity plotted in Figure 7.7. We find that a similar Tl centered bound excited state was stable in that system as well. As the bound exciton in Tl_2LiYCl_6 is likely to be localized and the dynamic distortions around the Tl^+ ions in the cubic elpasolite phase are similar to the ones found in the lower energy structures with reduced symmetry found as the ground state at lower temperatures, we believe this provides a qualitatively accurate picture of bound excitons found in finite-temperature cubic elpasolite phase of undoped bulk Tl_2LiYCl_6.

Chapter 8

Conclusions and Future Work

The research performed for this dissertation was undertaken for two different projects motivated by studying very different properties such as ion transport and scintillation in two distinct classes of materials: iron oxides (Fe_3O_4 and Fe_2O_3) and Tl_2LiYCl_6. Both of the systems and types of properties considered possess conceptual similarity in the form of complexities associated with simulating localized point defect and exciton states strongly coupled with local charge and structural environments. Chapters 4, 5 and 6 were related to point defect properties in magnetite (Fe_3O_4) and hematite (Fe_2O_3). After providing a justification for the presence of charge ordering in cubic magnetite at ambient temperatures in chapter 4, effects of resulting local environments on various spin and charge configurations of oxygen vacancies were studied. It was found that the charge redistribution associated with formation of iron and oxygen vacancies as well as bound di-vacancies affects the relative stability of these defects. The results suggest local order can have important effects on the pathways and rates of ionic hopping in magnetite that should be accounted for in transport models at low and intermediate temperatures, where local charge order is pronounced.

The results and discussion provided in chapter 7 employed DFT and constrained-DFT calculations to investigate the nature of bound excitons responsible for emission in Tl_2LiYCl_6. The binding energy and stability of localized excitons is found to be influenced by the distortions in the local structural environments and corresponding electronic states around the binding site. To this end, we performed a detailed and systematic analysis of the local distortions and Tl-Cl environments found in different structural phases of bulk Tl_2LiYCl_6. The presence of both Tl^+ and Cl^- ions leads to the distortions away from the reference cubic elpasolite structure, to lower the energy. The presence of distortions has its origin in the relatively small ionic size of Tl^+ and hybridization of Tl-s and Cl-p orbitals. These distortions persist as we move down in symmetry from cubic to tetragonal to triclinic phases, leading to multiple near-degenerate structures in the low-energy structures. This leads to a significant Tl contribution to the character of the electron states at the valence band edge, which aids in capturing of an exciton at Tl sites. The results provide guidelines for the discovery of new scintillator materials which involve Tl-halide chemical environments in their bulk structure.

The above analysis highlights the importance of correctly capturing the distortion of the perovskite lattice when modelling the bound exciton properties in the double-perovskite halide compounds containing Tl^+. These distortions can be static or dynamic. Recent work performed on the polymorphous nature of such cubic halide perovskite systems[67] provides a way to generate a representation of bulk electronic and crystal structures.

8.1 Extension of the iron oxide work

Studying atomistic behavior of point defects in iron-oxides can be challenging owing to the difficulties associated with current electronic structure methods in describing correlated electronic structure and localized electronic structure. Moreover, understanding ion transport mechanisms at play, requires simulating diffusion processes in larger systems for long time-scales. The proposed future work highlights the limitations of results presented in this thesis and suggests methods for improving their accuracy as well as further calculations which can be performed.

Choice of electronic structure methods

The primary motivation for using Hubbard-U corrections in our electronic structures calculations is removing the self-interaction error inherent in approximations made in the GGA formalism. In terms of the dependence of total energy with respect to orbital occupation, the removal of self-interaction is manifested as linearity in total energy versus number of electrons in the system. We chose the effective Hubbard U value as the one which satisfies this linearity condition, as shown in Figure 3.1.

However, this correction is only applied to the d orbitals of the iron atoms. This changes the local chemical potential of electrons occupying these orbitals, effectively shifting their energies not just with respect to the s and p orbitals on the iron but also the oxygen p orbitals. For oxide systems with significant covalent character, it has been shown that merely applying the Hubbard U correction to only transition metal d orbitals can reduce the degree of hybridization between cation d and anion p orbitals, in some cases at the detriment of prediction of physical properties such as equilibrium geometries, bond angles, orbital character of the band edges and more[177, 78]. An extended formulation of the DFT+U method, called DFT+U+V[177] has been proposed in the literature, which includes an additional term for inter-site interactions between electrons on orbitals located on neighboring sites, which can improve the description of hybridization between cation-d and anion-p states.

A recently published study[178] employed DFT+U+V methodology to calculate the electronic structure of bulk magnetite in its cubic inverse spinel structure. Along with increase in curvature of bands near the Fermi level resulting from increase in hybridization between oxygen $2p$ and iron $3d$ orbitals, this study also found that the U and V values, calculated using linear response approach[179], differ for octahedral and tetrahedral sites by around

0.6 eV. Dependence of U values on the local coordination has also been explored in other studies and is not unexpected. In the popular formalism of applying the Hubbard U corrections, where the U values are derived from a linear response approach to minimizing the local curvature of the energy with respect to addition or removal of electrons from a localized orbital (subshell denoted by n,l to the rest of the system at constant charge)[180, 78]. Therefore, the resulting Hubbard U value can be site-dependent, as the chemical bonding environments are changed. This however poses a challenge for finding optimal parameters for these Hubbard-like corrections where the local environments of ions are not always known a-priori, such as finding a defect migration pathways which can involve new coordination environments and local hybridization. Additionally, it has been shown that in cases where treating non-collinear spins accurately is important, other modifications such as accounting for screening by opposite spin channels on the same site[181] in calculating U and J values and using source-free formulations of exchange correlation functional might be needed[182].

For the purpose of defect simulations, especially in calculating the migration barriers and pathways, allowing the spins to be oriented at various angles might be necessary to obtain the minimum energy configurations. Considering the complex interdependence of local structural, spin and charge degrees of freedom found in transition metal oxides, including iron oxides, the functional form of the dependence of U, J and V values on local environments could be very complicated. Uses of machine learning with applying important physical constraints to calculate approximations to the exchange correlation functional[183] and calculation of local properties are emerging areas of interest[184, 185]. Developing methodologies and inferring the dependence of U, J and V values on local environments is a very interesting problem for applying statistical inference methods such as machine learning and would be extremely helpful in widening the scope of applications where we can make reasonable prediction of materials properties, including but not limited to mass transport through diffusion and radiation tolerance of oxides.

Defect calculations in iron oxides

Use of Hubbard U corrections for DFT calculations of iron oxides poses a challenge for defect formation energy calculations in the form of required correction to electron and atomic chemical potential reference energies. The electron chemical potential given by the Fermi level is affected by self-interaction error, which can be corrected by using appropriate U, J and V values, as described above. However, the same corrections might not be optimal for getting the relative energies of different phases correct. Numerous schemes for corrections to energies of reference phases and compounds to get the correct convex hull have been proposed in the literature[186] and exploring and refining these for the iron oxygen system, while being consistent with the optimal values required for maintaining the correct values of relative electron chemical potentials, will be very useful in developing models for multi-layer

growth of oxides on iron and other applications requiring such heterostructures.

When predicting the stability of defects at non-zero temperatures, the entropy contribution to the Gibbs Free Energy might be significant in changing the relative values of formation energies[187]. The two contributions to entropy which could be important are configurational and vibrational entropy. The entropy associated with these point defects could not just affect the free energies of the defect configurations, but can also significantly affect the chemical potentials used for calculating formation energies, possibly changing the most stable defect configurations at high temperature through change in formation free energies. In the case of magnetite (Fe_3O_4), the point defects lead to redistribution of electrons and holes. Considering the near-degeneracy of different charge distributions around a defect site, at high enough temperatures, these could contribute significantly to the configurational entropy associated with formation of point defects.

Defect Kinetics in magnetite

In addition to improving the description of the electronic structure, predicting ion transport in iron oxides would also require development of force-fields to run long timescale simulations on large cells. Developing empirical force-fields for oxide materials is not trivial due to the complexity of interactions and atomic scale processes involved. Apart from accounting for spins and variable charges, polarization of ions also need to be treated well by the potential to capture the energetics of diffusion pathways and subsequent rearrangement of local structure[38, 188]. As seen in the results presented in the previous chapters of this thesis, the formation of defects is accompanied by the redox of surrounding ions. To capture this phenomenon in force-fields, the net charge and spin on an ion has to be allowed to vary within the simulation. These effects are even more important when simulating interfaces, as the misalignment of band-edges between two structurally and electronically dissimilar phases is often accompanied by formation of a space-charge layer, a highly defective or new oxide phases at the interface and sometimes even a 2D electron gas. Recently, machine-learned interatomic potentials (MLIP) have become a popular form of force-fields to simulate complex phenomenon where the known empirical functional forms are not sufficient to model all the interactions[189, 188]. Even though in the newer generations of MLIPs it is possible to include the charges explicitly[190, 191, 192, 193], the training process is complicated by the problem of charge partitioning in DFT and use of smaller cutoffs. These charge-aware potentials have not yet been developed for iron oxides, and further work in this area would be needed for realistic modelling of transport processes and interfaces of oxides. In addition to including the electrostatics resulting from point charges, dipoles and quadrupoles, allowing for charge transfer would also be a crucial aspect for capturing redox which often accompanies defect formation and transport phenomenon. Interatomic potential forms which allow for change in type of bonding (reactive force-fields) have been used to perform such atomistic simulations in oxides[194], but there is scope for further improvement in the accuracy and genralizability of such potentials.

8.2 Extension of the Tl_2LiYCl_6 work

A comprehensive understanding of scintillation behavior of a material involves understanding not only the nature of bound excitons, but also the dynamics of exciton transport and identifying all possible mechanisms for charge trapping and transport[45]. In this study, we focused only on how different local environments in Tl_2LiYCl_6 can enable multiple exciton configuration depending upon local Tl-Cl bonding. We did not, in particular, comment on how this exciton forms or is captured, and if the less stable configurations can transform into the most stable one, before recombination of electron and hole states. Since an exciton inherently is a two-particle state, the single particle approximation in the formulation of DFT used for the results in the chapter 7, in itself needs to be improved upon. Suggested future work presented in this section aims to address these limitations and further calculations which can be performed for better prediction of scintillation properties in Tl_2LiYCl_6.

Choice of electronic structure methods

While the Δ-SCF method allows us to create an approximate model for the excited state, it restricts us to be only able to simulate the triplet-state of the exciton due to the spin constraints, forcing the spin state of electron and hole wavefunction to be the same. Moreover, the effect of interaction between electron and hole states as well as many-body nature of electronic polarization are not taken into account. These deficiencies, in principle, can be corrected by using many-body perturbation methods such as GW-BSE[195]. Methods such as GW approximation, generally improve upon the Kohn-Sham eigenvalues by recognizing that in an extended system, all the electrons participate in screening interactions, and utilize a first order perturbative correction to Kohn-Sham eigenvalues, taking into account the screened Coulomb interaction and dynamical screening effects. For simulating two-particle states such as bound excitons, a two-particle Green's function approach can be implemented using the Bethe-Selpter equation (BSE)[196]. Although quite accurate, these methods are computationally quite expensive. Nevertheless with the advent of highly parallel electronic structure codes such as BerkeleyGW[197] and exascale infrastructure[198], it is becoming more feasible to use GW-BSE methods to calculate the emission spectra of larger systems with extended distortions such as Tl_2LiYCl_6.

Including Phonon Effects

In addition to using more accurate electronic structure methods, it is also important to account for phonon effects in Tl_2LiYCl_6 in the form of anharmonic stability and exciton-phonon interactions. Phase stability at non-zero temperatures is determined by Gibbs Free Energy which includes a combination of internal energy and entropic effects, usually occuring in the form of vibrational entropy for materials without compositional disorder. As described in chapter 7, phonon dispersion calculated under the harmonic approximation dis-

plays imaginary frequencies for cubic and tetrahedral structures. In order to obtain a more accurate picture of stability of these phases, we need to consider the possibility of anharmonic contributions to the lattice vibrations and calculate the corresponding phonon dispersion. In addition to determining the stability of bulk phases, anharmonicity of phonons can also lead to band gap renormalization, possibly impacting the nature of band-edge states[199]. Calculating anharmonic phonon spectra can be computationally expensive as it requires calculating/fitting higher-order force constants, which in turn requires much more extensive sampling of distortions in the system. While these distortions can be obtained from dynamical sampling using long molecular dynamics trajectories, less expensive sampling methods based on using regression algorithms have been suggested in the literature[200]. Employing these methods to calculate anharmonic vibrational spectra for the cubic and room-temperature tetragonal structure will enable a more complete understanding of role of distortions and their dynamical nature in exciton emission in Tl_2LiYCl_6.

Effect of phonons on scintillator behavior can also appear in the form of electron-phonon coupling effects. Exciton-phonon coupling can manifest itself in the form of temperature dependence of exciton lifetimes, mean free path and absorption or emission spectra [199, 201]. In ionic compounds such as metal halide perovskites, an effective dielectric constant is usually employed to account for both electrons and phonons screening the interaction between the electron-hole pair. However, recent studies[202, 203], have explicitly included certain phonon modes to calculate the exciton binding energies to elucidate the importance of understanding the mechanism of the screening and improve the binding energy predictions. Considering the importance of distortions in stabilizing certain bound exciton configurations in Tl_2LiYCl_6 and the possible dynamical nature of these distortions for the room-temperature phases, further work should be done on Tl_2LiYCl_6 and other Tl based elpasolites, to study the nature of exciton-phonon coupling in these systems.

Bibliography

[1] Zimin Li et al. "Mechanism and kinetics of magnetite oxidation under hydrothermal conditions". en. In: *RSC Adv.* 9.58 (2019), pp. 33633–33642. ISSN: 2046-2069. DOI: 10.1039/C9RA03234G.

[2] Gisella Palma et al. "A review of magnetite geochemistry of Chilean iron oxide-apatite (IOA) deposits and its implications for ore-forming processes". en. In: *Ore Geology Reviews* 126 (Nov. 2020), p. 103748. ISSN: 01691368. DOI: 10.1016/j.oregeorev.2020.103748.

[3] Francisco Velasco, Fernando Tornos, and John M. Hanchar. "Immiscible iron- and silica-rich melts and magnetite geochemistry at the El Laco volcano (northern Chile): Evidence for a magmatic origin for the magnetite deposits". en. In: *Ore Geology Reviews* 79 (Dec. 2016), pp. 346–366. ISSN: 01691368. DOI: 10.1016/j.oregeorev.2016.06.007.

[4] Hongping He et al. "Natural Magnetite: an efficient catalyst for the degradation of organic contaminant". en. In: *Sci Rep* 5.1 (Sept. 2015), p. 10139. ISSN: 2045-2322. DOI: 10.1038/srep10139.

[5] Shu Nie et al. "Insight into Magnetite's Redox Catalysis from Observing Surface Morphology during Oxidation". In: *J. Am. Chem. Soc.* 135.27 (July 2013), pp. 10091–10098. ISSN: 0002-7863. DOI: 10.1021/ja402599t.

[6] Macarena Munoz et al. "Preparation of magnetite-based catalysts and their application in heterogeneous Fenton oxidation – A review". en. In: *Applied Catalysis B: Environmental* 176-177 (Oct. 2015), pp. 249–265. ISSN: 0926-3373. DOI: 10.1016/j.apcatb.2015.04.003.

[7] T. B. Scott et al. "Reduction of U(VI) to U(IV) on the surface of magnetite". en. In: *Geochimica et Cosmochimica Acta* 69.24 (Dec. 2005), pp. 5639–5646. ISSN: 0016-7037. DOI: 10.1016/j.gca.2005.07.003.

[8] Takashi Tsuchiya et al. "*In* Situ Tuning of Magnetization and Magnetoresistance in Fe O Thin Film Achieved with All-Solid-State Redox Device". en. In: *ACS Nano* 10.1 (Jan. 2016), pp. 1655–1661. ISSN: 1936-0851, 1936-086X. DOI: 10.1021/acsnano.5b07374.

[9] Ai I Osaka et al. "Nondeteriorating Verwey Transition in 50 nm Thick Fe O Films by Virtue of Atomically Flattened MgO Substrates: Implications for Magnetoresistive Devices". en. In: *ACS Appl. Nano Mater.* 4.11 (Nov. 2021), pp. 12091–12097. ISSN: 2574-0970, 2574-0970. DOI: 10.1021/acsanm.1c02634.

[10] James E. Castle and P. L. Surman. "Self-diffusion of oxygen in magnetite. Effect of anion vacancy concentration and cation distribution". en. In: *J. Phys. Chem.* 73.3 (Mar. 1969), pp. 632–634. ISSN: 0022-3654, 1541-5740. DOI: 10.1021/j100723a025.

[11] R. Dieckmann and H. Schmalzried. "Defects and Cation Diffusion in Magnetite (II)". en. In: *Berichte der Bunsengesellschaft für physikalische Chemie* 81.4 (Apr. 1977), pp. 414–419. ISSN: 00059021. DOI: 10.1002/bbpc.19770810412.

[12] R. Dieckmann. "Defects and Cation Diffusion in Magnetite (IV): Nonstoichiometry and Point Defect Structure of Magnetite (Fe3-O4)". en. In: *Berichte der Bunsengesellschaft für physikalische Chemie* 86.2 (Feb. 1982), pp. 112–118. ISSN: 00059021. DOI: 10.1002/bbpc.19820860205.

[13] B.J. Giletti and K.C. Hess. "Oxygen diffusion in magnetite". en. In: *Earth and Planetary Science Letters* 89.1 (June 1988), pp. 115–122. ISSN: 0012821X. DOI: 10.1016/0012-821X(88)90037-4.

[14] Hebatalla Elnaggar et al. "Temperature-Driven Self-Doping in Magnetite". en. In: *Phys. Rev. Lett.* 127.18 (Oct. 2021), p. 186402. ISSN: 0031-9007, 1079-7114. DOI: 10.1103/PhysRevLett.127.186402.

[15] Alexey Bosak et al. "Short-Range Correlations in Magnetite above the Verwey Temperature". en. In: *Phys. Rev. X* 4.1 (Mar. 2014), p. 011040. ISSN: 2160-3308. DOI: 10.1103/PhysRevX.4.011040.

[16] Y. Yamada, N. Wakabayashi, and R. M. Nicklow. "Neutron diffuse scattering in magnetite due to molecular polarons". en. In: *Phys. Rev. B* 21.10 (May 1980), pp. 4642–4648. ISSN: 0163-1829. DOI: 10.1103/PhysRevB.21.4642.

[17] Mark S. Senn et al. "Electronic orders in the Verwey structure of magnetite". en. In: *Phys. Rev. B* 85.12 (Mar. 2012), p. 125119. ISSN: 1098-0121, 1550-235X. DOI: 10.1103/PhysRevB.85.125119.

[18] Mark S. Senn et al. "Charge localization in the Verwey structure of magnetite". en. In: *Phys. Rev. B* 92.2 (July 2015), p. 024104. ISSN: 1098-0121, 1550-235X. DOI: 10.1103/PhysRevB.92.024104.

[19] D. O. Smith. "Magnetization of a Magnetite Single Crystal Near the Curie Point". In: *Phys. Rev.* 102.4 (May 1956), pp. 959–963. DOI: 10.1103/PhysRev.102.959.

[20] N. Berdunov et al. "Atomically Resolved Spin-Dependent Tunneling on the Oxygen-Terminated \mathrmF\mathrme_3\mathrmO_4(111)". In: *Phys. Rev. Lett.* 93.5 (July 2004), p. 057201. DOI: 10.1103/PhysRevLett.93.057201.

[21] Vojtěch Chlan et al. "Electronic structure and hyperfine fields in non-stoichiometric magnetite above the Verwey transition". In: *Journal of Magnetism and Magnetic Materials* 322.9 (2010), pp. 1079–1081. ISSN: 0304-8853. DOI: https://doi.org/10.1016/j.jmmm.2009.03.026.

[22] H. Elnaggar et al. "Noncollinear Ordering of the Orbital Magnetic Moments in Magnetite". en. In: *Phys. Rev. Lett.* 123.20 (Nov. 2019), p. 207201. ISSN: 0031-9007, 1079-7114. DOI: 10.1103/PhysRevLett.123.207201.

[23] Francis Millot and Niu Yan. "Diffusion of O18 in Fe3O4: An experimental approach to study the behavior of minority defects in oxides". en. In: *Journal of Physics and Chemistry of Solids* 58.1 (Jan. 1997), pp. 63–72. ISSN: 0022-3697. DOI: 10.1016/S0022-3697(96)00101-1.

[24] E. J. W. Verwey. "Electronic Conduction of Magnetite (Fe3O4) and its Transition Point at Low Temperatures". en. In: *Nature* 144.3642 (Aug. 1939), pp. 327–328. ISSN: 1476-4687. DOI: 10.1038/144327b0.

[25] H. Kronmüller, R. Schützenauer, and F. Walz. "Magnetic After-Effects in Magnetite". en. In: *Phys. Stat. Sol. (a)* 24.2 (Aug. 1974), pp. 487–494. ISSN: 00318965, 1521396X. DOI: 10.1002/pssa.2210240214.

[26] "Mössbauer spectroscopy of stoichiometric and non-stoichiometric magnetite". en. In: *Journal of Physics and Chemistry of Solids* 30.6 (June 1969), pp. 1561–1571. ISSN: 0022-3697. DOI: 10.1016/0022-3697(69)90217-0.

[27] R. Arras, L. Calmels, and B. Warot-Fonrose. "Half-metallicity, magnetic moments, and gap states in oxygen-deficient magnetite for spintronic applications". en. In: *Appl. Phys. Lett.* 100.3 (Jan. 2012), p. 032403. ISSN: 0003-6951, 1077-3118. DOI: 10.1063/1.3678028.

[28] O. Mounkachi et al. "Effect of Defects Disorder on the Half-Metallicity, Magnetic Properties, and Gap States of Fe3O4: a First-Principles Study". en. In: *J Supercond Nov Magn* 30.11 (Nov. 2017), pp. 3221–3224. ISSN: 1557-1939, 1557-1947. DOI: 10.1007/s10948-017-4108-3.

[29] R Arras, B Warot-Fonrose, and L Calmels. "Electronic structure near cationic defects in magnetite". en. In: *Journal of Physics: Condensed Matter* 25.25 (June 2013), p. 256002. ISSN: 0953-8984, 1361-648X. DOI: 10.1088/0953-8984/25/25/256002.

[30] Christopher L. Muhich et al. "First-Principles Analysis of Cation Diffusion in Mixed Metal Ferrite Spinels". en. In: *Chemistry of Materials* 28.1 (Jan. 2016), pp. 214–226. ISSN: 0897-4756, 1520-5002. DOI: 10.1021/acs.chemmater.5b03911.

[31] Steven T. Hartman and Ghanshyam Pilania. "Defect thermodynamics in spinel oxides leading to plasmonic behavior". en. In: *Journal of Physics and Chemistry of Solids* 168 (Sept. 2022), p. 110822. ISSN: 00223697. DOI: 10.1016/j.jpcs.2022.110822.

[32] M I Shutikova and V V Stegailov. "Frenkel pair formation energy for cubic Fe O in DFT + U calculations". en. In: *Journal of Physics: Condensed Matter* 34.47 (Nov. 2022), p. 475701. ISSN: 0953-8984, 1361-648X. DOI: 10.1088/1361-648X/ac9440.

[33] M. I. Shutikova and V. V. Stegailov. "Vacancy Formation Energy in the Cubic Phase of Magnetite in the Framework of the DFT+U Method". en. In: *J. Exp. Theor. Phys.* 133.2 (Aug. 2021), pp. 206–228. ISSN: 1090-6509. DOI: 10.1134/S1063776121080100.

[34] K. E. Sickafus et al. "Radiation Tolerance of Complex Oxides". In: *Science* 289.5480 (Aug. 2000), pp. 748–751. DOI: 10.1126/science.289.5480.748.

[35] Blas Pedro Uberuaga et al. "Discovering mechanisms relevant for radiation damage evolution". en. In: *Computational Materials Science* 147 (May 2018), pp. 282–292. ISSN: 09270256. DOI: 10.1016/j.commatsci.2018.01.052.

[36] Eric Cockayne and Benjamin P. Burton. "Dipole moment of a Pb-O vacancy pair in PbTiO 3". en. In: *Physical Review B* 69.14 (Apr. 2004), p. 144116. ISSN: 1098-0121, 1550-235X. DOI: 10.1103/PhysRevB.69.144116.

[37] Richard J. Zamora et al. "The effects of cation–anion clustering on defect migration in MgAl2O4". en. In: *Physical Chemistry Chemical Physics* 18.29 (July 2016), pp. 19647–19654. ISSN: 1463-9084. DOI: 10.1039/C6CP03931F.

[38] Samuel T Murphy. "Atomistic simulation of defects and diffusion in oxides". en. PhD Thesis.

[39] Kayla H. Yano et al. "Dose rate dependent cation & anion radiation enhanced diffusion in hematite". en. In: *Journal of Materials Chemistry A* 10.45 (2022), pp. 24167–24177. DOI: 10.1039/D2TA03403D.

[40] Paul Lecoq, Alexander Gektin, and Mikhail Korzhik. *Inorganic Scintillators for Detector Systems*. en. Particle Acceleration and Detection. Cham: Springer International Publishing, 2017. ISBN: 978-3-319-45521-1 978-3-319-45522-8. DOI: 10.1007/978-3-319-45522-8.

[41] A Eempicki. "The physics of inorganic scintillators". en. In: (), p. 16.

[42] Ch B Lushchik and I K Vitol. "Decay of electronic excitations into radiation defects in ionic crystals". en. In: (1977), p. 18.

[43] A. Canning et al. "First-principles study of luminescence in Ce-doped inorganic scintillators". en. In: *Phys. Rev. B* 83.12 (Mar. 2011), p. 125115. ISSN: 1098-0121, 1550-235X. DOI: 10.1103/PhysRevB.83.125115.

[44] R M Van Ginhoven and P A Schultz. "Off-center Tl and Na dopant centers in CsI". In: *J. Phys.: Condens. Matter* 25.49 (Dec. 2013), p. 495504. ISSN: 0953-8984, 1361-648X. DOI: 10.1088/0953-8984/25/49/495504.

[45] K. S. Song and Richard T. Williams. *Self-Trapped Excitons*. Ed. by Manuel Cardona et al. Vol. 105. Springer Series in Solid-State Sciences. Berlin, Heidelberg: Springer Berlin Heidelberg, 1996. ISBN: 978-3-540-60446-4 978-3-642-85236-7. DOI: 10.1007/978-3-642-85236-7.

[46] Peiyun Li et al. "Picosecond Absorption Spectroscopy of Excited States in Ba Br Cl with and without Eu Dopant and Au Codopant". en. In: *Physical Review Applied* 12.1 (July 2019), p. 014035. ISSN: 2331-7019. DOI: 10.1103/PhysRevApplied.12.014035.

[47] J Andriessen, M Marsman, and C W E van Eijk. "*Ab* initio study of the stokes shift of the n s- n p transition of Tl and In in KCl, Jahn-Teller effect in the n s n p configuration". In: *J. Phys.: Condens. Matter* 13.24 (June 2001), pp. 5597–5610. ISSN: 0953-8984, 1361-648X. DOI: 10.1088/0953-8984/13/24/306.

[48] M. P. Fontana and W. J. Van Sciver. "Energy Transfer and Optical Properties of Tl + Centers in NaI(Tl) Crystals". en. In: *Phys. Rev.* 168.3 (Apr. 1968), pp. 960–964. ISSN: 0031-899X. DOI: 10.1103/PhysRev.168.960.

[49] M. H. Du. "Chemical trends of electronic and optical properties of ns ^{2} ions in halides". In: *J. Mater. Chem. C* 2.24 (2014), pp. 4784–4791. ISSN: 2050-7526, 2050-7534. DOI: 10.1039/C4TC00485J.

[50] A. Ranfagni et al. "The optical properties of thallium-like impurities in alkali-halide crystals". In: *Advances in Physics* 32.6 (Jan. 1983), pp. 823–905. ISSN: 0001-8732, 1460-6976. DOI: 10.1080/00018738300101621.

[51] Shunran Li et al. "Self-Trapped Excitons in All-Inorganic Halide Perovskites: Fundamentals, Status, and Potential Applications". In: *J. Phys. Chem. Lett.* 10.8 (Apr. 2019), pp. 1999–2007. ISSN: 1948-7185. DOI: 10.1021/acs.jpclett.8b03604.

[52] Aron Walsh et al. "Stereochemistry of post-transition metal oxides : revision of the classical lone pair model". In: *Chemical Society Reviews* 40.9 (2011), pp. 4455–4463. DOI: 10.1039/C1CS15098G.

[53] Riley E. Brandt et al. "Identifying defect-tolerant semiconductors with high minority-carrier lifetimes: beyond hybrid lead halide perovskites". en. In: *MRS Communications* 5.2 (June 2015), pp. 265–275. ISSN: 2159-6859, 2159-6867. DOI: 10.1557/mrc.2015.26.

[54] P A Christiansen, W C Ermler, and K S Pitzer. "Relativistic Effects in Chemical Systems". In: *Annual Review of Physical Chemistry* 36.1 (1985), pp. 407–432. DOI: 10.1146/annurev.pc.36.100185.002203.

[55] Ulrich Häussermann et al. "TlF and PbO under High Pressure: Unexpected Persistence of the Stereochemically Active Electron Pair". In: *Angewandte Chemie* 113.24 (2001), pp. 4760–4765. ISSN: 1521-3757. DOI: 10.1002/1521-3757(20011217)113:24<4760::AID-ANGE4760>3.0.CO;2-6.

[56] Anja-Verena Mudring. "Thallium Halides – New Aspects of the Stereochemical Activity of Electron Lone Pairs of Heavier Main-Group Elements". In: *European Journal of Inorganic Chemistry* 2007.6 (Feb. 2007), pp. 882–890. ISSN: 1434-1948. DOI: 10.1002/ejic.200600975.

[57] Koushik Biswas and Mao-Hua Du. "Energy transport and scintillation of cerium-doped elpasolite Cs 2 LiYCl 6 : Hybrid density functional calculations". In: *Phys. Rev. B* 86.1 (July 2012), p. 014102. ISSN: 1098-0121, 1550-235X. DOI: 10.1103/PhysRevB.86.014102.

[58] S. G. Zazubovich. "Jahn-Teller Effect and Partially Covalent Bond as Causes of Low Symmetry of Ga+, In+, and Tl+ Centres in CsCl-Type Alkali Halides". In: *phys. stat. sol. (b)* 38.1 (1970), pp. 119–129. ISSN: 03701972, 15213951. DOI: 10.1002/pssb.19700380109.

[59] A. Filipponi et al. "Local lattice relaxation around Tl substitutional impurities in a NaI(Tl) scintillator crystal". In: *Radiation Physics and Chemistry* 177 (Dec. 2020), p. 108992. ISSN: 0969806X. DOI: 10.1016/j.radphyschem.2020.108992.

[60] R. Hawrami et al. "Intrinsic scintillators: TlMgCl and TlCaI". In: *Journal of Crystal Growth* 475 (Oct. 2017), pp. 216–219. ISSN: 00220248. DOI: 10.1016/j.jcrysgro.2017.06.012.

[61] F. Patrick Doty et al. *Elpasolite scintillators.* en. Tech. rep. SAND2012-9951, 1096473. Dec. 2012, SAND2012–9951, 1096473. DOI: 10.2172/1096473.

[62] Felix A. Faber et al. "Machine Learning Energies of 2 Million Elpasolite (ABC_2D_6) Crystals". In: *Phys. Rev. Lett.* 117.13 (2016), p. 135502. DOI: 10.1103/PhysRevLett.117.135502.

[63] H.J. Kim et al. "Luminescence and scintillation properties of the new Ce-doped Tl2LiGdCl6 single crystals". In: *Journal of Luminescence* 164 (Aug. 2015), pp. 86–89. ISSN: 00222313. DOI: 10.1016/j.jlumin.2015.03.026.

[64] R. Hawrami et al. "Tl2LiYCl6: Large Diameter, High Performing Dual Mode Scintillator". In: *Crystal Growth & Design* 17.7 (July 2017), pp. 3960–3964. ISSN: 1528-7483. DOI: 10.1021/acs.cgd.7b00583.

[65] D. R Onken et al. "The crystal structure and temperature dependence of the elpasolite Tl2LiYCl6". In: *Journal of Applied Crystallography* 54.2 (2021), pp. 604–611. ISSN: 1600-5767. DOI: 10.1107/S1600576721002065.

[66] I.N. Flerov et al. "Phase transitions in elpasolites (ordered perovskites)". In: *Materials Science and Engineering: R: Reports* 24.3 (Nov. 1998), pp. 81–151. ISSN: 0927796X. DOI: 10.1016/S0927-796X(98)00015-1.

[67] Xin-Gang Zhao et al. "Polymorphous nature of cubic halide perovskites". In: *Phys. Rev. B* 101.15 (Apr. 2020), p. 155137. ISSN: 2469-9950, 2469-9969. DOI: 10.1103/PhysRevB.101.155137.

[68] P. M. Woodward. "Octahedral Tilting in Perovskites. I. Geometrical Considerations". In: *Acta Cryst B* 53.1 (Feb. 1997), pp. 32–43. ISSN: 0108-7681. DOI: 10.1107/S0108768196010713.

[69] Christopher J. Howard and Harold T. Stokes. "Octahedral tilting in cation-ordered perovskites – a group-theoretical analysis". In: *Acta Crystallogr B Struct Sci* 60.6 (Dec. 2004), pp. 674–684. ISSN: 0108-7681. DOI: 10.1107/S0108768104019901.

[70] Christopher J. Howard, Brendan J. Kennedy, and Patrick M. Woodward. "Ordered double perovskites – a group-theoretical analysis". In: *Acta Crystallogr B Struct Sci* 59.4 (Aug. 2003), pp. 463–471. ISSN: 0108-7681. DOI: 10.1107/S0108768103010073.

[71] Yao Cai et al. "High-throughput Computational Study of Halide Double Perovskite Inorganic Compounds". In: *Chem. Mater.* 31.15 (Aug. 2019), pp. 5392–5401. ISSN: 0897-4756. DOI: 10.1021/acs.chemmater.9b00116.

[72] Richard M. Martin. *Electronic Structure: Basic Theory and Practical Methods*. Cambridge University Press, 2004.

[73] Kieron Burke and Lucas O. Wagner. "DFT in a nutshell". en. In: *International Journal of Quantum Chemistry* 113.2 (2013), pp. 96–101. ISSN: 1097-461X. DOI: 10.1002/qua.24259.

[74] Kieron Burke. "Perspective on density functional theory". In: *The Journal of Chemical Physics* 136.15 (Apr. 2012), p. 150901. ISSN: 0021-9606. DOI: 10.1063/1.4704546.

[75] P. Hohenberg and W. Kohn. "Inhomogeneous Electron Gas". In: *Phys. Rev.* 136 (3B Nov. 1964), B864–B871. DOI: 10.1103/PhysRev.136.B864.

[76] W. Kohn and L. J. Sham. "Self-Consistent Equations Including Exchange and Correlation Effects". In: *Phys. Rev.* 140 (4A Nov. 1965), A1133–A1138. DOI: 10.1103/PhysRev.140.A1133.

[77] John P. Perdew, Kieron Burke, and Matthias Ernzerhof. "Generalized Gradient Approximation Made Simple". In: *Phys. Rev. Lett.* 77.18 (Oct. 1996), pp. 3865–3868. DOI: 10.1103/PhysRevLett.77.3865.

[78] Heather J. Kulik. "Perspective: Treating electron over-delocalization with the DFT+U method". en. In: *The Journal of Chemical Physics* 142.24 (June 2015), p. 240901. ISSN: 0021-9606, 1089-7690. DOI: 10.1063/1.4922693.

[79] S. L. Dudarev et al. "Electron-energy-loss spectra and the structural stability of nickel oxide: An LSDA+U study". In: *Phys. Rev. B* 57.3 (Jan. 1998), pp. 1505–1509. DOI: 10.1103/PhysRevB.57.1505.

[80] Ismaila Dabo et al. "Koopmans' condition for density-functional theory". In: *Phys. Rev. B* 82.11 (Sept. 2010), p. 115121. DOI: 10.1103/PhysRevB.82.115121.

[81] Kieron Burke, John P. Perdew, and Matthias Ernzerhof. "Mixing Exact Exchange with GGA: When to Say When". en. In: *Electronic Density Functional Theory: Recent Progress and New Directions*. Ed. by John F. Dobson, Giovanni Vignale, and Mukunda P. Das. Boston, MA: Springer US, 1998, pp. 57–68. ISBN: 978-1-4899-0316-7. DOI: 10.1007/978-1-4899-0316-7_5.

[82] Carlo Adamo and Vincenzo Barone. "Toward reliable density functional methods without adjustable parameters: The PBE0 model". In: *The Journal of Chemical Physics* 110.13 (Apr. 1999), pp. 6158–6170. ISSN: 0021-9606. DOI: 10.1063/1.478522.

[83] Wei Chen et al. "Nonempirical dielectric-dependent hybrid functional with range separation for semiconductors and insulators". In: *Phys. Rev. Mater.* 2.7 (July 2018), p. 073803. DOI: 10.1103/PhysRevMaterials.2.073803.

[84] Ke Chen et al. "Physics-inspired machine learning of localized intensive properties". In: *Chem Sci* 14.18 (), pp. 4913–4922. ISSN: 2041-6520. DOI: 10.1039/d3sc00841j.

[85] Zhi-Hao Cui et al. "Doubly Screened Hybrid Functional: An Accurate First-Principles Approach for Both Narrow- and Wide-Gap Semiconductors". In: *J. Phys. Chem. Lett.* 9.9 (May 2018), pp. 2338–2345. DOI: 10.1021/acs.jpclett.8b00919.

[86] Peitao Liu et al. "Assessing model-dielectric-dependent hybrid functionals on the antiferromagnetic transition-metal monoxides MnO, FeO, CoO, and NiO". en. In: *J. Phys.: Condens. Matter* 32.1 (Oct. 2019), p. 015502. ISSN: 0953-8984. DOI: 10.1088/1361-648X/ab4150.

[87] A. van de Walle, M. Asta, and G. Ceder. "The alloy theoretic automated toolkit: A user guide". en. In: *Calphad* 26.4 (Dec. 2002), pp. 539–553. ISSN: 0364-5916. DOI: 10.1016/S0364-5916(02)80006-2.

[88] A. van de Walle et al. "Efficient stochastic generation of special quasirandom structures". en. In: *Calphad* 42 (Sept. 2013), pp. 13–18. ISSN: 03645916. DOI: 10.1016/j.calphad.2013.06.006.

[89] P. E. Blöchl. "Projector augmented-wave method". In: *Phys. Rev. B* 50.24 (Dec. 1994), pp. 17953–17979. DOI: 10.1103/PhysRevB.50.17953.

[90] G. Kresse and J. Furthmüller. "Efficient iterative schemes for ab initio total-energy calculations using a plane-wave basis set". In: *Phys. Rev. B* 54.16 (1996), pp. 11169–11186. DOI: 10.1103/PhysRevB.54.11169.

[91] G. Kresse and D. Joubert. "From ultrasoft pseudopotentials to the projector augmented wave method". In: *Phys. Rev. B* 59.3 (Jan. 1999), pp. 1758–1775. DOI: 10.1103/PhysRevB.59.1758.

[92] Peter E. Blöchl, O. Jepsen, and O. K. Andersen. "Improved tetrahedron method for Brillouin-zone integrations". In: *Phys. Rev. B* 49.23 (June 1994), pp. 16223–16233. DOI: 10.1103/PhysRevB.49.16223.

[93] J. F. Janak. "Proof that $\frac{\partial E}{\partial n_i} = \epsilon$ in density-functional theory". In: *Phys. Rev. B* 18.12 (Dec. 1978), pp. 7165–7168. DOI: 10.1103/PhysRevB.18.7165.

[94] Paula Mori-Sánchez, Aron J. Cohen, and Weitao Yang. "Localization and Delocalization Errors in Density Functional Theory and Implications for Band-Gap Prediction". In: *Phys. Rev. Lett.* 100.14 (Apr. 2008), p. 146401. DOI: 10.1103/PhysRevLett.100.146401.

[95] Aron J. Cohen, Paula Mori-Sánchez, and Weitao Yang. "Fractional spins and static correlation error in density functional theory". en. In: *The Journal of Chemical Physics* 129.12 (Sept. 2008), p. 121104. ISSN: 0021-9606, 1089-7690. DOI: 10.1063/1.2987202.

[96] Evert Jan Baerends. "Density functional approximations for orbital energies and total energies of molecules and solids". In: *J. Chem. Phys.* 149.5 (Aug. 2018), p. 054105. ISSN: 0021-9606. DOI: 10.1063/1.5026951.

[97] Nicholas J. Mosey, Peilin Liao, and Emily A. Carter. "Rotationally invariant ab initio evaluation of Coulomb and exchange parameters for DFT+U calculations". In: *J. Chem. Phys.* 129.1 (July 2008), p. 014103. ISSN: 0021-9606. DOI: 10.1063/1.2943142.

[98] F. Zhou et al. "First-principles prediction of redox potentials in transition-metal compounds with \textbackslashmathrmLDA+U". In: *Phys. Rev. B* 70.23 (Dec. 2004), p. 235121. DOI: 10.1103/PhysRevB.70.235121.

[99] Anubhav Jain et al. "Formation enthalpies by mixing GGA and GGA + U calculations". In: *Phys. Rev. B* 84.4 (July 2011), p. 045115. DOI: 10.1103/PhysRevB.84.045115.

[100] B. Meredig et al. "Method for locating low-energy solutions within DFT+U". In: *Phys. Rev. B* 82.19 (Nov. 2010), p. 195128. DOI: 10.1103/PhysRevB.82.195128.

[101] Christoph Freysoldt, Jörg Neugebauer, and Chris G. Van de Walle. "Electrostatic interactions between charged defects in supercells". In: *Phys. Status Solidi B* 248.5 (2011), pp. 1067–1076. ISSN: 1521-3951. DOI: 10.1002/pssb.201046289.

[102] Christoph Freysoldt et al. "First-principles calculations for point defects in solids". In: *Rev. Mod. Phys.* 86.1 (Mar. 2014), pp. 253–305. DOI: 10.1103/RevModPhys.86.253.

[103] Yu Kumagai and Fumiyasu Oba. "Electrostatics-based finite-size corrections for first-principles point defect calculations". In: *Phys. Rev. B* 89.19 (May 2014), p. 195205. DOI: 10.1103/PhysRevB.89.195205.

[104] N. D. M. Hine et al. "Supercell size scaling of density functional theory formation energies of charged defects". In: *Phys. Rev. B* 79.2 (Jan. 2009), p. 024112. DOI: 10.1103/PhysRevB.79.024112.

[105] Christoph Freysoldt, Jörg Neugebauer, and Chris G. Van de Walle. "Fully *Ab* Initio Finite-Size Corrections for Charged-Defect Supercell Calculations". In: *Phys. Rev. Lett.* 102.1 (Jan. 2009), p. 016402. DOI: 10.1103/PhysRevLett.102.016402.

[106] S. B. Zhang and John E. Northrup. "Chemical potential dependence of defect formation energies in GaAs: Application to Ga self-diffusion". In: *Phys. Rev. Lett.* 67.17 (Oct. 1991), pp. 2339–2342. DOI: 10.1103/PhysRevLett.67.2339.

[107] Christoph Freysoldt et al. "Electron and chemical reservoir corrections for point-defect formation energies". In: *Physical Review B* 93.16 (2016), p. 165206.

[108] Xavier Gonze and Changyol Lee. "Dynamical matrices, Born effective charges, dielectric permittivity tensors, and interatomic force constants from density-functional perturbation theory". In: *Phys. Rev. B* 55.16 (Apr. 1997), pp. 10355–10368. DOI: 10.1103/PhysRevB.55.10355.

[109] X. Gonze et al. "Interatomic force constants from first principles: The case of α-quartz". In: *Phys. Rev. B* 50.17 (Nov. 1994), pp. 13035–13038. DOI: 10.1103/PhysRevB.50.13035.

[110] Hongsheng Liu and Cristiana Di Valentin. "Band Gap in Magnetite above Verwey Temperature Induced by Symmetry Breaking". en. In: *J. Phys. Chem. C* 121.46 (Nov. 2017), pp. 25736–25742. ISSN: 1932-7447, 1932-7455. DOI: 10.1021/acs.jpcc.7b09387.

[111] Amitava Banerjee et al. "Thermokinetics of point defects in -Fe2O3". en. In: *Electron. Struct.* 5.2 (May 2023), p. 024007. ISSN: 2516-1075. DOI: 10.1088/2516-1075/acd158.

[112] G. Kresse and J. Furthmüller. "Efficiency of ab-initio total energy calculations for metals and semiconductors using a plane-wave basis set". In: *Computational Materials Science* 6.1 (July 1996), pp. 15–50. ISSN: 0927-0256. DOI: 10.1016/0927-0256(96)00008-0.

[113] Thomas D. Kühne et al. "CP2K: An electronic structure and molecular dynamics software package - Quickstep: Efficient and accurate electronic structure calculations". In: *The Journal of Chemical Physics* 152.19 (May 2020), p. 194103. ISSN: 0021-9606. DOI: 10.1063/5.0007045.

[114] Jürg Hutter et al. "cp2k: atomistic simulations of condensed matter systems". In: *WIREs Computational Molecular Science* 4.1 (2014), pp. 15–25. ISSN: 1759-0884. DOI: 10.1002/wcms.1159.

[115] Manuel Guidon, Jürg Hutter, and Joost VandeVondele. "Robust Periodic Hartree-Fock Exchange for Large-Scale Simulations Using Gaussian Basis Sets". In: *J. Chem. Theory Comput.* 5.11 (Nov. 2009), pp. 3010–3021. ISSN: 1549-9618. DOI: 10.1021/ct900494g.

[116] Manuel Guidon et al. "Ab initio molecular dynamics using hybrid density functionals". In: *The Journal of Chemical Physics* 128.21 (June 2008), p. 214104. ISSN: 0021-9606. DOI: 10.1063/1.2931945.

[117] Richard Dronskowski and Peter E. Bloechl. "Crystal orbital Hamilton populations (COHP): energy-resolved visualization of chemical bonding in solids based on density-functional calculations". In: *J. Phys. Chem.* 97.33 (Aug. 1993), pp. 8617–8624. ISSN: 0022-3654. DOI: 10.1021/j100135a014.

[118] Volker L. Deringer, Andrei L. Tchougréeff, and Richard Dronskowski. "Crystal Orbital Hamilton Population (COHP) Analysis As Projected from Plane-Wave Basis Sets". In: *J. Phys. Chem. A* 115.21 (June 2011), pp. 5461–5466. ISSN: 1089-5639. DOI: 10.1021/jp202489s.

[119] Stefan Maintz et al. "LOBSTER: A tool to extract chemical bonding from plane-wave based DFT". en. In: *Journal of Computational Chemistry* 37.11 (2016), pp. 1030–1035. ISSN: 1096-987X. DOI: 10.1002/jcc.24300.

[120] Ryky Nelson et al. "LOBSTER: Local orbital projections, atomic charges, and chemical bonding analysis from projector-augmented-wave-based density-functional theory". en. In: *Journal of Computational Chemistry* 41.21 (2020), pp. 1931–1940. ISSN: 1096-987X. DOI: 10.1002/jcc.26353.

[121] Yoyo Hinuma et al. "Band structure diagram paths based on crystallography". In: *Computational Materials Science* 128 (Feb. 2017), pp. 140–184. ISSN: 0927-0256. DOI: 10.1016/j.commatsci.2016.10.015.

[122] Alex M. Ganose, Adam J. Jackson, and David O. Scanlon. "sumo: Command-line tools for plotting and analysis of periodic *ab initio* calculations". In: *Journal of Open Source Software* 3.28 (Aug. 2018), p. 717. ISSN: 2475-9066. DOI: 10.21105/joss.00717.

[123] Stefano Baroni and Raffaele Resta. "Ab initio calculation of the macroscopic dielectric constant in silicon". In: *Phys. Rev. B* 33.10 (May 1986), pp. 7017–7021. DOI: 10.1103/PhysRevB.33.7017.

[124] M. Gajdoš et al. "Linear optical properties in the projector-augmented wave methodology". In: *Phys. Rev. B* 73.4 (Jan. 2006), p. 045112. DOI: 10.1103/PhysRevB.73.045112.

[125] Atsushi Togo and Isao Tanaka. "First principles phonon calculations in materials science". In: *Scripta Materialia* 108 (Nov. 2015), pp. 1–5. ISSN: 1359-6462. DOI: 10.1016/j.scriptamat.2015.07.021.

[126] Joost VandeVondele and Jürg Hutter. "Gaussian basis sets for accurate calculations on molecular systems in gas and condensed phases". In: *The Journal of Chemical Physics* 127.11 (Sept. 2007), p. 114105. ISSN: 0021-9606. DOI: 10.1063/1.2770708.

[127] Joost VandeVondele et al. "Quickstep: Fast and accurate density functional calculations using a mixed Gaussian and plane waves approach". In: *Computer Physics Communications* 167.2 (Apr. 2005), pp. 103–128. ISSN: 0010-4655. DOI: 10.1016/j.cpc.2004.12.014.

[128] Manuel Guidon, Jürg Hutter, and Joost VandeVondele. "Auxiliary Density Matrix Methods for Hartree-Fock Exchange Calculations". In: *J. Chem. Theory Comput.* 6.8 (Aug. 2010), pp. 2348–2364. ISSN: 1549-9618. DOI: 10.1021/ct1002225.

[129] Joost VandeVondele and Jürg Hutter. "An efficient orbital transformation method for electronic structure calculations". In: *The Journal of Chemical Physics* 118.10 (Feb. 2003), pp. 4365–4369. ISSN: 0021-9606. DOI: 10.1063/1.1543154.

[130] M. Krack. "Pseudopotentials for H to Kr optimized for gradient-corrected exchange-correlation functionals". In: *Theor Chem Acc* 114.1 (Sept. 2005), pp. 145–152. ISSN: 1432-2234. DOI: 10.1007/s00214-005-0655-y.

[131] S. Goedecker, M. Teter, and J. Hutter. "Separable dual-space Gaussian pseudopotentials". In: *Phys. Rev. B* 54.3 (July 1996), pp. 1703–1710. DOI: 10.1103/PhysRevB.54.1703.

[132] Richard M. Martin. *Electronic Structure: Basic Theory and Practical Methods*. Cambridge University Press, 2004.

[133] Jörg Behler et al. "Nonadiabatic potential-energy surfaces by constrained density-functional theory". en. In: *Physical Review B* 75.11 (Mar. 2007), p. 115409. ISSN: 1098-0121, 1550-235X. DOI: 10.1103/PhysRevB.75.115409.

[134] R. Monnier et al. "Change-in-self-consistent-field theory of the work function". In: *Physical Review B* 18.2 (July 1978), pp. 656–666. DOI: 10.1103/PhysRevB.18.656.

[135] Ulf von Barth. "Local-density theory of multiplet structure". In: *Physical Review A* 20.4 (Oct. 1979), pp. 1693–1703. DOI: 10.1103/PhysRevA.20.1693.

[136] A. Hellman, B. Razaznejad, and B. I. Lundqvist. "Potential-energy surfaces for excited states in extended systems". In: *The Journal of Chemical Physics* 120.10 (Mar. 2004), pp. 4593–4602. ISSN: 0021-9606. DOI: 10.1063/1.1645787.

[137] Dan Han et al. "Unraveling luminescence mechanisms in zero-dimensional halide perovskites". en. In: *Journal of Materials Chemistry C* 6.24 (June 2018). Publisher: The Royal Society of Chemistry, pp. 6398–6405. ISSN: 2050-7534. DOI: 10.1039/C8TC01291A.

[138] Hongliang Shi et al. "Impact of metal n s 2 lone pair on luminescence quantum efficiency in low-dimensional halide perovskites". en. In: *Physical Review Materials* 3.3 (Mar. 2019), p. 034604. ISSN: 2475-9953. DOI: 10.1103/PhysRevMaterials.3.034604.

[139] Guanhong Wu et al. "A One-Dimensional Organic Lead Chloride Hybrid with Excitation Dependent Broadband Emissions". In: *ACS Energy Letters* 3.6 (June 2018). Publisher: American Chemical Society, pp. 1443–1449. DOI: 10.1021/acsenergylett.8b00661.

[140] Vladan Stevanović, Mayeul d'Avezac, and Alex Zunger. "Universal Electrostatic Origin of Cation Ordering in A2BO4 Spinel Oxides". In: *J. Am. Chem. Soc.* 133.30 (Aug. 2011), pp. 11649–11654. ISSN: 0002-7863. DOI: 10.1021/ja2034602.

[141] Albert P. Bartók, Risi Kondor, and Gábor Csányi. "On representing chemical environments". In: *Phys. Rev. B* 87.18 (May 2013), p. 184115. DOI: 10.1103/PhysRevB.87.184115.

[142] C. C. Wu and T. O. Mason. "Thermopower Measurement of Cation Distribution in Magnetite". en. In: *Journal of the American Ceramic Society* 64.9 (1981), pp. 520–522. ISSN: 1551-2916. DOI: 10.1111/j.1151-2916.1981.tb10317.x.

[143] J. P. Shepherd et al. "Heat capacity and entropy of nonstoichiometric magnetite $Fe_{3(1-\delta)}O_4$: The thermodynamic nature of the Verwey transition". In: *Phys. Rev. B* 43.10 (Apr. 1991), pp. 8461–8471. DOI: 10.1103/PhysRevB.43.8461.

[144] Masanobu Nakayama et al. "A concerted migration mechanism of mixed oxide ion and electron conduction in reduced ceria studied by first-principles density functional theory". en. In: *Phys. Chem. Chem. Phys.* 14.17 (2012), p. 6079. ISSN: 1463-9076, 1463-9084. DOI: 10.1039/c2cp00020b.

[145] Dawei Zhang et al. "Oxygen-Vacancy Dynamics and Entanglement with Polaron Hopping at the Reduced \textbackslashmathrmCeO_2(111) Surface". In: *Phys. Rev. Lett.* 122.9 (Mar. 2019), p. 096101. DOI: 10.1103/PhysRevLett.122.096101.

[146] Ryan M. Trottier et al. "Predicting Spinel Disorder and Its Effect on Oxygen Transport Kinetics in Hercynite". en. In: *ACS Appl. Mater. Interfaces* 12.21 (May 2020), pp. 23831–23843. ISSN: 1944-8244, 1944-8252. DOI: 10.1021/acsami.0c02819.

[147] Blas P. Uberuaga and Ghanshyam Pilania. "Inversion, chemical complexity, and interstitial transport in spinels". en. In: *Journal of the American Ceramic Society* 104.5 (2021), pp. 2313–2324. ISSN: 1551-2916. DOI: 10.1111/jace.17598.

[148] I. V. Belova and G. E. Murch. "Tracer diffusion via bound vacancy pairs in mixed ionic crystals". In: *Philosophical Magazine A* 79.11 (Nov. 1999), pp. 2681–2690. ISSN: 0141-8610. DOI: 10.1080/01418619908212017.

[149] I. V. Belova and G. E. Murch. "Diffusion kinetics for migration by bound vacancy pairs in ionic crystals". In: *Philosophical Magazine A* 79.7 (July 1999), pp. 1509–1515. ISSN: 0141-8610. DOI: 10.1080/01418619908210376.

[150] Sanchita Dey et al. "Radiation Tolerance of Nanocrystalline Ceramics: Insights from Yttria Stabilized Zirconia". In: *Scientific Reports* 5 (Jan. 2015), p. 7746. ISSN: 2045-2322. DOI: 10.1038/srep07746.

[151] Ho Lun Chan et al. "Multi–length scale characterization of point defects in thermally oxidized, proton irradiated iron oxides". In: *Materialia* 28 (May 2023), p. 101762. ISSN: 2589-1529. DOI: 10.1016/j.mtla.2023.101762.

[152] Peilin Liao, Maytal Caspary Toroker, and Emily A. Carter. "Electron Transport in Pure and Doped Hematite". In: *Nano Letters* 11.4 (Apr. 2011), pp. 1775–1781. ISSN: 1530-6984. DOI: 10.1021/nl200356n.

[153] Amitava Banerjee et al. "Interplay between defect transport and cation spin frustration in corundum-structured oxides". In: *Physical Review Materials* 5.3 (Mar. 2021), p. 034410. DOI: 10.1103/PhysRevMaterials.5.034410.

[154] J. Engel and H. L. Tuller. "The electrical conductivity of thin film donor doped hematite: from insulator to semiconductor by defect modulation". en. In: *Physical Chemistry Chemical Physics* 16.23 (May 2014), pp. 11374–11380. ISSN: 1463-9084. DOI: 10.1039/C4CP01144A.

[155] Christian S. Ahart, Kevin M. Rosso, and Jochen Blumberger. "Electron and Hole Mobilities in Bulk Hematite from Spin-Constrained Density Functional Theory". In: *Journal of the American Chemical Society* 144.10 (Mar. 2022), pp. 4623–4632. ISSN: 0002-7863. DOI: 10.1021/jacs.1c13507.

[156] Christopher Matthews et al. "Cluster dynamics simulation of uranium self-diffusion during irradiation in UO2". en. In: *Journal of Nuclear Materials* 527 (Dec. 2019), p. 151787. ISSN: 00223115. DOI: 10.1016/j.jnucmat.2019.151787.

[157] *Radii for All Species http://abulafia.mt.ic.ac.uk/shannon/radius.php.*

[158] V. M. Goldschmidt. "Die Gesetze der Krystallochemie". In: *Naturwissenschaften* 14.21 (May 1926), pp. 477–485. ISSN: 1432-1904. DOI: 10.1007/BF01507527.

[159] Christopher J. Bartel et al. "New tolerance factor to predict the stability of perovskite oxides and halides". In: *Science Advances* 5.2 (Feb. 2019), eaav0693. DOI: 10.1126/sciadv.aav0693.

[160] Xin-Gang Zhao et al. "The effects of intrinsic local distortions vs. dynamic thermal motions on the stability and band gaps of cubic oxide and halide perovskites". In: *Materials Today* 49 (Oct. 2021), pp. 107–122. ISSN: 13697021. DOI: 10.1016/j.mattod.2021.05.021.

[161] Douglas H. Fabini, Ram Seshadri, and Mercouri G. Kanatzidis. "The underappreciated lone pair in halide perovskites underpins their unusual properties". In: *MRS Bulletin* 45.6 (June 2020), pp. 467–477. ISSN: 0883-7694, 1938-1425. DOI: 10.1557/mrs.2020.142.

[162] Lingyuan Gao et al. "Metal cation s lone-pairs increase octahedral tilting instabilities in halide perovskites". In: *Materials Advances* 2.14 (2021), pp. 4610–4616. DOI: 10.1039/D1MA00288K.

[163] Mao-Hua Du and David J. Singh. "Enhanced Born charge and proximity to ferroelectricity in thallium halides". In: *Phys. Rev. B* 81.14 (Apr. 2010), p. 144114. ISSN: 1098-0121, 1550-235X. DOI: 10.1103/PhysRevB.81.144114.

[164] *http://vergil.chemistry.gatech.edu/notes/hf-intro/hf-intro.html.*

[165] W. Zhong, David Vanderbilt, and K. M. Rabe. "First-principles theory of ferroelectric phase transitions for perovskites: The case of BaTiO 3". In: *Phys. Rev. B* 52.9 (Sept. 1995), pp. 6301–6312. ISSN: 0163-1829, 1095-3795. DOI: 10.1103/PhysRevB.52.6301.

[166] Jonathan Lahnsteiner and Menno Bokdam. "Anharmonic lattice dynamics in large thermodynamic ensembles with machine-learning force fields: Cs Pb Br 3 , a phonon liquid with Cs rattlers". In: *Phys. Rev. B* 105.2 (Jan. 2022), p. 024302. ISSN: 2469-9950, 2469-9969. DOI: 10.1103/PhysRevB.105.024302.

[167] Christopher E. Patrick, Karsten W. Jacobsen, and Kristian S. Thygesen. "Anharmonic stabilization and band gap renormalization in the perovskite CsSnI". In: *Phys. Rev. B* 92.20 (Nov. 2015), p. 201205. DOI: 10.1103/PhysRevB.92.201205.

[168] Moinak Dutta et al. "Ultralow Thermal Conductivity in Chain-like TlSe Due to Inherent Tl Rattling". In: *J. Am. Chem. Soc.* 141.51 (Dec. 2019), pp. 20293–20299. ISSN: 0002-7863, 1520-5126. DOI: 10.1021/jacs.9b10551.

[169] Koushik Pal, Yi Xia, and Chris Wolverton. "Microscopic mechanism of unusual lattice thermal transport in TlInTe2". In: *npj Comput Mater* 7.1 (Dec. 2021), p. 5. ISSN: 2057-3960. DOI: 10.1038/s41524-020-00474-5.

[170] A. M. Glazer. "The classification of tilted octahedra in perovskites". In: *Acta Crystallographica Section B* 28.11 (1972), pp. 3384–3392. DOI: 10.1107/S0567740872007976.

[171] A.K Azad et al. "Synthesis, structural and magnetic characterisation of the double perovskite A2MnMoO6 (A=Ba, Sr)". In: *Journal of Alloys and Compounds* 364.1 (2004), pp. 77–82. ISSN: 0925-8388. DOI: https://doi.org/10.1016/S0925-8388(03)00611-X.

[172] Atsushi Togo and Isao Tanaka. "Spglib: a software library for crystal symmetry search". In: (2018). DOI: 10.48550/arXiv.1808.01590.

[173] Haoyan Huo and Matthias Rupp. "Unified representation of molecules and crystals for machine learning". en. In: *Machine Learning: Science and Technology* 3.4 (Nov. 2022), p. 045017. ISSN: 2632-2153. DOI: 10.1088/2632-2153/aca005.

[174] Lauri Himanen et al. "DScribe: Library of descriptors for machine learning in materials science". In: *Computer Physics Communications* 247 (2020), p. 106949. ISSN: 0010-4655. DOI: 10.1016/j.cpc.2019.106949.

[175] Jarno Laakso et al. *Updates to the DScribe Library: New Descriptors and Derivatives*. 2023.

[176] Sandip De et al. "Comparing molecules and solids across structural and alchemical space". In: *Phys. Chem. Chem. Phys.* 18.20 (2016), pp. 13754–13769. DOI: 10.1039/C6CP00415F.

[177] Vivaldo Leiria Campo and Matteo Cococcioni. "Extended DFT + U + V method with on-site and inter-site electronic interactions". en. In: *J. Phys.: Condens. Matter* 22.5 (Jan. 2010), p. 055602. ISSN: 0953-8984. DOI: 10.1088/0953-8984/22/5/055602.

[178] Nelson Naveas et al. "First-Principles Calculations of Magnetite (Fe3O4) above the Verwey Temperature by Using Self-Consistent DFT + U + V". In: *J. Chem. Theory Comput.* 19.23 (Dec. 2023), pp. 8610–8623. ISSN: 1549-9618. DOI: 10.1021/acs.jctc.3c00860.

[179] Matteo Cococcioni and Stefano de Gironcoli. "Linear response approach to the calculation of the effective interaction parameters in the LDA+U method". In: *Phys. Rev. B* 71.3 (Jan. 2005), p. 035105. DOI: 10.1103/PhysRevB.71.035105.

[180] Qing Zhao, Efthymios I. Ioannidis, and Heather J. Kulik. "Global and local curvature in density functional theory". In: *The Journal of Chemical Physics* 145.5 (Aug. 2016), p. 054109. ISSN: 0021-9606. DOI: 10.1063/1.4959882.

[181] Edward B. Linscott et al. "Role of spin in the calculation of Hubbard U and Hund's J parameters from first principles". In: *Phys. Rev. B* 98.23 (Dec. 2018), p. 235157. DOI: 10.1103/PhysRevB.98.235157.

[182] S. Sharma et al. "Source-Free Exchange-Correlation Magnetic Fields in Density Functional Theory". In: *J. Chem. Theory Comput.* 14.3 (Mar. 2018), pp. 1247–1253. ISSN: 1549-9618. DOI: 10.1021/acs.jctc.7b01049.

[183] Ryo Nagai and Ryosuke Akashi. "Development of Exchange-Correlation Functionals Assisted by Machine Learning". en. In: *Machine Learning in Molecular Sciences*. Ed. by Chen Qu and Hanchao Liu. Challenges and Advances in Computational Chemistry and Physics. Cham: Springer International Publishing, 2023, pp. 91–112. ISBN: 978-3-031-37196-7. DOI: 10.1007/978-3-031-37196-7_4.

[184] Maituo Yu et al. "Machine learning the Hubbard U parameter in DFT+U using Bayesian optimization". en. In: *npj Comput Mater* 6.1 (Nov. 2020), pp. 1–6. ISSN: 2057-3960. DOI: 10.1038/s41524-020-00446-9.

[185] Federico M. Paruzzo et al. "Chemical shifts in molecular solids by machine learning". In: *Nat Commun* 9 (Oct. 2018), p. 4501. ISSN: 2041-1723. DOI: 10.1038/s41467-018-06972-x.

[186] Vladan Stevanović et al. "Correcting density functional theory for accurate predictions of compound enthalpies of formation: Fitted elemental-phase reference energies". en. In: *Phys. Rev. B* 85.11 (Mar. 2012), p. 115104. ISSN: 1098-0121, 1550-235X. DOI: 10.1103/PhysRevB.85.115104.

[187] Péter Ágoston and Karsten Albe. "Formation entropies of intrinsic point defects in cubic In 2 O 3 from first-principles density functional theory calculations". en. In: *Physical Chemistry Chemical Physics* 11.17 (2009), pp. 3226–3232. DOI: 10.1039/B900280D.

[188] Philipp Beck et al. "Influence of polarizability on metal oxide properties studied by molecular dynamics simulations". en. In: *J. Phys.: Condens. Matter* 24.48 (Nov. 2012), p. 485401. ISSN: 0953-8984. DOI: 10.1088/0953-8984/24/48/485401.

[189] P. W. Fowler and P. A. Madden. "In-crystal polarizabilities of alkali and halide ions". In: *Physical Review B* 29.2 (Jan. 1984), pp. 1035–1042. DOI: 10.1103/PhysRevB.29.1035.

[190] Jörg Behler. "Four Generations of High-Dimensional Neural Network Potentials". In: *Chemical Reviews* 121.16 (Aug. 2021), pp. 10037–10072. ISSN: 0009-2665. DOI: 10.1021/acs.chemrev.0c00868.

[191] Tsz Wai Ko et al. "Accurate Fourth-Generation Machine Learning Potentials by Electrostatic Embedding". In: *Journal of Chemical Theory and Computation* 19.12 (June 2023), pp. 3567–3579. ISSN: 1549-9618. DOI: 10.1021/acs.jctc.2c01146.

[192] Tsz Wai Ko et al. "A fourth-generation high-dimensional neural network potential with accurate electrostatics including non-local charge transfer". en. In: *Nature Communications* 12.1 (Jan. 2021), p. 398. ISSN: 2041-1723. DOI: 10.1038/s41467-020-20427-2.

[193] Emir Kocer, Tsz Wai Ko, and Jörg Behler. "Neural Network Potentials: A Concise Overview of Methods". In: *Annual Review of Physical Chemistry* 73.1 (2022), pp. 163–186. DOI: 10.1146/annurev-physchem-082720-034254.

[194] Yun Kyung Shin et al. "Development of a ReaxFF Reactive Force Field for Fe/Cr/O/S and Application to Oxidation of Butane over a Pyrite-Covered Cr2O3 Catalyst". In: *ACS Catal.* 5.12 (Dec. 2015), pp. 7226–7236. DOI: 10.1021/acscatal.5b01766.

[195] Lars Hedin. "New Method for Calculating the One-Particle Green's Function with Application to the Electron-Gas Problem". In: *Phys. Rev.* 139.3A (Aug. 1965), A796–A823. DOI: 10.1103/PhysRev.139.A796.

[196] Michael Rohlfing and Steven G. Louie. "Electron-hole excitations and optical spectra from first principles". In: *Phys. Rev. B* 62.8 (Aug. 2000), pp. 4927–4944. DOI: 10.1103/PhysRevB.62.4927.

[197] Jack Deslippe et al. "BerkeleyGW: A massively parallel computer package for the calculation of the quasiparticle and optical properties of materials and nanostructures". In: *Computer Physics Communications* 183.6 (June 2012), pp. 1269–1289. ISSN: 0010-4655. DOI: 10.1016/j.cpc.2011.12.006.

[198] Mauro Del Ben et al. "Large-scale GW calculations on pre-exascale HPC systems". In: *Computer Physics Communications* 235 (Feb. 2019), pp. 187–195. ISSN: 0010-4655. DOI: 10.1016/j.cpc.2018.09.003.

[199] Laura M. Herz. "How Lattice Dynamics Moderate the Electronic Properties of Metal-Halide Perovskites". In: *J. Phys. Chem. Lett.* 9.23 (Dec. 2018), pp. 6853–6863. DOI: 10.1021/acs.jpclett.8b02811.

[200] Fei Zhou et al. "Lattice Anharmonicity and Thermal Conductivity from Compressive Sensing of First-Principles Calculations". In: *Phys. Rev. Lett.* 113.18 (Oct. 2014), p. 185501. DOI: 10.1103/PhysRevLett.113.185501.

[201] Gabriel Antonius and Steven G. Louie. "Theory of exciton-phonon coupling". In: *Phys. Rev. B* 105.8 (Feb. 2022), p. 085111. DOI: 10.1103/PhysRevB.105.085111.

[202] Marina R. Filip, Jonah B. Haber, and Jeffrey B. Neaton. "Phonon Screening of Excitons in Semiconductors: Halide Perovskites and Beyond". In: *Phys. Rev. Lett.* 127.6 (Aug. 2021), p. 067401. DOI: 10.1103/PhysRevLett.127.067401.

[203] Marina R. Filip et al. "Screening of Excitons by Organic Cations in Quasi-Two-Dimensional Organic–Inorganic Lead-Halide Perovskites". In: *Nano Lett.* 22.12 (June 2022), pp. 4870–4878. ISSN: 1530-6984. DOI: 10.1021/acs.nanolett.2c01306.